RCR Russian Chemical Reviews

https://doi.org/10.59761/RCR5263

Accepted Manuscript

Recent progress on structural design, composite electrocatalysis and interfacial regulation for high-performance sulfur cathodes in lithium-sulfur batteries

Submitted: 25 August 2026

Published: 18 November 2026

Cite this article as: Y.Liu, Y.Yang, R.Shao, Z.Chen, Z.Jin, L.Sun. Recent progress on structural design, composite electrocatalysis and interfacial regulation for high-performance sulfur cathodes in lithium-sulfur batteries. *Russ. Chem. Rev.*, RCR5263; https://doi.org/10.59761/RCR5263

Yang Liu, Yaping Yang, Rong Shao, Zhidong Chen, Zhong Jin & Lin Sun

This is a PDF file of a peer-reviewed manuscript that has been accepted for publication in Russian Chemical Reviews. The text and figures will undergo editing, formatting and proof reading before the article is published in its final form. The file will be replaced with the Version of Record.

Accepted manuscript
This manuscript will be edited, formatted, and proof read. The file will be replaced with Version of Record.

Recent progress on structural design, composite electrocatalysis and interfacial regulation for high-performance sulfur cathodes in lithium-sulfur batteries

Yang Liu,[a,b] Yaping Yang,[b] Rong Shao,[b] Zhidong Chen,[a,*] Zhong Jin,[c,*] Lin Sun,[b,*]

[a] *School of Materials Science & Engineering, Changzhou University, Changzhou, Jiangsu 213164, China*

[b] *School of Chemistry and Chemical Engineering, Yancheng Institute of Technology, Yancheng, 224051, China*

[c] *School of Chemistry and Chemical Engineering, Nanjing University, Nanjing 210023, China*

*Corresponding authors.

E-mail: sunlin@nju.edu.cn (Lin Sun); chenzd@cczu.edu.cn (Zhidong Chen); zhongjin@nju.edu.cn (Zhong Jin)

Accepted manuscript

This manuscript will be edited, formatted, and proofread. The file will be replaced with Version of Record.

Abstract:

Lithium-sulfur batteries feature ultrahigh energy density and low-cost sulfur cathodes, yet poor conductivity, severe volume expansion and polysulfide shuttle hinder their commercialization. This review categorizes mainstream sulfur cathode optimizations into three independent technical routes: structural design, composite electrocatalysis and interfacial regulation. We systematically elaborate the working mechanisms, merits and inherent drawbacks of each strategy, and critically analyze unavoidable performance trade-offs when combining multiple modifications. High-porous carbon hosts boost catalysis but sacrifice volumetric energy density; dense interfacial layers suppress shuttling yet raise ion transport resistance; metal catalysts accelerate redox kinetics but suffer ion leaching and active site passivation. Sulfurized polyacrylonitrile cathodes with solid-solid conversion are discussed separately, as they fundamentally eliminate soluble polysulfides and match ester electrolytes well. Industrial metrics including areal sulfur loading, electrolyte-to-sulfur ratio (E/S ratio) and negative-to-positive ratio (N/P ratio) are adopted to evaluate reported electrode practicability. Unlike reviews advocating idealized integrated synergies, this work clarifies the lack of quantitative evidence for cross-strategy synergistic gains. We finally propose differentiated optimization schemes tailored to distinct performance targets and highlight key research gaps oriented toward practical pouch cells, offering critical references for developing viable high-energy Li-S cathodes.

Keywords: Li-S battery; Cathode material; Structural design; Composite catalysis; Interface regulation

Accepted manuscript
This manuscript will be edited, formatted and proofread. The file will be replaced with the Version of Record.

Contents

1 Introduction

2 Fundamentals and Core Bottlenecks of Sulfur Cathodes for Li-S Batteries

3 Structural Confinement Design for Physical Regulation

4 Composite Electrocatalysis for Accelerated Redox Kinetics

5 Interfacial Engineering to Suppress Shuttle Effect

6 Covalent Sulfurized Polymer Cathodes with Solid－Solid Conversion (SPAN System)

7 Conclusions and Industrialization-Oriented Future Outlook

8 References

Accepted manuscript
This manuscript will be edited, formatted, and proof read. The file will be replaced with Version of Record.

1 Introduction

The escalating depletion of global fossil fuel reserves, coupled with the intensifying challenges of environmental pollution, has fundamentally challenged conventional energy systems. Accordingly, the development of green and low-carbon energy storage technologies has emerged as a pivotal strategy to address the prevailing energy crisis. Meanwhile, the ever-increasing demands for high-energy-density, safe, reliable and cost-effective batteries in grid-scale energy storage, consumer electronics and new energy vehicles is vigorously driving the research, development, and industrialization of next-generation battery chemistries, including lithium-ion batteries (LIBs) and Lithium-sulfur (Li-S) batteries.[1-3]

Although conventional LIBs are widely applied in consumer electronics and electric vehicles,[4] their energy density is increasingly limited by the theoretical capacity of cathode materials, rendering them unable to meet the stringent performance requirements of future energy storage systems. In contrast, Li-S battery with a sulfur cathode offer a compelling alternative. Sulfur features an ultrahigh theoretical specific capacity (1675 mAh g^{-1})，while the high theoretical energy density of 2600 Wh kg^{-1} belongs to the full Li-S electrochemical system rather than elemental sulfur alone.[5] Furthermore, sulfur is abundant, environmentally benign, non-toxic, and low-cost, which positions Li-S battery as a leading candidate for next-generation high-specific-energy storage systems.

However, the practical application of Li-S battery is confronted with several critical scientific and technical challenges. Firstly, the intrinsically poor electronic conductivity of elemental sulfur and its discharge products (Li_2S/Li_2S_2) severely impedes the electrochemical reaction kinetics, leading to low sulfur utilization.[6] Secondly, soluble lithium polysulfides (LiPSs , Li_2S_n, $4 \leqslant n \leqslant 8$) generated during cycling readily migrate between the cathode and anode through the electrolyte, inducing the well-known “polysulfide shuttle effect”. This phenomenon results in continuous loss of active materials and exacerbated

Accepted manuscript
This manuscript will be edited, formatted, and proofread. The file will be replaced with Version of Record.

parasitic reactions at electrode interfaces. Concurrently, the sulfur electrode undergoes substantial volume expansion (up to 80%) during the electrochemical conversion process,[7] which can trigger structural collapse of the electrode and detachment of active materials from the current collector. Additionally, the lithium metal anode is prone to non-uniform deposition during lithium plating/stripping, leading to dendrite formation. These dendrites not only disrupt ion transport pathways but also cause damage and failure of the solid electrolyte interphase (SEI) layer.[8]

Over the past decade, Li-S batteries have become a research focus in the electrochemistry and energy materials communities. According to Web of Science statistics, the number of research publications in this field has increased sustainably and rapidly, with studies on cathode materials accounting for over 50%, which underscores the research intensity and application potential of this technology (**Figure 1**). Researchers worldwide have carried out extensive systematic work to address the aforementioned bottlenecks, and progressively developed multi-dimensional and multi-level optimization strategies. These strategies include: (i) Cathode structure design, constructing composite electrodes by integrating sulfur with various hosts (e.g., carbon-based materials,[9, 10] metal compounds,[11, 12] and polymers,[13]) to achieve high conductivity, high sulfur loading, and enhanced structural stability; (ii) Electrolyte optimization, developing high-concentration electrolytes,[14, 15] ionic liquid-based electrolytes,[16] and solid-state electrolytes [17, 18] to suppress polysulfide dissolution and shuttling; (iii) Functionalized separator modification,[19, 20] constructing physical and chemical barrier layers for efficient polysulfide interception; (iv) Lithium anode protection, adopting surface coating,[21, 22] composite structure design[23-25] and other methods to improve the uniformity of lithium deposition and interfacial stability. The combined adoption of these strategies has significantly improved the cycling stability, rate capability, and safety of Li-S batteries.

Accepted manuscript
This manuscript will be edited, formatted and proofread. There will be replaced with Version of Record.

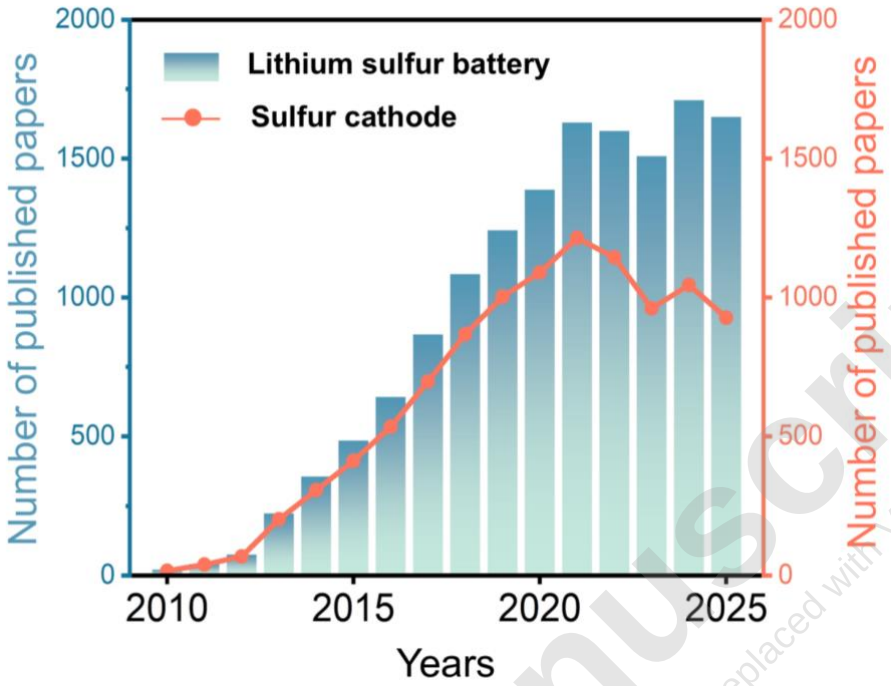


Figure 1. Publication trend of relevant research papers with the keywords of "Lithium-sulfur battery" and "sulfur cathode" since 2010 based on Web of Science Database .

Numerous review articles have summarized sulfur cathode modification from single perspectives such as carbon hosts, electrocatalysts or separator modification. However, most existing works either elaborate a single technical route in detail or simply list various material systems without comparative analysis of the inherent conflicts among different optimization approaches. Furthermore, few reviews integrate industrial quantitative indicators (E/S ratio, N/P ratio, volumetric energy density) to screen and evaluate reported electrode performance, and solid-solid conversion sulfurized polyacrylonitrile (SPAN) cathodes are seldom discussed separately to contrast the fundamental limitations of conventional S_8 cathodes.

Against this background, this review establishes a triple classification system covering structural design, composite electrocatalysis and interfacial regulation, which covers nearly all mainstream sulfur cathode modification technologies. Each category is independently elaborated on their working mechanisms, typical

Accepted manuscript
This manuscript will be edited, formatted and proofread. The file will be replaced with Version of Record.

material systems and electrochemical performances. Critically, we conduct a targeted discussion on the unavoidable performance trade-offs when simultaneously applying multiple modification methods: for instance, high-porosity three-dimensional carbon frameworks enhance sulfur loading and expose abundant catalytic sites, but excessive pore volume reduces electrode compaction density and volumetric energy density; thick functional polymer/separator interlayers efficiently trap polysulfides, while simultaneously raising Li^+ diffusion impedance and deteriorating rate performance; high-loading catalytic nanoparticles improve redox kinetics yet aggravate metal ion dissolution and cross-talk between cathode and anode.

Notably, this work does not construct an idealized integrated synergistic model, as current research cannot provide sufficient quantitative experimental evidence to prove that multi-strategy combination achieves performance far exceeding the simple superposition of single modifications. Instead, we objectively dissect the compatibility barriers of cross-route combination, and separately analyze the application scenarios suitable for structural optimization, catalytic modification or interface regulation alone. In addition, SPAN-based covalent sulfur polymer cathodes with solid-solid conversion behavior are discussed in an independent chapter, whose unique reaction mechanism is compared with the liquid-solid multiphase transformation of elemental sulfur cathodes. At the end of this review, we summarize the bottlenecks of each single strategy, sort out unresolved contradictions in multi-technology coupling, and put forward differentiated research suggestions targeting practical pouch cell indicators (high areal loading, lean electrolyte, limited N/P ratio). This review aims to provide a comprehensive, critical reference for researchers to rationally select modification routes according to specific performance targets, rather than proposing a universal synergistic optimization framework.

Accepted manuscript
This manuscript will be edited, formatted and proofread. The file will be replaced with Version of Record.

List of abbreviations and symbols

1D — one-dimensional,

2D — two-dimensional,

3D — three-dimensional,

CNT — carbon nanotube,

COF — covalent-organic framework,

DFT — density-functional theory,

DME — 1,2-dimethoxyethane,

DOL — 1,3-dioxolane,

E/S ratio — electrolyte-to-sulfur ratio,

GO — graphene oxide,

HEA — high-entropy alloy,

HES — high-entropy sulfide,

ICP-MS — inductively coupled plasma-mass spectrometry,

KB — Ketjenblack,

LIBs — lithium-ion batteries,

Li-S — lithium-sulfur batteries,

LiPSs — lithium polysulfides,

MBene — metal boride,

MOF — metal-organic framework,

MXene — transition-metal carbide/nitride,

MWCNT — multi-walled carbon nanotube,

N/P ratio — negative-to-positive ratio,

PANI — polyaniline,

PEDOT — poly(3,4-ethylenedioxythiophene),

PE — polyethylene,

PP — polypropylene,

PPy — polypyrrole,

PTh — polythiophene,

Accepted manuscript
This manuscript will be edited, formatted, and proof read. The file will be replaced with Version of Record.

RGO — reduced graphene oxide,

SA — single-atom site,

SAC — single-atom catalyst,

SEI — solid-electrolyte interphase,

SEM — scanning electron microscopy,

SPAN — sulfurized polyacrylonitrile,

SPANI — sulfur-polyaniline,

XAS — X-ray absorption spectroscopy,

XRD — X-ray diffraction.

Accepted manuscript
This manuscript will be edited, formatted, and proof read. The file will be replaced with Version of Record.

2 Fundamentals and Core Bottlenecks of Sulfur Cathodes for Li-S Batteries

2.1 Cell Configuration and Electrochemical Reaction Mechanism of Li-S Batteries

A conventional Li-S battery primarily comprises several key functional components, including a sulfur-based cathode, a lithium metal anode, an organic electrolyte, a porous separator and metallic current collectors (**Figure 2a**). The fundamental principle of energy storage involves a multi-step redox reaction between sulfur and lithium, which enables the directed migration of lithium ions and electrons along with charge transfer, thus realizing the reversible conversion between chemical and electrical energy. The overall reaction of the battery system is expressed by Equation (1):[26, 27]

$$S_8 + 16Li^+ + 16e^- \leftrightarrow 8Li_2S \quad (1)$$

Specifically, as shown in **Figure 2b**, the discharge process of a Li-S battery follows a four-stage, multi-step reaction pathway.[28] It should be noted that electrochemical reactions take place only after the reactants (sulfur or lithium polysulfides) are sorbed onto the surface of electronically conductive components of the cathode. Furthermore, the redox conversion of sulfur and polysulfides is continuously accompanied by disproportionation and comproportionation reactions of lithium polysulfides, which accounts for the nearly horizontal second discharge plateau. Once formed, lithium polysulfides are solvated by solvent molecules, and such solvation modulates their electrochemical activity. In electrolyte media, lithium polysulfides can exist in both molecular and anionic forms, and these distinct species exhibit different electrochemical reactivities.[29, 30] The reaction characteristics, voltage ranges and corresponding equations for each stage are detailed as follows:

Stage I (Solid-Liquid Transformation, 2.6–2.3 V): Solid elemental sulfur (S_8) is reduced, and its ring-like molecular structure opens to generate soluble long-chain Li_2S_8 in the electrolyte. The reaction is shown in Equation (2):

$$S_8 + 2Li^+ + 2e^- \rightarrow Li_2S_8 \quad (2)$$

Accepted manuscript
This manuscript will be edited, formatted, and proof read. The final version will be replaced with Version of Record.

Stage II (Liquid-Liquid Transformation, 2.3–2.1 V): Li_2S_8 in the electrolyte is further reduced consecutively, and gradually transformed into medium-chain lithium polysulfides (Li_2S_6, Li_2S_4). This stage corresponds to the first voltage plateau in the discharge curve, as described by Equations (3) and (4):

$$3Li_2S_8 + 2Li^+ + 2e^- \rightarrow 4Li_2S_6 \quad (3)$$

$$2Li_2S_6 + 2Li^+ + 2e^- \rightarrow 3Li_2S_4 \quad (4)$$

Stage III (Liquid-Solid Transformation, ~2.1 V): Under critical reduction conditions, medium-chain Li_2S_4 further combines with lithium ions and electrons to form short-chain lithium polysulfides (Li_2S_2). This stage corresponds to the second voltage plateau, as shown in Equation (5):

$$Li_2S_4 + 2Li^+ + 2e^- \rightarrow 2Li_2S_2 \quad (5)$$

Stage IV (Solid-Solid Transformation, 2.1–1.7 V): Short-chain Li_2S_2 is continuously reduced and ultimately forms solid lithium sulfide (Li_2S) that is insoluble in the electrolyte and uniformly deposits on the cathode surface. The reaction is given by Equation (6):

$$Li_2S_2 + 2Li^+ + 2e^- \rightarrow 2Li_2S \quad (6)$$

The charging process is the thermodynamically reverse process of discharge. Driven by an applied electric field, solid Li_2S undergoes a multi-step oxidation reaction, passing through intermediates (e.g., Li_2S_2, Li_2S_4, Li_2S_6 and Li_2S_8), and is ultimately re-oxidized back to elemental sulfur.

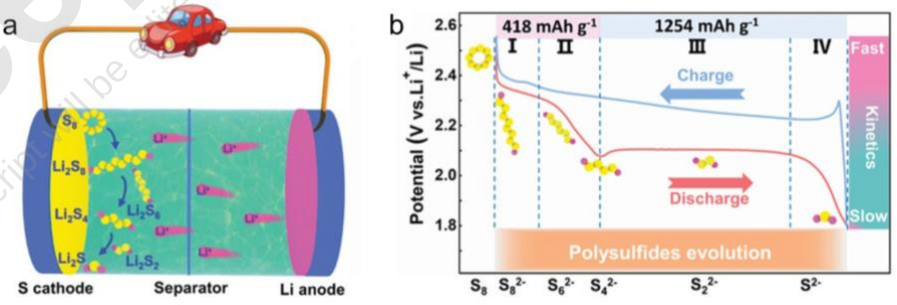


Figure 2. (a) Schematic diagram of the structure of conventional Li-S batteries. (b) Typical charge-discharge curve of Li-S batteries. Reproduced with permission. [28]Copyright 2021, Wiley-VCH.

Accepted manuscript
This manuscript will be edited, formatted and proof read. There will be replaced with Version of Record.

2.2 Four Dominant Obstacles

The charge-discharge cycling of Li-S batteries involves complex redox reactions with 16-electron transfer and solid-liquid-solid multiphase transformations. This inherent characteristic leads to several core technical bottlenecks that severely impede their commercialization. As the core component for energy storage and conversion, both the sulfur cathode and lithium anode suffer from pronounced performance drawbacks, giving rise to four primary challenges as detailed below. (**Figure 3**)[31, 32]

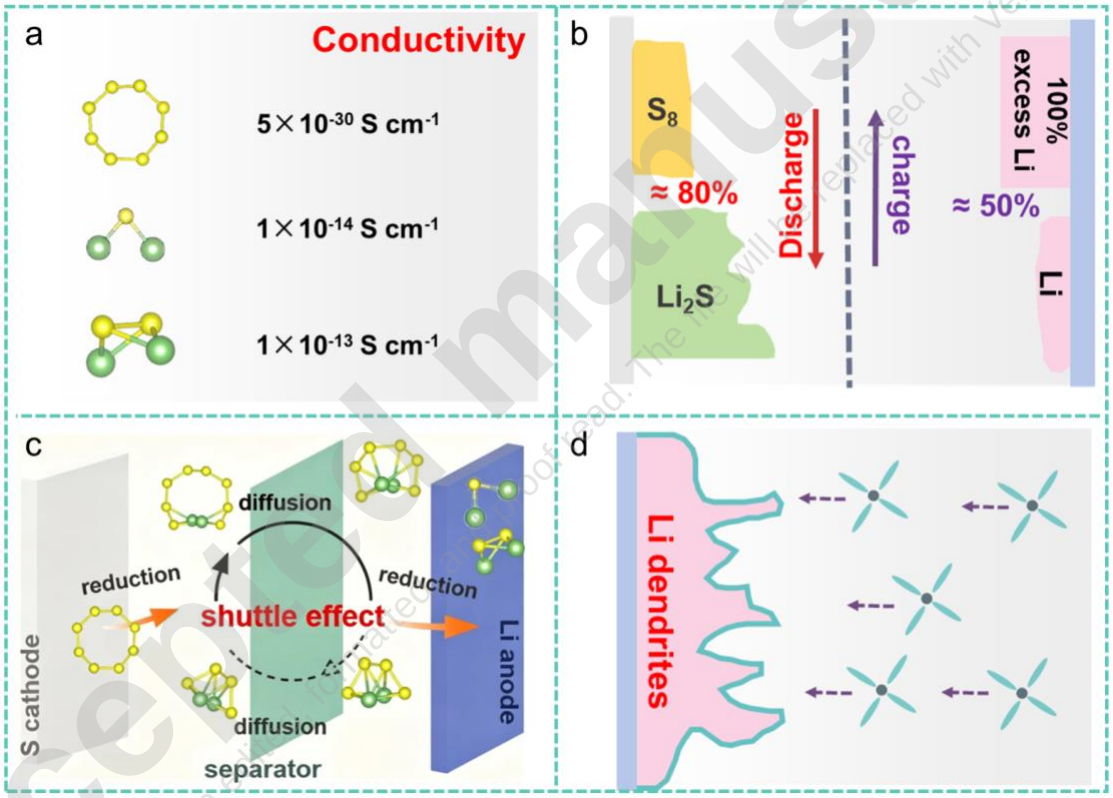


Figure 3. Key challenges in the practicalization of Li-S batteries.

2.2.1 Sluggish Electron/Ion Transport Kinetics

Elemental sulfur (S_8) and its main discharge products (Li_2S, Li_2S_2) possess extremely low electronic conductivities (approximately 5×10^{-30} S cm^{-1}, 1×10^{-14} S cm^{-1}, and 1×10^{-13} S cm^{-1}, respectively), which classifies them as electronic insulators. Furthermore, orthorhombic α-sulfur, consisting of discrete crown-shaped S_8 rings assembled via weak van der Waals interactions, exhibits a high

Accepted manuscript
This manuscript will be replaced with version of Record. The PDF will be updated with the final proofread.

lithium-ion diffusion energy barrier (0.6~0.8 eV) that severely restricts ion transport efficiency.[33] This dual insulating nature causes two major problems: first, the discharge product Li_2S can form a dense passivation layer on the electrode interface, reducing electrolyte wettability of the active materials; second, the hindered electron transport and lithium-ion diffusion drastically decrease the electrode reaction kinetics, manifesting as poor rate capability and low active material utilization.

2.2.2 Severe Volume Variation

Elemental sulfur possesses a theoretical density of 2.07 g cm^{-3}, whereas its fully lithiated discharge product Li_2S exhibits a lower theoretical density of only 1.66 g cm^{-3}.[34] The obvious density difference between sulfur and its lithiated product inevitably induces severe volume variation of sulfur-based electrode materials during cycling. The volume expansion ratio does not increase linearly with the loading mass of sulfur active materials, while the absolute volume expansion capacity rises synchronously with the increase of active material loading. Under high sulfur loading conditions, the excessive absolute volume fluctuation readily triggers electrode pulverization and fracture of internal conductive networks, which further destroys the stable electrode structure and eventually results in severe structural damage and rapid electrochemical capacity attenuation of the electrode.

2.2.3 Intrinsic Polysulfide Shuttle

The shuttle effect is an inherent core challenge of Li-S batteries. Its essence lies in the continuous dissolution, migration and deposition behavior of polysulfides during cycling. Long-chain polysulfides formed by sulfur conversion are highly soluble in conventional ether-based electrolytes and can diffuse across the separator toward the lithium metal anode. Upon arriving at the anode surface, these soluble long-chain polysulfides are reduced into insoluble short-chain polysulfides. Unlike long-chain species, short-chain polysulfides are poorly soluble in ether electrolytes and cannot diffuse back to the cathode. This

Accepted manuscript
This manuscript will be edited, formatted and proofread. The file will be replaced with Version of Record.

irreversible reduction and deposition process leads to permanent loss of sulfur active substances, severe corrosion of lithium anodes and aggravated side reactions of electrolytes. Such adverse reactions form a vicious cycle, ultimately inducing persistent performance degradation of lithium-sulfur batteries.

2.2.4 Disordered Growth of Lithium Dendrites

Despite the ultrahigh theoretical specific capacity and extremely low electrode potential of metallic lithium anodes, their intrinsically high chemical reactivity induces inhomogeneous Li deposition during electrochemical cycling and consequently the generation of lithium dendrites. The sharp protrusive structure of as-formed dendrites is capable of piercing the separator and incurring severe safety hazards; furthermore, the repetitive formation and fracture of dendrites trigger the accumulation of dead lithium and continuous depletion of electrolyte, which drastically deteriorate the Coulombic efficiency and cycling lifespan of batteries. Accordingly, lithium dendrite growth stands as one of the critical bottlenecks restricting the long-term cycling stability of lithium-sulfur batteries.[35, 36]

In summary, sulfur cathodes suffer from sluggish electronic/ionic transport kinetics, severe volume expansion and the notorious polysulfide shuttle effect, while metallic lithium anodes face critical safety concerns originating from uncontrolled lithium dendrite growth. Notably, the drawbacks of cathodes and anodes are not independent of each other; instead, they are dynamically coupled via the spatial shuttling of soluble polysulfides and inherent internal potential gradient inside cells, triggering synergistic degradation on both electrodes. Collectively, these drawbacks limit the cycling stability, rate capability, safety and reliability of Li-S batteries, constituting the primary bottlenecks impeding their commercialization. Tackling these obstacles via advanced performance optimization strategies, including rational cathode structural design, catalytic modulation and interfacial engineering, is essential to fabricate high-power and long-lifespan Li-S batteries. Detailed technical routes corresponding to these

Accepted manuscript
This manuscript will be edited, formatted and proofread. The file will be replaced with Version of Record.

optimization approaches will be elaborated in the following sections.

3 Structural Confinement Design for Physical Regulation

Structural design is critical physical regulation strategy to break through the performance of Li-S battery cathodes. Its optimization effect is closely related to the dimensional characteristics, microscopic morphology, and pore structure of the host materials. By rationally designing conductive frameworks with specific morphologies and structures, and then compounding them with sulfur active materials, multiple synergistic functions can be achieved at the physical level: on the one hand, continuous and efficient electronic/ionic transport pathways can be constructed, which significantly mitigates the intrinsic poor conductivity of sulfur and Li_2S; on the other hand, spatial confinement and structural deformation buffering can be utilized to effectively alleviate volume expansion during charge-discharge processes and suppress the dissolution and diffusion of polysulfides.[37, 38] This section systematically summarizes the regulation mechanisms and research progress of structural designs with different dimensions for Li-S battery cathodes, which are classified into 1D, 2D, and 3D structural systems (**Table 1**).

Table 1. Summary of sulfur cathode structure design for Li-S Batteries

Structure	Cathode	Sulfur content (wt%)/ Sulfur loading (mg cm^{-2})	Initial discharge capacity ($mAh\ g^{-1}$)/C-rate	Long-term cycling ($mAh\ g^{-1}$)/ cycles/C-rate	Electrolyte type	Refs.
1D structure	CNT-COPS@S	70/1.44±0.21	1128/0.1 C	576/100/0.5 C	Ether-based liquid	[39]
	$Te_{0.02}S_{0.98}$FPAN	49.0/1~1.4	764/0.2 C	641/500/1 C	Carbonate-based liquid	[40]
	S/HNT@C-3%	70/1~1.2	922.7/0.1C	329.5/500/1 C	Ether-based liquid	[41]
	SD-CNT@MoS_2-S	74.1/1.2	1144/0.1C	975/100/0.5 C	Ether-based liquid	[42]
	S@CNT@N/O-PC	75.2/1.3	1110/0.2 C	684/200/0.2 C	Ether-based liquid	[43]
	Fe_3O_4@S	57/-	964/0.2 C	316/120/0.5 C	-	[44]
	S@Fe/Ni-N-PCNSs	51.6/1	867/0.2 C	808/1000/0.2 C	Ether-based liquid	[45]
	S@$Fe(OH)_3$/MXene	67.4/-	1374.7/0.1 C	787.5/200/1 C	Ether-based liquid	[46]
2D structure	S@$FeTe_2$/CN	70.1/1	1353/0.1 C	504/430/1 C	Ether-based liquid	[47]
	S@CM@MX-2	-	1161.5/0.1 C	544.5/250/1 C	Ether-based liquid	[48]
	S/$Mo_{4/3}B_2$-MoS_2	70.2/1.5	1311.4/0.2 C	832/500/1 C	Ether-based liquid	[49]
	CNSs-Se@S	73/1.21	1418/0.1 C	852/150/0.2 C	Ether-based liquid	[50]

Accepted manuscript
This manuscript will be edited, formatted, and proofread. The final version will be published with Version of Record.

3D porous material	S@N_2RuCl_2/NCNS	70/5	965.3/0.1 C	801.4/200/0.1 C	Ether-based liquid	[51]
	S@HCS(1:2)	69.1/1	1346.5/0.1 C	417.8/1000/1 C	Ether-based liquid	[52]
	RPC-Co/S	79.1/-	1302.5/0.2 C	525.5/1000/1 C	Ether-based liquid	[53]
	Glyc-1/S	75/1.2	651/0.2 C	476/500/0.2 C	Ether-based liquid	[54]
	3DC-CNT/S	51.9/1.5	1363.9/0.1 C	633.4/800/0.2 C	Ether-based liquid	[55]
	UIPC/S	80.3/1~1.3	1311.5/0.1 C	520.7/300/1 C	Ether-based liquid	[56]
	MCS1	39/2~2.3	830/0.1 C	488/250/0.2 C	Ether-based liquid	[57]
	PDR-H/S	68.2/1~2	583.7/0.1 C	193.5/800/0.2 C	Ether-based liquid	[58]
	VNQDs/NOSHPC/S	76.3/5.2	1655/0.1 C	881/100/1 C	Ether-based liquid	[59]
	NATPC/S	73/-	1264.6/0.1 C	291/300/1 C	Ether-based liquid	[60]
	KOH@AVP/S	60.19/-	1501/0.1 C	590/800/1 C	Ether-based liquid	[61]
	S@CoNiM/CNTs	70/-	670.9/0.2 C	508.5/200/0.5 C	Ether-based liquid	[62]
	Co_3S_4-CoP/C@S	66.35/-	1178.2/0.1 C	740.4/300/1 C	Ether-based liquid	[63]
	Co_3S_4/MoS_2@Nfib-HCNFs/S	76.3/3.6	1282/0.1 C	449/500/1 C	Ether-based liquid	[64]
	NiCe@CPS	65.8/2	1013/0.1 C	609/100/0.1 C	Ether-based liquid	[65]
3D framework skeleton structure	Co-N/CBW/Li_2S_8	-/1.99	1213.1/0.1 C	590.3/200/0.5 C	Ether-based liquid	[66]
	S/VSe_2@VC/CNTs-350	70.5/-	1207.8/0.1 C	894.8/500/0.5 C	Ether-based liquid	[67]
	S@Ni-CN	72/1.7~2.5	1288.6/0.1 C	433.4/400/2 C	Ether-based liquid	[68]
	COF/MXene/S	50.7/1~1.5	1050/0.1 A g^{-1}	379/300/0.5 A g^{-1}	Ether-based liquid	[69]
	SPAN@CF-RGO	22/3	1548/0.1 C	584.3/300/2.5 C	Ether-based liquid	[70]
	S@MXene/CNT-1Zr	69.5/2	1285.8/0.1 C	381.1/1000/1 C	Ether-based liquid	[71]
	CVO@RGO/S	68.9/1	1150.82/0.1 C	887.04/500/0.5 C	Ether-based liquid	[72]
	TiC-Ti 3D framework@S	75/2	1506/0.1 C	488/500/1 C	Ether-based liquid	[73]
	WN@CNT-3/S	65/-	1512.6/0.1 C	687.2/200/1 C	Ether-based liquid	[74]
3D network cross-linked structure	S@rGO-void-$CoSe_2$	80.5/1.1~1.8	1124.2/0.1 C	270/1000/1 C	Ether-based liquid	[75]
	S@TiN/MC-CNT	63.7/-	1209.6/0.1 C	604.4/100/0.1 C	Ether-based liquid	[76]
	DC/$CoSe_2$-S	-/4	1524/0.1 C	825/400/1 C	Ether-based liquid	[77]
	CC@CNT/Ni-$Ni_{0.85}Se$-S	-/4	1563/0.1 C	770/200/3 C	Ether-based liquid	[78]

3.1 1D Host Architecture

1D structural materials are functional hosts constructed from high aspect ratio units (e.g., nanowires, nanotubes, nanofibers, nanorods and nanoribbons). Typical representatives include carbon nanotubes, electrospun nanofibers and 1D nanostructures of metal oxides/phosphides. Benefiting from their high aspect ratio and linear continuous morphology, 1D materials can construct highly interconnected conductive networks along the axial direction, providing fast transport channels for electrons and lithium ions and fundamentally improving

Accepted manuscript
This manuscript will be edited, formatted, and proofread. The file will be replaced with Version of Record.

the reaction kinetics of sulfur cathodes. Meanwhile, the flexible 1D structure can buffer the volumetric stress induced by sulfur lithiation through its own elastic deformation during cycling; the spatial barriers formed by their oriented arrangement can also restrict the lateral migration of lithium polysulfides, thus physically mitigating the shuttle effect.[79]

For instance, Liu et al.[80] designed and synthesized a 1D porous carbon-coated CoP nanotube composite (CoP@C), as shown in **Figure 4a**. This 1D structure not only significantly enhanced electrode conductivity, promoting rapid electron/ion transport and sufficient electrolyte infiltration, but also effectively buffered volume changes during cycling to maintain electrode structural integrity. The constructed CoP@C/MWCNT/S cathode delivered a high initial discharge capacity of 1237.6 mAh g^{-1} at 0.5 C with a sulfur loading of 1.4 mg cm^{-2}, and retained 92.3% of its capacity after 100 cycles. Xiang et al.[81] developed a 1D nanofiber-structured sulfurized polyacrylonitrile composite (SFPAN) and applied it as a cathode for Li-S batteries, as shown in **Figure 4b**. Leveraging the continuous conductive pathways formed by 1D nanofibers, the SFPAN cathode enabled rapid electron/ion transport, which significantly enhanced electrochemical performance under high-rate and low-temperature conditions. After 400 cycles at a current density of 0.3 A g^{-1}, the electrode still delivered a reversible specific capacity of nearly 1200 mAh g^{-1}. In another example, Yang et al.[82] prepared a hierarchically porous carbon material (FLHPC) with a 1D rod-like morphology from an Al-MOF precursor via high-temperature carbonization, as shown in **Figure 4c**. Elemental sulfur was effectively confined in the micro- and mesopores, while the macroporous channels provided rapid diffusion pathways for lithium ions. Wang et al.[83] designed and synthesized a 1D core-shell structured ZnO@NiO nanobelt (ZnO@NiO CNBs), as shown in **Figure 4d**. The heterogeneous interface formed a p-n junction, which further promoted interfacial charge transfer and catalytic conversion of polysulfides. Electrochemical tests showed that the ZnO@NiO CNBs electrode retained 73.6%

Accepted manuscript
This manuscript will be edited, formatted and proofread. The file will be replaced with Version of Record.

of its capacity after 1000 cycles at 2 C with a sulfur loading of 2 mg cm^{-2}, with an ultralow capacity decay rate of 0.026% per cycle.

In summary, benefiting from their high aspect ratio, 1D structures can simultaneously provide a conductive network, volume buffering and shuttle suppression. Such multifunctional features render 1D structures an important direction for sulfur cathode structural design. Different categories of 1D hosts exhibit distinct advantages and inherent limitations. Carbon-based 1D materials (e.g., carbon nanotubes, nanofibers) emphasize conductive continuity and structural flexibility, but their capability to chemically anchor lithium polysulfides is insufficient. Metal compound-based 1D structures (e.g., CoP nanotubes, ZnO@NiO nanobelts) introduce catalytic sites to combine physical confinement and chemical catalysis, at the expense of relatively low intrinsic electronic conductivity. Polymer-based 1D sulfurized polyacrylonitrile hosts achieve remarkable cycling stability and superior low-temperature performance, yet it remains difficult to reach high sulfur loading. The oriented arrangement, pore distribution and composite methods of 1D structures directly affect their performance; the design of hierarchical pores and core-shell heterostructures further improves mass transfer efficiency and catalytic activity. Practical bottlenecks mainly originate from two separate issues including poor structural uniformity during large-scale fabrication and inadequate chemisorption capacity toward lithium polysulfides. Future research should focus on precise structural regulation and coupling with active components to optimize the comprehensive performance under high sulfur loading, while balancing the trade-off between mechanical robustness, adsorption capability and electron transport to fulfill the practical requirements of high-energy-density lithium-sulfur cathodes.

Accepted manuscript
This manuscript will be edited, formatted and proofread. The file will be replaced with Version of Record.

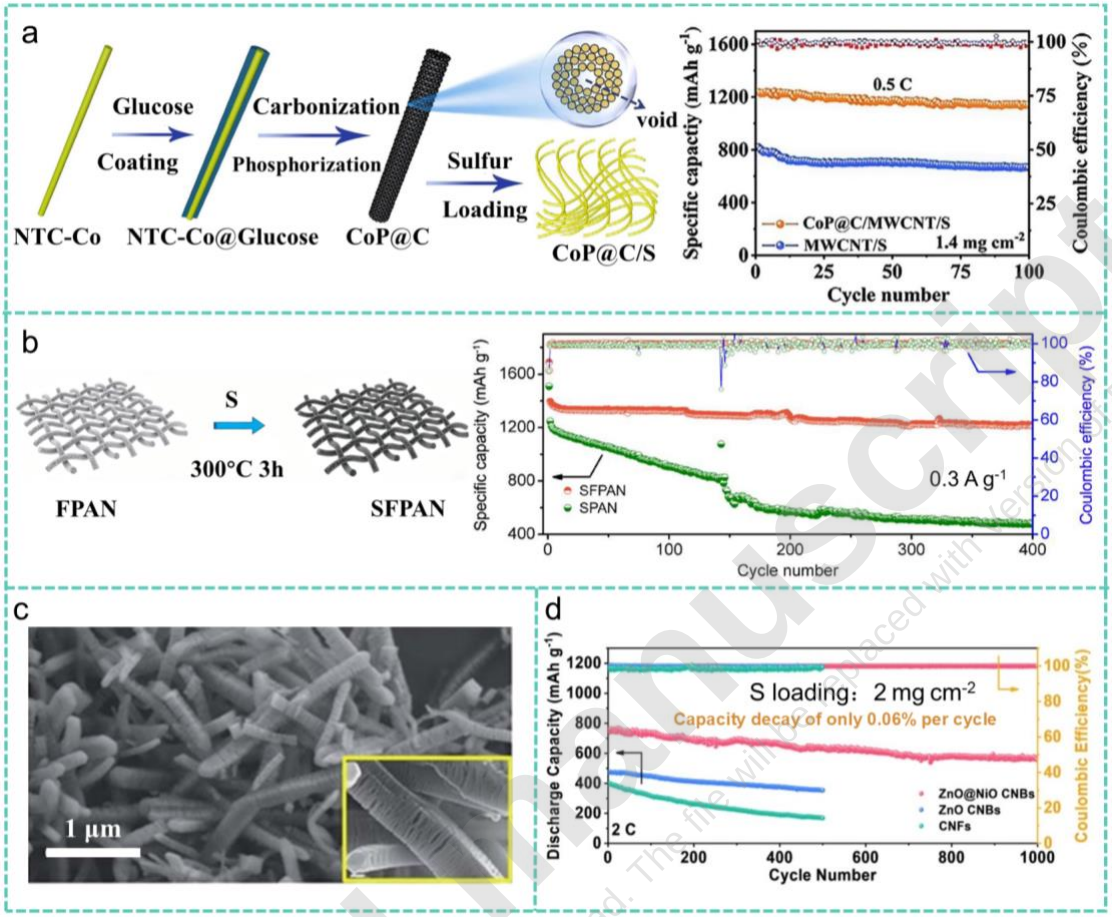


Figure 4. (a) Schematic diagram of the synthesis procedure for one-dimensional CoP@C/S nanostructures and the long-term cycling stability of the CoP@C/MWCNT/S electrode tested at 0.5 C (sulfur loading: 1.4 mg cm^{-2}). Reproduced with permission.[80] Copyright 2023, Elsevier. (b) Schematic illustration of the formation process of the SFPAN composite and its high electrochemical stability tested at 0.3 A g^{-1}. Reproduced with permission.[81] Copyright 2020, Elsevier. (c) SEM micrographs of S/FLHPC. Reproduced with permission.[82] Copyright 2015, Royal Society of Chemistry. (d) High electrochemical stability of the ZnO@NiO CNBs-based electrode tested at 2 C (sulfur loading: 2 mg cm^{-2}). Reproduced with permission.[83] Copyright 2024, Springer Nature.

3.2 2D Layered Host Design

Two-dimensional structural materials are functional materials characterized by

Accepted Manuscript
This manuscript will be edited, formatted, and proofread. This file will be replaced with Version of Record.

atomically thin layers and sheet/flake-like morphologies. Typical representatives include graphene, doped carbon nanosheets, MXenes, MBenes, 2D MOFs/COFs, and their derivatives.[84] 2D materials possess ultrahigh specific surface area, tunable interlayer spacing and abundant surface sites, which provide an ideal platform for uniform sulfur loading, rapid electron transport, and polysulfide immobilization.[85] Their large specific surface area enables highly dispersed sulfur loading, enhancing the conductive contact efficiency; their ordered layered spaces can form dual constraints of physical barriers and adsorption sites, effectively inhibiting polysulfide dissolution and shuttling; meanwhile, the interlayer gaps provide sufficient structural buffer space, alleviating volume expansion and maintaining electrode structural integrity.[86]

Li et al.[87] prepared a freestanding S@rGO-rGO composite cathode using a sulfur solution and reduced graphene oxide (rGO), as shown in **Figure 5a**. This 2D freestanding structure significantly enhanced structural stability and mass transfer efficiency. Jiang et al.[88] fabricated nitrogen-doped 2D wave-like carbon nanosheets (NCN) via a Pickering emulsion template method, as shown in **Figure 5b**. The unique wave-like 2D morphology not only accelerated lithium ion transport but also effectively regulated the dissolution and diffusion behavior of polysulfides. Furthermore, Li et al.[89] prepared porous $Ti_3C_2T_x$ (K-$Ti_3C_2T_x$) using a molten salt method combined with an alkali treatment strategy, as shown in **Figure 5c**. This 2D porous structure possessed abundant polysulfide anchoring sites, which significantly accelerated sulfur redox kinetics. The K-$Ti_3C_2T_x$@S electrode exhibited an ultralow capacity decay rate of only 0.047% per cycle over 500 cycles at 1 C with a sulfur loading of 1 mg cm^{-2}. Yang et al.[90] reported a 2D C_2N material loaded with high-loading, low-coordination Co single atoms (Co-SAs/C_2N) as an efficient sulfur host, as shown in **Figure 5d**. The S@Co-SAs/C_2N electrode still retained a high capacity retention of 80.9% after 2500 cycles at 3 C with sulfur loading approximately in the range of 1.0-1.2 mg cm^{-2}. Moreover, the S@Co-SAs/C_2N cathode achieved an areal capacity of

Accepted manuscript
This manuscript will be edited, formatted and proofread. The file will be replaced with Version of Record.

6.32 mAh cm^{-2} after 100 cycles at 0.2 C under a high sulfur loading of 8.1 mg cm^{-2}. In another instance, Wu et al.[91] prepared molybdenum nitride with a 2D nanochannel structure (2D-MoN_x), as shown in **Figure 5e**. Its interconnected 2D channels significantly enhanced the contact interface with polysulfides and catalytic conversion efficiency.

It is evident that 2D structures can simultaneously provide sulfur dispersion, enhanced mass transfer, shuttle suppression and volume buffering owing to their ultrahigh specific surface area, tunable interlayer spacing and abundant active sites. Such multifunctional characteristics establish 2D structures as a key direction for sulfur cathode optimization. Nevertheless, different categories of 2D hosts also exhibit inherent limitations alongside their respective strengths. Different types of 2D materials have distinct advantages. Carbon-based materials (e.g., graphene, carbon nanosheets) excel in conductivity and structural support, yet they mainly rely on physical confinement with weak chemical adsorption toward lithium polysulfides. Polar materials (e.g., MXene, MoN_x) enhance polysulfide anchoring and catalysis, but they often suffer from severe interlayer restacking and relatively high preparation costs. Single-atom loaded 2D materials (e.g., Co-SAs/C_2N) realize the precise coupling of adsorption and catalysis, whereas the synthesis complexity and cost restrict scalable production. Designs involving interlayer spacing regulation, porous structure construction and single-atom modification further enhance the overall performance of the materials. Current challenges include interlayer stacking under high sulfur loading and high costs of large-scale preparation. Future research should focus on precise "structure-composition-function" matching and utilize interface engineering and multi-component compounding to optimize the high-rate and long-cycle stability. Meanwhile, it is necessary to balance the intrinsic trade-off among interlayer anti-restacking ability, active-site density and material cost to accelerate the practical deployment of 2D sulfur cathode materials.

Accepted manuscript
This manuscript will be edited, formatted and proofread. The file will be replaced with Version of Record.

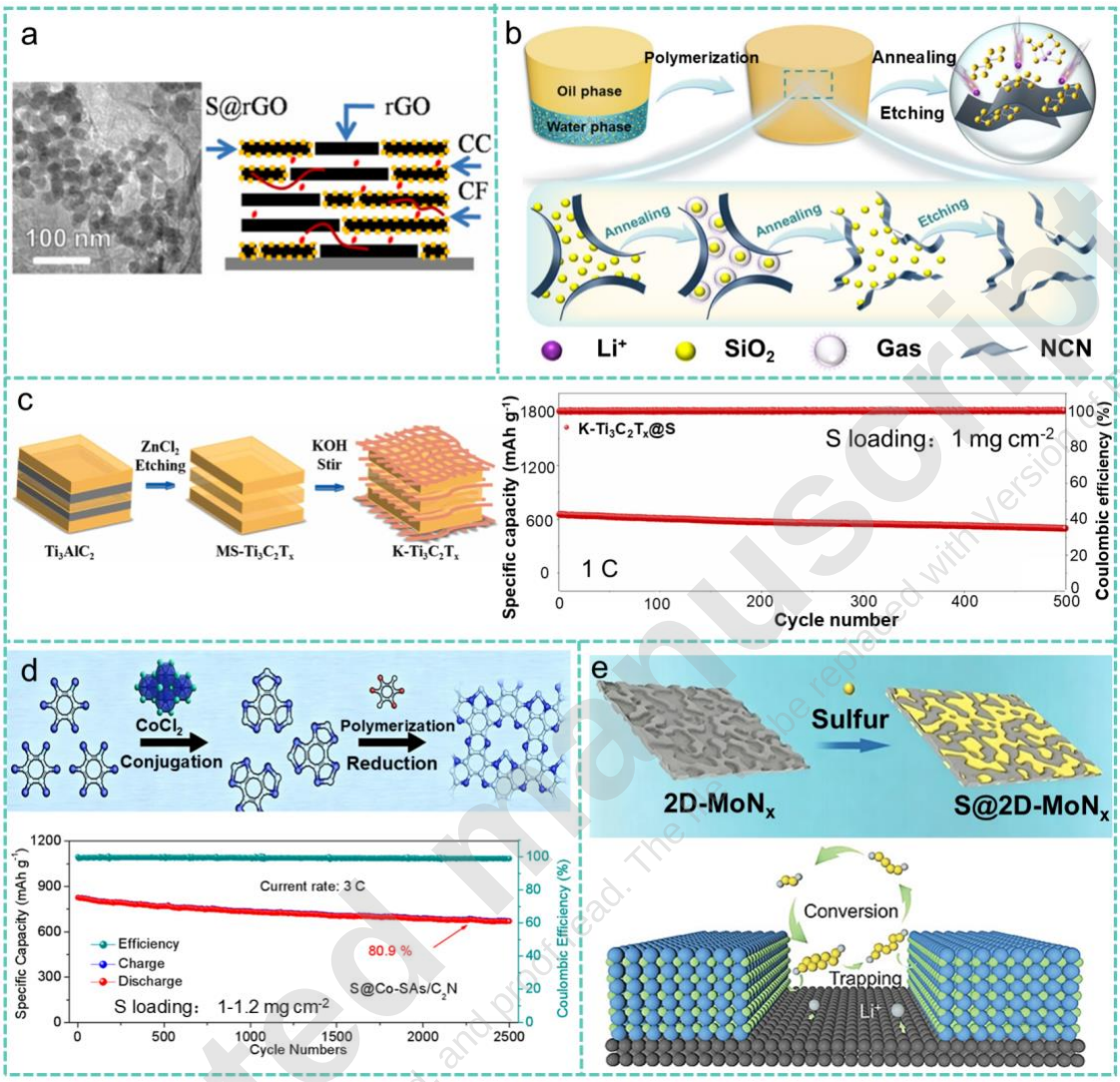


Figure 5. (a) TEM micrograph of S@rGO and schematic illustration of S@rGO-rGO. Reproduced with permission.[87] Copyright 2024, Elsevier. (b) Schematic illustration of the NCN fabrication process. Reproduced with permission.[88] Copyright 2025, American Chemical Society. (c) The fabrication process of K-$Ti_3C_2T_x$ material and the long-term cycling stability of the K-$Ti_3C_2T_x$@S electrode tested at 1 C (sulfur loading: 1 mg cm^{-2}). Reproduced with permission.[89] Copyright 2025, Elsevier. (d) Schematic illustration of Co-SAs/C_2N synthesis and long-term cycling stability of the S@Co-SAs/C_2N electrode tested at 3 C (sulfur loading: 1-1.2 mg cm^{-2}). Reproduced with permission.[90] Copyright 2024, American Chemical Society. (e) Schematic illustration of ultra-thin 2D molybdenum compounds synthesis and the catalytic

Accepted manuscript
This manuscript will be edited, formatted, and proofread. The final version may be replaced with Version of Record.

mechanism of S@2D-MoN_x at the cathode interface. Reproduced with permission. [91] Copyright 2024, Wiley-VCH.

3.3 3D Hierarchical Hosts

Three-dimensional structural materials are 3D frameworks characterized by continuous extension and interconnection in all three spatial dimensions, which usually exist as porous structures, framework structures or cross-linked networks. In Li-S systems, 3D structures can construct all-around conductive pathways, meeting the multiple demands of high sulfur loading, rapid mass transfer and structural stability. Their internally interconnected pore systems not only provide sufficient buffer space for volume expansion but also effectively anchor polysulfides for the long term through physical confinement, high specific surface area adsorption, and exposed active sites and other actions, thus addressing the three core issues of poor conductivity, volume deformation, and the shuttle effect simultaneously.[92, 93]

Based on construction methods and structural characteristics, this section further categorizes 3D structures into three types for systematic elaboration: three-dimensional porous structures, three-dimensional framework structures and three-dimensional network cross-linked structures.

3.3.1 3D Porous Structure

The three-dimensional porous structure is the most commonly used microstructural design for Li-S battery cathodes. Specifically, it refers to three-dimensional carbon-based or carbon-inorganic composite structures with hierarchical pore channels (micropores/mesopores/macropores), which are typically fabricated via template synthesis, chemical activation, magnesiothermic reduction, biomass-based self-pore-forming and other methods. Hierarchical pore architectures enable functional synergy: micropores/mesopores are responsible for sulfur loading and polysulfide confinement, while macropores facilitate rapid ion transport and electrolyte

Accepted manuscript
This manuscript will be edited, formatted, and proofread. The final version will be published with Version of Record.

penetration.[94, 95]

For instance, Yu et al.[96] prepared titanium monoxide-modified three-dimensional nitrogen-doped graphitized porous carbon (TiO-NGPC) via a magnesiothermic reduction method, as shown in **Figure 6a**. The three-dimensional interconnected carbon skeleton provided efficient electron transport pathways, while the polar TiO nanoparticles served as strong anchoring sites for polysulfides, accelerating catalytic conversion and suppressing the shuttle effect. Under an ultrahigh sulfur loading of 8.97 mg cm^{-2}, the TiO-NGPC/S cathode achieved an areal capacity of 9.87 mAh cm^{-2}, showcasing great practical promise. Zhang et al.[97] utilized ZnO as a hard template and furfuryl alcohol (FA) as a carbon source to prepare hierarchical porous carbon (HPC), which was subsequently modified with nitrogen doping and Ni/Co dual atoms to obtain a high-performance sulfur host, as shown in **Figure 6b**. The Microwave C-2.5%Ni2.5%Co electrode achieved a reversible specific capacity of 902.8 mAh g^{-1} after 500 cycles at 1 C with a sulfur loading of 6.2 mg cm^{-2}, corresponding to a capacity retention of 74%. Huangfu et al.[98] synthesized N/P co-doped porous carbon (N/P-LPC-900) via a chemical activation method, as shown in **Figure 6c**. Its microporous structure provided strong physical confinement, while the N and P polar sites enhanced adsorption and catalysis, effectively confining the sulfur conversion process within the pore channels. Yang et al.[99] used moso bamboo as a raw material to prepare microporous carbon (MPC) through direct carbonization-induced self-pore-forming, which was then combined with sulfur to obtain an MPC@S cathode, as shown in **Figure 6d**. Such low-cost renewable biomass resources demonstrated significant potential for scalable preparation and industrial application.

Accepted manuscript
This manuscript will be edited, formatted and proofread. The file will be replaced with the Version of Record.

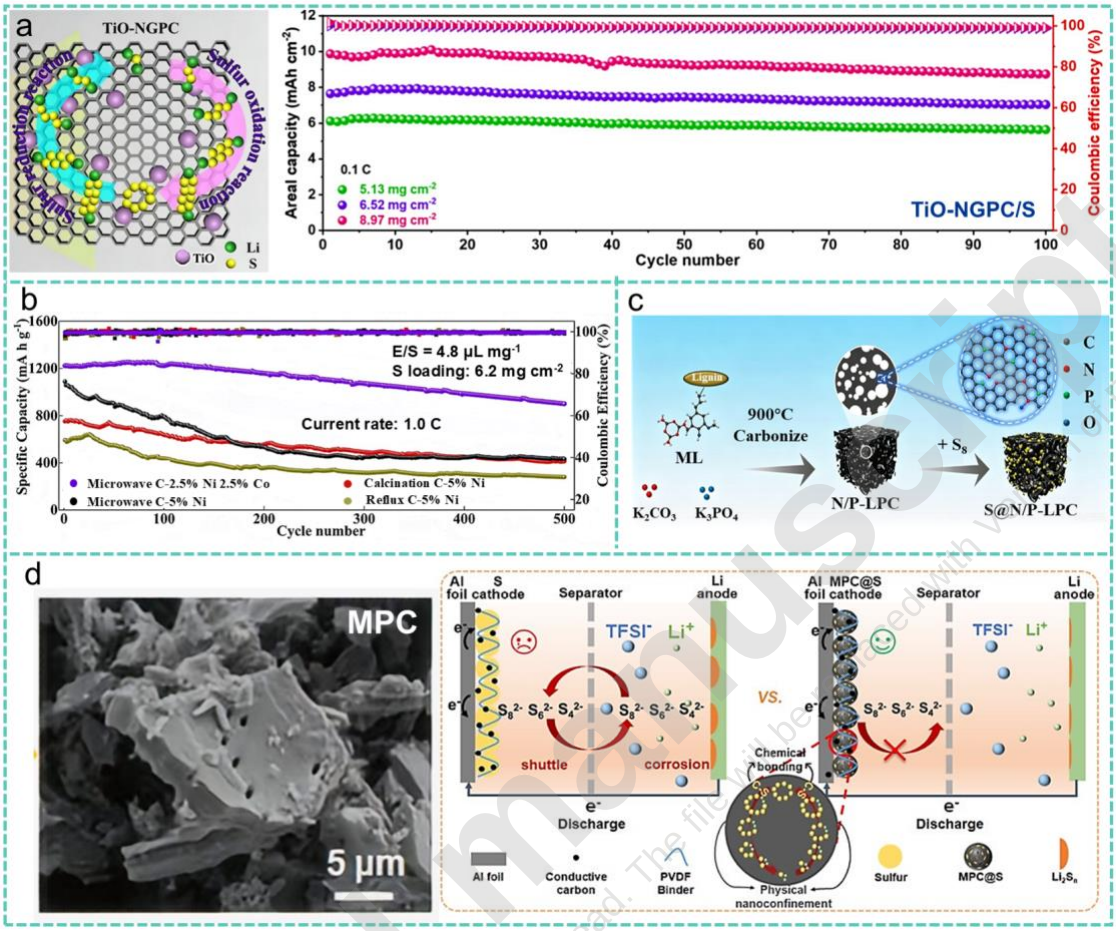


Figure 6. (a) Reaction mechanism of the TiO-NGPC/S cathode and cycling stability of high-loading TiO-NGPC/S cathodes tested at 0.1 C with sulfur loadings of 5.13, 6.52, and 8.97 mg cm^{-2}. Reproduced with permission.[96] Copyright 2025, American Chemical Society. (b) High cycling stability of the Microwave C-2.5%Ni-2.5%Co electrode tested at 1 C (sulfur loading: 6.2 mg cm^{-2}). Reproduced with permission.[97] Copyright 2025, Royal Society of Chemistry. (c) The preparation flow chart of S@N/P-LPC. Reproduced with permission.[98] Copyright 2025, Wiley-VCH. (d) SEM images of MPC and schematic profile of the Li-S battery with MPC@S cathode. Reproduced with permission.[99] Copyright 2025, American Chemical Society.

Current research shows that 3D porous structures have become a core design strategy for balancing high sulfur loading and long-term cycling stability owing to their hierarchical pore features. Micropores and mesopores confine sulfur and

Accepted manuscript
This manuscript will be edited, formatted and proofread. The final version may differ from this version of Record.

polysulfides while macropores accelerate mass transfer. Nevertheless, different types of 3D porous hosts possess distinct merits and inherent limitations. Carbon-based porous materials integrate physical confinement and chemical adsorption or catalysis via heteroatom doping, inorganic particle decoration or dual-atom modification, which significantly improves their electrochemical performance, yet excessive doping or inorganic loading may reduce pore volume and tap density. Biomass-derived porous carbons have the advantages of low cost and environmental friendliness, demonstrating great potential for industrialization, but they remain difficult to achieve controllable and uniform pore structure. Current challenges lie in the precise regulation of hierarchical pore sizes, prevention of pore blockage under high sulfur loading, and improvement of scaling-up preparation efficiency. Future research should focus on pore structure optimization and precise implantation of active sites and utilize innovative preparation processes and multi-component design to further enhance the mass transfer efficiency and cycling stability at high rates.

3.3.2 3D Framework Skeleton Structure

The 3D skeleton structure is a system constructed from building blocks such as MOFs, COFs, ordered mesoporous carbon, or hollow carbon spheres that are assembled, derived or compounded into a 3D framework with regular topology and rigid support. It is characterized by structural regularity, uniform pore channels, highly designable functional sites, excellent mechanical stability and structural controllability.[100]

For example, Lv et al.[101] synthesized a 3D COF (NiS_4-TAPT) constructed from nickel-bis(dithiolene) and N-rich triazine units, as shown in **Figure 7a**. This material featured 3D ordered pore channels and high-density N sites; the Li@NiS_4-TAPT‖S@NiS_4-TAPT full battery maintained a specific capacity of 620.2 mAh g^{-1} after 400 cycles at 1 C with a sulfur loading of ~2 mg cm^{-2}. He et al.[102] synthesized a β-ketoenamine-based 3D COF (TT COF) via a room-temperature Schiff base reaction, as shown in **Figure 7b**. Its 3D network

Accepted manuscript
This manuscript will be edited, formatted and proofread. There will be replaced with Version of Record.

structure significantly enhanced specific surface area and ion transport efficiency, achieving a discharge specific capacity of 490.6 mAh g^{-1} after 2000 cycles at 2 C. Mu et al.[103] anchored ultrafine CoFeP nanoparticles in-situ onto hollow mesoporous carbon spheres (HMCS), preparing a CoFeP@HMCS composite sulfur host, as shown in **Figure 7c**. This 3D framework afforded triple functionality of efficient electron conduction, strong adsorption and high catalytic activity, endowing the assembled Li-S battery with excellent long-term cycling performance. Under a high sulfur loading of 8.2 mg cm^{-2} and a low E/S ratio of 4.8 μL mg^{-1}, the resultant battery retained a high areal capacity of 6.06 mAh cm^{-2} after 200 cycles. Zhang et al.[104] designed an Fe_3O_4-doped carbon cube material with an interlocked tube-network structure (SP-Fe_3O_4-C), as shown in **Figure 7d**. The 3D continuous pore channels, carbon-based conductive network and polar Fe_3O_4 sites synergistically realized rapid charge transfer, strong polysulfide capture, and efficient catalysis. SP-Fe_3O_4-C/S cathode delivered a high areal capacity of 6.5 mAh cm^{-2} after 60 cycles at a sulfur loading of 8.2 mg cm^{-2}.

Such advanced functional organic frameworks and inorganic–carbon composite skeletons can simultaneously integrate porous architectures, conductive networks and catalytic active sites. Nevertheless, different categories of these skeletons possess distinct merits and inherent limitations. 3D COF skeletons have regular, tunable pore channels and designable polar sites to modulate polysulfide conversion, yet their complicated synthesis and high cost hinder scalable production. Transition metal phosphide/carbon composite skeletons offer strong adsorption and high catalytic activity, while nanoparticle agglomeration reduces accessible active sites. Metal-oxide-incorporated carbon skeletons realize synergistic polysulfide anchoring and redox catalysis, though heavy metal oxides compromise gravimetric specific capacity. Interface and nanoscale structural engineering further optimize electrochemical performance. Current structural challenges include high synthesis costs of crystalline

Accepted manuscript
This manuscript will be edited, formatted and proof read. There will be replaced with Version of Record.

frameworks and uncontrolled agglomeration of inorganic catalytic nanoparticles. Toward industrial deployment, future structural design should simplify fabrication routes and tailor the spatial distribution of active sites to achieve high sulfur loading and stable cycling under lean-electrolyte conditions while balancing electrode compactness and volumetric energy density.

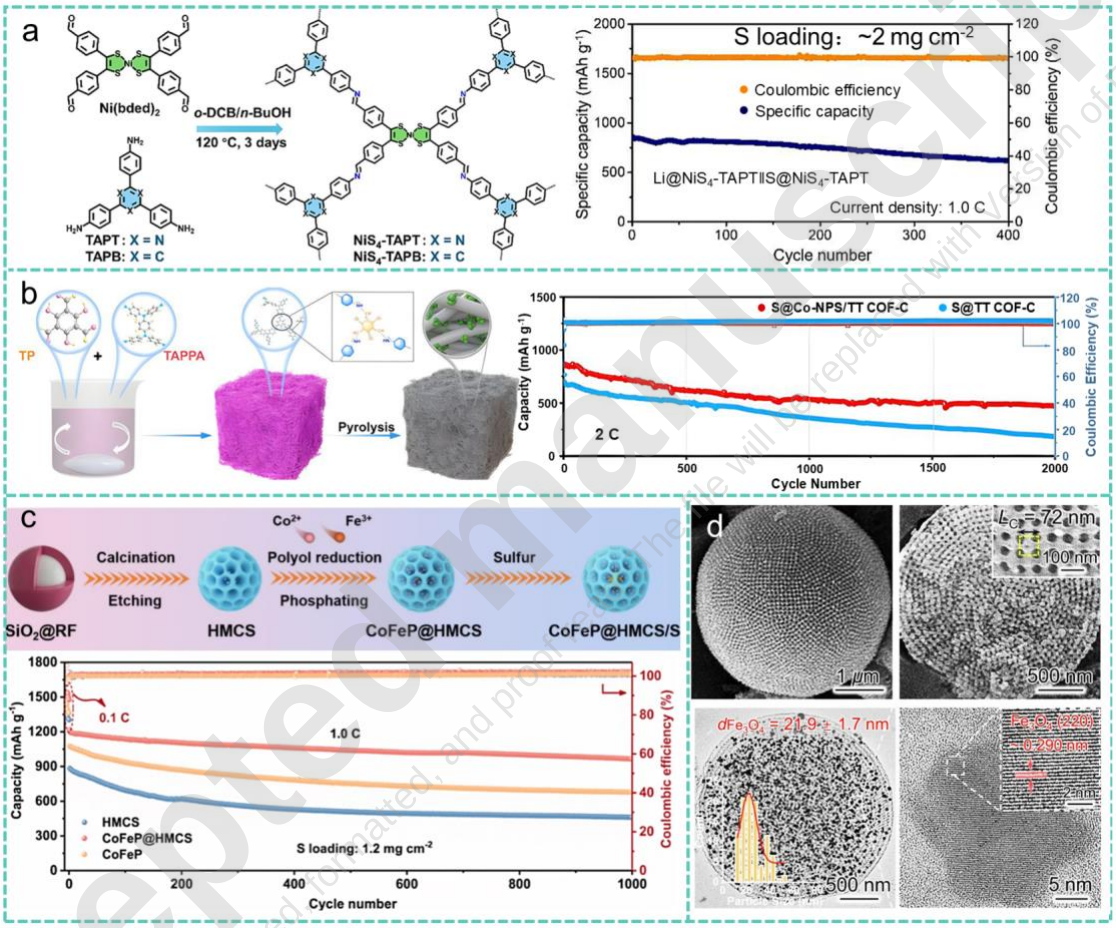


Figure 7. (a) Schematic diagram of the synthesis processes of NiS_4-TAPT and NiS_4-TAPB and the long-term cycling stability of Li@NiS_4-TAPT‖S@NiS_4-TAPT full battery tested at 1 C (sulfur loading: ~2 mg cm^{-2}). Reproduced with permission.[101] Copyright 2024, American Chemical Society. (b) Schematic illustration of the procedure for Co-NPs/TT COF-C and the cycling stability of S@Co-NPs/TT COF-C electrode tested at 2 C. Reproduced with permission.[102] Copyright 2025, Springer Nature. (c) Schematic illustration of CoFeP@HMCS/S fabrication and the cycling stability of its electrode tested at 1 C (sulfur loading: 1.2 mg cm^{-2}). Reproduced with permission.[103] Copyright

Accepted manuscript
This manuscript will be edited, formatted, and proofread. The title will be replaced with Version of Record.

2026, Elsevier. (d) SEM image and TEM image of an SP-Fe_3O_4-C cubosome. Reproduced with permission.[104] Copyright 2024, Springer Nature.

3.3.3 3D Network Cross-Linked Structure

The 3D network cross-linked structure is an interpenetrating network formed by low-dimensional building blocks such as carbon nanotubes, graphene sheets, metal clusters, or functional organic units, interconnected via covalent bonds, coordination bonds, π-π interactions, or chemical cross-linking. Its core advantages include high electrical conductivity, high structural flexibility, high porosity, and robust structural stability, which enable efficient accommodation of volume expansion and maintenance of electrode integrity.[105]

For instance, Xu et al.[106] loaded sulfur onto hydroxylated carbon nanotubes and then compounded them with 2D Cu-TCPP nanosheets (TCPP=tetrakis(4-carboxyphenyl)porphyrin) to construct a 3D network cross-linked composite material (Cu-TCPP@CNT-OH-S), as shown in **Figure 8a**. This cathode achieved a high initial specific capacity of 1448 mAh g^{-1} at 0.2 C and maintained a stable specific capacity of 820 mAh g^{-1} after 1000 cycles. In a Li-S pouch cell, a reversible areal capacity of 4.3 mAh cm^{-2} was obtained at 2 C after 100 cycles with a sulfur loading of 10.04 mg cm^{-2}. Xi et al.[107] prepared a WO_3@CNT-C_{ZIF-8}/S composite with a 3D network structure, as shown in **Figure 8b**, where CNTs, C_{ZIF-8} and WO_3 were interconnected into a hierarchical architecture with enhanced conductivity, structural stability and polysulfide confinement. Zhu et al.[108] coordinated Ni/Cu bimetallic centers onto tetraaminophthalocyanine (TaPc) and then chemically cross-linked the product with carbon nanotubes, constructing a stable 3D cross-linked sulfur host (TaPcNiCu/CNTs), as shown in **Figure 8c**. Zhou et al.[109] prepared strutted graphene foam (SG) with an interconnected network and abundant defects, and directly used it as a sulfur host, as shown in **Figure 8d**. The 3D graphene network significantly enhanced conductivity, buffers volume deformation, and suppresses the shuttle effect. The S/SG cathode retained a specific capacity of 691 mAh g^{-1} after 500 cycles at 2 C

Accepted manuscript
This manuscript will be edited, formatted, and proofread. The final version may be replaced with Version of Record.

with a sulfur loading of 3.5 mg cm^{-2}.

It is noteworthy that the 3D network cross-linked structure can simultaneously deliver high conductivity, high flexibility and high porosity by virtue of the interpenetration and strong interactions of 2D building blocks. Such structural features help accommodate sulfur volume expansion efficiently and preserve electrode integrity. Nevertheless, different component combinations of such cross-linked networks show distinct strengths and inherent limitations. Typical high-porosity carbon materials such as graphene foam can effectively buffer sulfur volume expansion and construct unobstructed ion transport channels, yet they usually exhibit an extremely low tap density below 0.5 g cm^{-3}, resulting in a volumetric energy density less than 400 Wh L^{-1}, which is far lower than the minimum threshold over 700 Wh L^{-1} required for industrial application. Carbon-based units (e.g., carbon nanotubes, graphene) construct the conductive network, while metal clusters or functional organic units enhance polysulfide adsorption and catalysis, but the introduction of multi-functional components may increase the complexity of synthesis and affect the overall porosity. The combined structural features of these components greatly improve cycling stability and capacity retention. Current research on structural design mostly focuses only on gravimetric specific capacity while ignoring volumetric electrochemical performance. Current challenges include precise control of the cross-linking degree and optimization of mass transfer efficiency under high sulfur loading. Accordingly, subsequent studies are required to simultaneously report volumetric capacity (mAh cm^{-3}) and electrode compaction density, so as to balance electrochemical performance and practical application requirements. Future research should focus on multi-component structural design and simplification of preparation processes to further strengthen structural stability and catalytic activity, promoting their application in high-performance Li-S batteries.

Accepted manuscript
This manuscript will be edited, formatted and proofread. The file will be replaced with Version of Record.

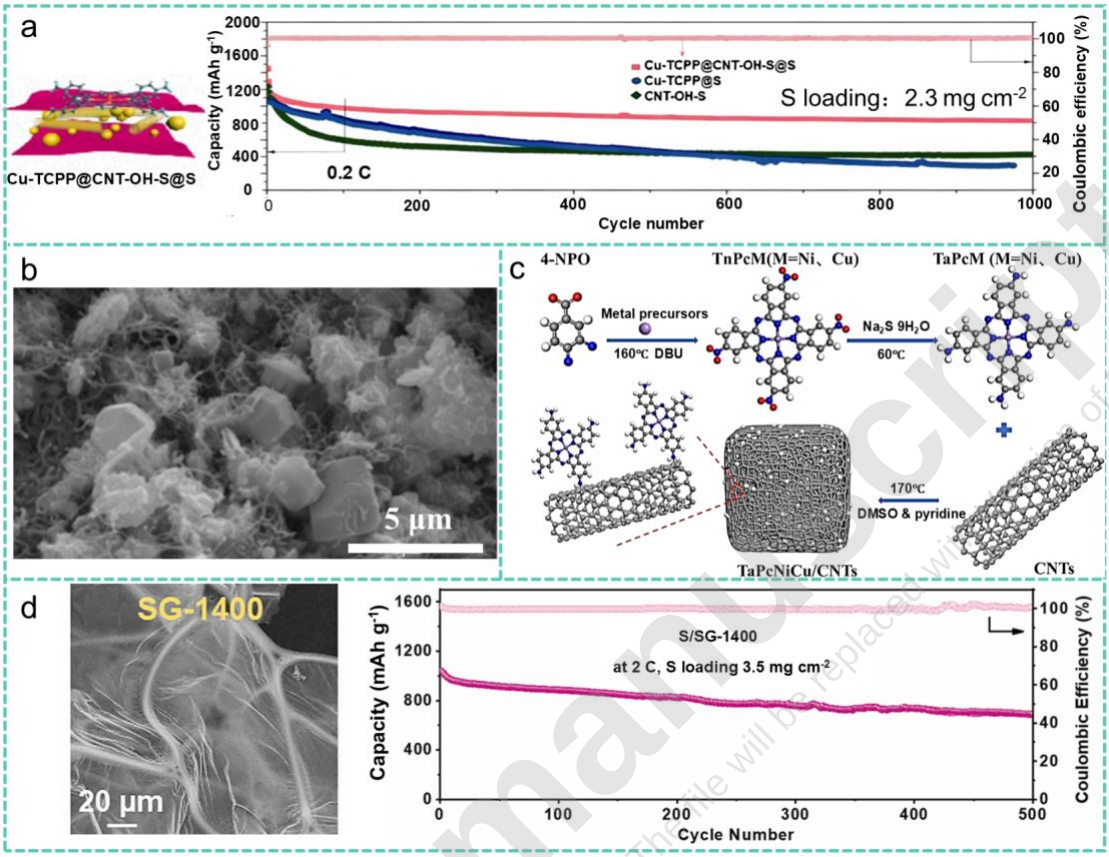


Figure 8. (a) Scheme of Cu-TCPP@CNT-OH-S and high electrochemical stability of its electrode tested at 0.2 C (sulfur loading: 2.3 mg cm^{-2}). Reproduced with permission.[106] Copyright 2024, Elsevier. (b) SEM image of WO_3@CNT-C_{ZIF-8}. Reproduced with permission.[107] Copyright 2025, Elsevier. (c) Synthesis illustration of TaPcNiCu/CNTs composites. Reproduced with permission.[108] Copyright 2026, Elsevier. (d) SEM image of SG and long-term cycling stability of S/SG electrode tested at 2 C (sulfur loading: 3.5 mg cm^{-2}). Reproduced with permission.[109] Copyright 2024, Elsevier.

3.4 Critical discussion on structural design and its conflicts with catalytic/interface strategies

One-dimensional, two-dimensional and three-dimensional host structures can physically confine sulfur species and construct rapid charge transport pathways, yet this type of structural optimization faces inherent limitations when matched with catalytic or interfacial modification. Hierarchically porous carbon

Accepted manuscript
This manuscript will be edited, formatted, and proofread. The file will be replaced with the Version of Record.

substrates with large specific surface areas can load abundant catalytic nanoparticles, but high porosity lowers electrode tap density and volumetric energy density, which conflicts with the industrial demand for compact thick electrodes. If dense conductive frameworks with low porosity are adopted to improve volumetric performance, the exposed catalytic active sites will be drastically reduced, weakening polysulfide conversion kinetics. Meanwhile, when paired with thick functional separator/interlayer coatings for shuttle suppression, the ion transport channels constructed by porous structures will be partially blocked, further deteriorating rate capability. At present, most structural host research only reports gravimetric capacity under low E/S ratio and low sulfur loading, while systematic data matching lean-electrolyte industrial conditions are insufficient. Simply combining structural confinement with catalytic or interfacial strategies cannot eliminate the above trade-offs, and targeted quantitative design of pore size, compaction density and catalyst loading is still lacking in existing literature, which requires careful parametric screening to balance volumetric energy density, catalytic conversion activity and ion transport property for thick electrode design.

4 Composite Electrocatalysis for Accelerated Redox Kinetics

The primary objective of composite catalysis strategies is to enhance the electrochemical reaction kinetics of sulfur cathodes. By introducing highly active catalytic components, these strategies effectively reduce the energy barriers of polysulfide redox reactions and accelerate the reversible conversion rate of polysulfides. This chemically suppresses the dissolution, accumulation, and shuttle effect of polysulfides, thus synergistically improving sulfur utilization, cycling stability, and rate capability.[110-112] The sulfur species follow a typical electrochemical conversion sequence: S_8, Li_2S_8, Li_2S_6, Li_2S_4, Li_2S_2, Li_2S. Among the whole reaction process, the liquid-solid nucleation of Li_2S_4 to Li_2S_2 and the solid-solid transformation from Li_2S_2 to Li_2S are universally regarded as rate-determining steps.[113] According to practical functions, electrocatalysts can

Accepted manuscript
This manuscript will be edited, formatted and proofread. The file will be replaced with Version of Record.

be classified into three types: polysulfide capture and enrichment type, electron transfer activation type, and nucleation template type. The construction of active sites complies with distinct modulation rules. The catalytic performance of metal-based catalysts is dominated by the d-band center theory; the intrinsic activity of single-atom catalysts is closely associated with metal-sulfur coordination numbers; the synergistic effect of composite catalysts stems from interfacial charge redistribution of heterostructures. It should be noted that many published studies claim electrocatalytic activity merely based on battery cycling performance and DFT-calculated adsorption energies. Nevertheless, these two indicators alone are inadequate to confirm the improvement of redox reaction kinetics. Sufficient kinetic validation usually requires complementary experimental characterizations such as symmetric-cell cyclic voltammetry, Li_2S potentiostatic tests, activation energy calculation derived from variable-temperature electrochemical measurements, and in-situ characterizations, rather than over-reliance on battery capacity and cycling stability. Most current DFT simulations adopt static models, which fail to simulate actual solvent environments and dynamic surface reconstruction behaviors. Therefore, it is essential to implement in-situ dynamic investigations combined with operando characterizations including XRD, Raman and XAS. This section categorizes composite catalytic systems into three main types based on the nature of the catalytic active components: carbon-based catalytic systems, MOF-based catalytic systems, and metal-based catalytic systems. Their structural design, working mechanisms and research progress are systematically discussed.

4.1 Carbon-based Catalytic Systems

Carbon-based materials have broad application prospects in the catalytic modification of Li-S batteries owing to their high electrical conductivity, large specific surface area, chemical stability and cost advantages. However, pristine carbon materials have limited intrinsic catalytic activity. To overcome this limitation and move beyond the reliance of traditional carbon hosts solely on

Accepted manuscript
This manuscript will be edited, typeset and proofread. The file will be replaced with Version of Record.

physical confinement, strategies such as heteroatom doping (N, P, S, F, etc.), defect engineering and non-metal single atom loading are adopted. These methods construct high-density active sites on the carbon matrix surface, enabling strong chemisorption and efficient electrocatalytic conversion of polysulfides, which makes carbon-based systems a mainstream catalytic approach balancing performance and economy.[114]

For example, Hong et al.[115] prepared polyimide-derived N/O co-doped nanosheet-modified carbon cloth (NOCC) via in-situ imidization and high-temperature carbonization, and used it as a flexible freestanding sulfur host, as shown in **Figure 9a**. The N and O dual-doping sites provided bifunctional capabilities for strong polysulfide adsorption and efficient catalytic conversion, significantly accelerating redox kinetics. The NOCC@S cathode delivered a discharge specific capacity of 485 mAh g^{-1} after 700 cycles at 2 C with a sulfur loading of 1.5 mg cm^{-2}. Under high sulfur loading of 4.0 mg cm^{-2} and lean-electrolyte condition (E/S ratio=10 μL mg^{-1}), it achieved an initial areal capacity of 3.7 mAh cm^{-2} at 0.1 C. Li et al.[116] synthesized N/P co-doped honeycomb-like porous carbon (NPC) through resin pyrolysis and combined it with carbon nanotubes to construct a freestanding NPC@CNTs membrane electrode, as shown in **Figure 9b**. This hierarchical conductive structure facilitated rapid ion transport and sufficient electrolyte infiltration. Li et al.[117] designed a lithiophilic N-doped carbon-supported single-atom iodine catalyst (SAI-NC), as shown in **Figure 9c**. The C-N-I covalent bonds ensured high dispersion of iodine atoms, strengthening the chemical anchoring of polysulfides while providing efficient catalytic sites. This effectively suppressed the shuttle effect and sulfur deposition on the lithium anode, improving the uniformity of Li_2S deposition. Huang et al.[118] utilized rice husks as a raw material to prepare 3D porous carbon (ZRC) via zinc-assisted pyrolysis and applied it as a binder-free sulfur cathode, as shown in **Figure 9d**. The 3D conductive network enhanced electron transport efficiency and effectively buffered sulfur volume

Accepted manuscript
This manuscript will be edited, formatted and proofread. The file will be replaced with version of Record.

expansion. With sulfur loadings of 3.9, 8.5, and 10.3 mg cm^{-2}, the S/ZRC cathode delivered areal capacities of 4.1, 8.4, and 9.1 mAh cm^{-2} after 60 cycles at 0.2 C.

In summary, carbon-based catalytic systems can realize physical confinement, chemisorption, and catalysis through heteroatom doping, defect construction, or non-metallic single-atom loading. Different modification routes possess distinct merits and inherent limitations. N/O or N/P heteroatom co-doped carbons boost redox kinetics and ion transport yet suffer from insufficient active sites. Iodine single-atom decorated carbon effectively suppresses the shuttle effect, while large-scale production remains difficult. Biomass-derived porous carbon such as rice husk-based ZRC is low-cost and buffers sulfur volume expansion, albeit with poor controllability of pore structure. These strategies collectively overcome the intrinsic limitation of low catalytic activity of pure carbon materials by constructing high-density active sites to accelerate polysulfide conversion. Current challenges lie in the precise adjustment of active site density and catalytic selectivity. Future research should focus on structural design and active site engineering to further optimize catalytic efficiency and cycling stability, while balancing the trade-off between active-site density, electrical conductivity and mass transfer efficiency under practical high-sulfur-loading conditions.

Accepted manuscript
This manuscript will be edited, formatted, and proofread. The file will be replaced with Version of Record.

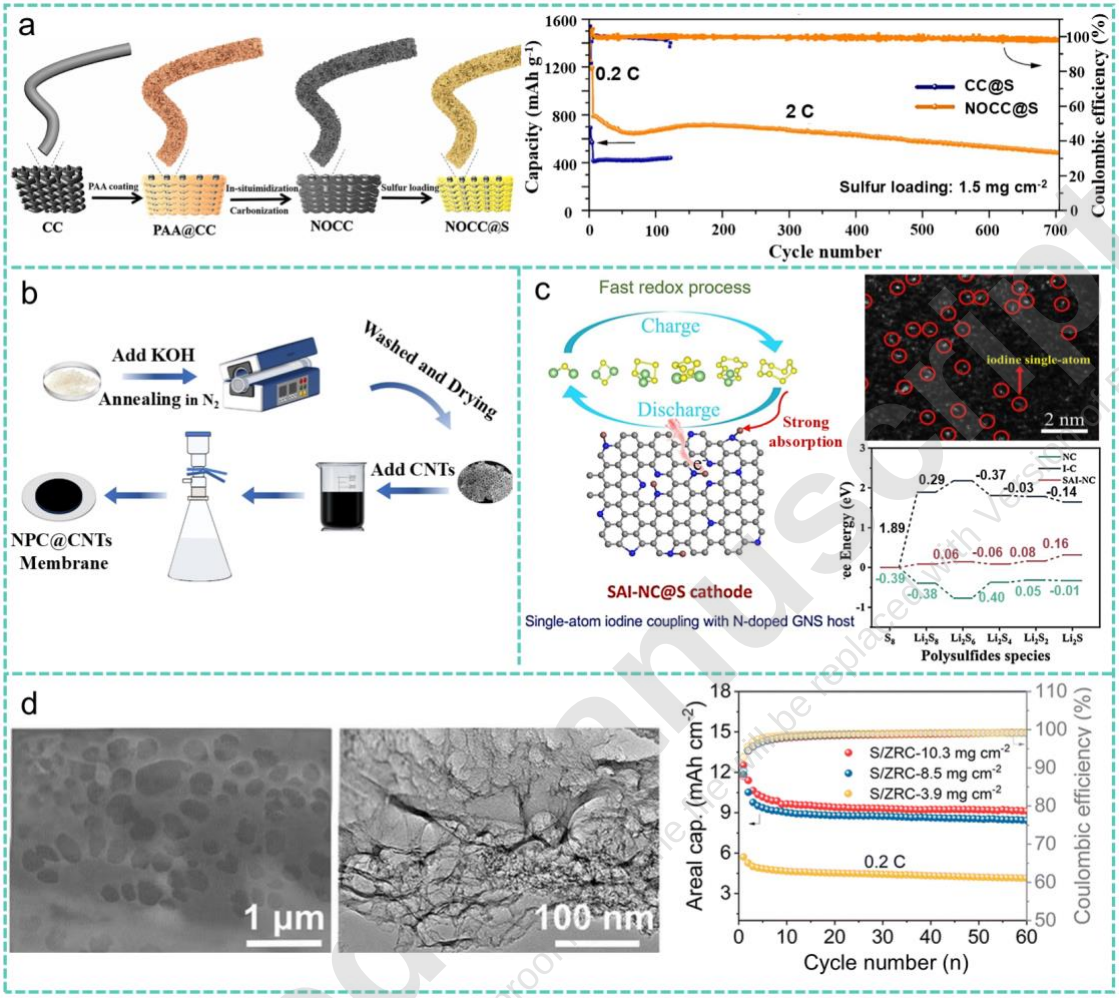


Figure 9. (a) Schematic depiction of NOCC@S composite synthesis, and long-term electrochemical stability of the electrode tested at 2 C (sulfur loading: 1.5 mg cm^{-2}). Reproduced with permission. [115] Copyright 2025, Elsevier. (b) Schematic illustration of NPC@CNTs synthesis. Reproduced with permission.[116] Copyright 2025, Elsevier. (c) Schematic diagram of SAI-NC@S adsorption mechanism, AC HAADF-STEM image of iodine single atoms, and DFT calculation results. Reproduced with permission.[117] Copyright 2025, Elsevier. (d) SEM and TEM images of ZRC and areal capacity cycling performance of S/ZRC electrode tested at 0.2 C with sulfur loadings of 3.9, 8.5, and 10.3 mg cm^{-2}. Reproduced with permission.[118] Copyright 2025, Royal Society of Chemistry.

Accepted manuscript
This manuscript will be edited, formatted and proofread before it is published in its final version. Please note that during the production process errors may be discovered which could affect the content, and all legal disclaimers that apply to the journal pertain.
Version of Record.

4.2 MOF-based Catalytic Systems

MOFs are characterized by regular porous structures, a high specific surface area, and abundant metal/ligand active sites. They can realize efficient adsorption and catalytic conversion of polysulfides through metal-sulfur coordination and polar interactions, while also providing ideal spaces for uniform sulfur dispersion. However, pristine MOFs often suffer from poor electrical conductivity. To address this issue, high-temperature pyrolysis is commonly used to prepare MOF-derived carbon-based composites. This process retains the porous topology and transforms metal species into active phases such as nanoparticles, nitrides, or phosphides, which substantially enhances conductivity and catalytic activity.[119]

For example, Meng et al.[120] designed a 3D Zr-MTAC MOF by combining azo-functionalized ligands with zirconium-oxo clusters, as shown in **Figure 10a**. The synergy between azo groups and zirconium-oxo clusters enabled efficient catalytic conversion of polysulfides. The S@Zr-MTAC cathode maintained a stable specific capacity of approximately 700 mAh g^{-1} after 1000 cycles at 1 C with a sulfur loading of 1.5 mg cm^{-2}. Under an ultra-high sulfur loading of 6.5 mg cm^{-2}, the battery still delivered a remarkable initial areal capacity of 5.8 mAh cm^{-2} and retained 4.6 mAh cm^{-2} after 120 cycles. Liu et al.[121] constructed a MOF-based sulfur-containing polymer composite (MOF808-D@PS), as shown in **Figure 10b**. The N-rich ligands significantly enhanced lithium-ion transport, achieving a diffusion coefficient 10^3 times higher than that of the unmodified polymer. The cathode retained a reversible capacity of 693 mAh g^{-1} after 500 cycles at 1 C with an estimated sulfur loading of ~1.3 mg cm^{-2}. Wu et al.[122] vertically grew Ni-HTP MOF arrays on carbon nanotubes, as shown in **Figure 10c**. The unique morphology and electronic structure significantly enhanced polysulfide adsorption, catalytic conversion and Li_2S deposition/decomposition kinetics. The electrode exhibited an ultralow capacity decay rate of only 0.042% per cycle over nearly 900 cycles at 1 C with sulfur loading approximately in the

Accepted manuscript
This manuscript will be edited, formatted and proofread. The file will be replaced with Version of Record.

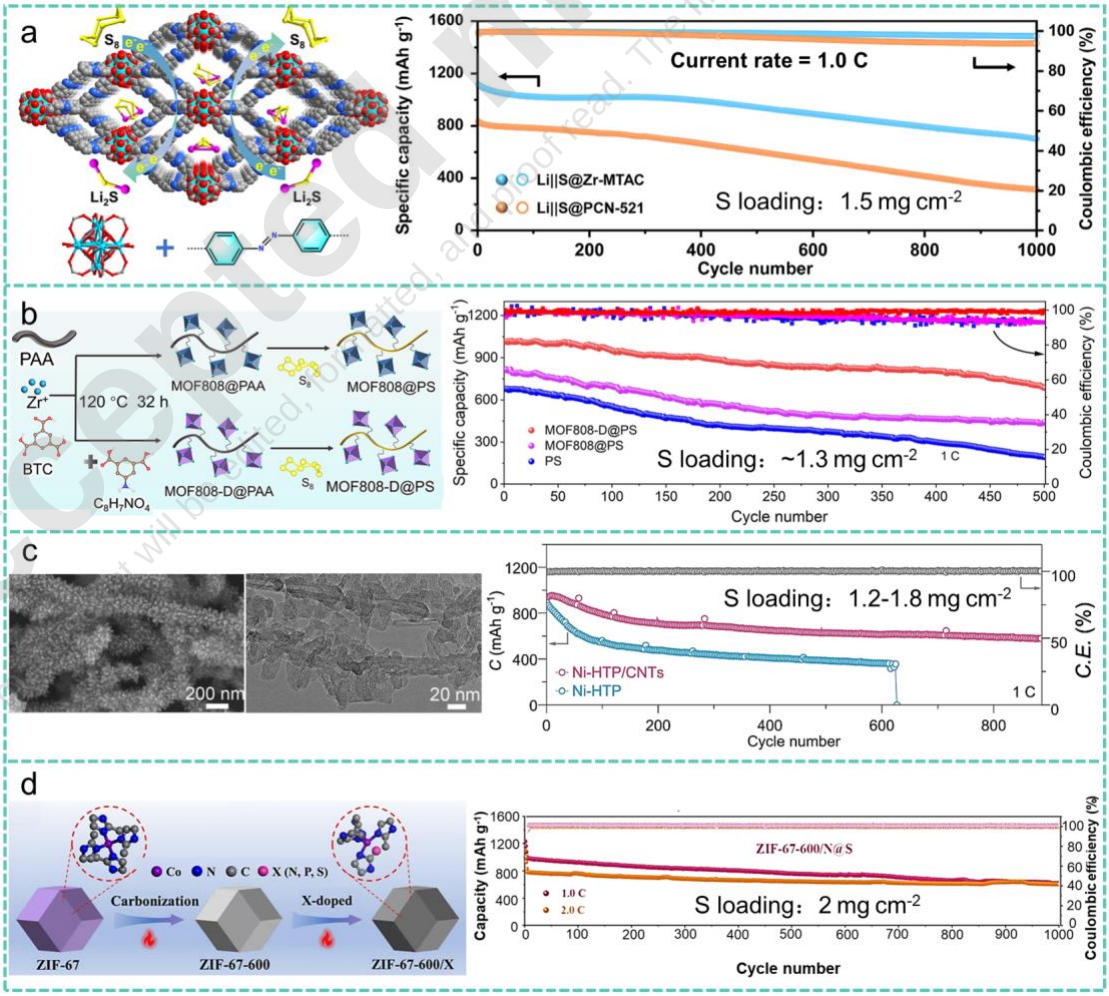
range of 1.2-1.8 mg cm^{-2}. He et al.[123] used ZIF-67 as a precursor to prepare a series of heteroatom-doped MOF-derived carbon materials, as shown in **Figure 10d**. Among them, the N-doped sample ZIF-67-600/N exhibited optimal catalytic activity and reversibility, maintaining an ultralow decay rate of 0.023% per cycle over more than 1000 cycles at 2.0 C with a sulfur loading of 2 mg cm^{-2}.

Current research progress indicates that MOF-based catalytic systems can deliver porous loading, adsorption anchoring and catalytic conversion through either functionalization of the pristine framework or pyrolytic derivatization. Such combined functional characteristics improve the overall electrochemical performance of the materials. Different modification routes possess distinct merits and inherent limitations. Azo-functionalized Zr-MOF enables efficient polysulfide catalysis and achieves ultrahigh sulfur loading, while such crystalline framework materials generally face challenges in long-cycle structural stability. N-rich ligand modified MOF-polymer composites greatly enhance Li^+ transport, yet their performance advantages are only manifested under low-to-medium sulfur loading and tend to degrade under high-sulfur-loading conditions. Vertically grown Ni-HTP MOF arrays on carbon substrates accelerate polysulfide adsorption and conversion, but such ordered array structures require cumbersome fabrication procedures. MOF-derived heteroatom-doped carbon exhibits ultra-low capacity decay, whereas high-temperature pyrolysis disrupts the fine pore structure of the original MOF framework.

Pristine MOFs utilize metal/ligand active sites to strengthen the interactions with polysulfides, while MOF-derived carbon materials further optimize reaction kinetics by forming metallic active phases and improving electrical conductivity. Notably, ligand functionalization and morphology regulation are recognized as key strategies for enhancing the catalytic performance of MOF-based systems. It is worth emphasizing that MOF-based catalytic systems may face structural collapse during long-term cycling, which is one of the main causes

Accepted manuscript
This manuscript will be edited, formatted and proofread. The file will be replaced with version of Record.

of catalyst deactivation. Meanwhile, the leaching of metal ions from MOFs may also lead to crosstalk between the positive and negative electrodes. Fortunately, strategies such as carbon coating and defect anchoring can effectively alleviate the aforementioned issues, thereby improving the long-term stability of the catalytic system. Despite these advances, current challenges still include the insufficient electrical conductivity of pristine MOFs and the difficulty in controlling the dispersion of active phases during the pyrolytic derivation process. Therefore, future research should focus on the precise structural design of MOFs and the optimization of derivation processes, aiming to realize rational matching among different components and further improve the catalytic stability and practical application potential of MOF-based catalytic systems, while reconciling the trade-off between structural robustness, active-site exposure and electron transport for long-cycle operation.



Accepted manuscript
This article will be published, after proof read. The file will be replaced with Version of Record.

Figure 10. (a) The synergistic effect of azo groups and Zr-oxo clusters on the electrochemical conversion of LiPSs, as well as the electrochemical stability of the S@Zr-MTAC electrode tested at 1 C (sulfur loading: 1.5 mg cm^{-2}). Reproduced with permission.[120] Copyright 2025, American Chemical Society. (b) Schematic synthesis process of MOF-808@PS and MOF-808-D@PS composites, as well as the electrochemical stability of the MOF-808-D@PS electrode tested at 1 C (sulfur loading: ~1.3 mg cm^{-2}). Reproduced with permission.[121] Copyright 2025, American Chemical Society. (c) SEM and TEM images of Ni-HTP/CNTs, as well as the electrochemical stability of the Ni-HTP/CNTs@S electrode tested at 1 C (sulfur loading: 1.2-1.8 mg cm^{-2}). Reproduced with permission.[122] Copyright 2026, Elsevier. (d) Schematic diagram for the preparation of ZIF-67–600/X composites and long-term cycling stability of ZIF-67–600/N@S electrode at 1 C and 2 C (sulfur loading: 2 mg cm^{-2}). Reproduced with permission.[123] Copyright 2024, Elsevier.

4.3 Metal-Based Catalytic Systems

Metal-based catalytic systems have inherent advantages such as high electrical conductivity, strong catalytic activity and significant chemical interactions with polysulfides, making them the most widely applied and effective catalytic type for Li-S battery modification.[124] Based on composition and structure, they can be further classified into single-metal catalytic systems, metal compound catalytic systems and multi-metal composite catalytic systems (**Table 2**).

Table 2. Summary of Metal-Based Catalytic Systems for Sulfur Cathodes in Li-S batteries

Cathode	Metal components	Sulfur content (wt%)/ Sulfur loading (mg cm^{-2})	Initial discharge capacity (mAh g^{-1})/C-rate	Long-term cycling (mAh g^{-1})/ cycles/C-rate	Electrolyte type	Refs.
Fe–NCNC/S	Fe	74/1.1~1.5	1176/0.1 C	539/400/1 C	Ether-based liquid	[125]
Co(Zn)@N-C/S	Co	-/2-6	1463.9/0.1 C	814/500/1 C	Ether-based liquid	[126]
NCF@CNTs/V_{900}-S	VN	-/2-10	1088.3/0.2 C	409.8/800/2 C	Ether-based liquid	[127]
S/Se-CoP@NC	CoP	75/1.25	1435.4/0.2 C	779.6/500/0.5 C	Ether-based liquid	[128]

Accepted manuscript
This manuscript will be edited, formatted, and proof read. There will be replaced with Version of Record.

PCNF/T@CoS_2/S	CoS_2	70/1.5~2	1013.8/0.5 C	860.7/310/0.5 C	Ether-based liquid	[129]
Li_2S/C/SnS_2(5%)	SnS_2	60/1	712/0.1 C	391/100/0.1 C	Ether-based liquid	[130]
KB-KOH-MoO_2@S	MoO_2	56.3/-	1218.85/0.1 C	458.76/500/2 C	Ether-based liquid	[131]
CZn(1)@S	ZnO	70/2	1260/0.05 C	1100/200/0.3 C	Ether-based liquid	[132]
S/$Co_{SA}Nb_{AC}$/NC	Co_{SA}/Nb_{AC}	71.9/1.5	1200.2/0.2 C	641.6/800/1 C	Ether-based liquid	[133]
S/VN/C@TCF	TiO_2/VN	-/1~1.5	1417.9/0.1 C	661.2/500/1 C	Ether-based liquid	[134]
VS_2/MoS_2@S	VS_2/MoS_2	40/1.7	1353/0.1 C	721/500/0.2 C	Ether-based liquid	[135]
$CoWO_4$/WO_2@S	$CoWO_4$/WO_2	20/1	1262/0.1 C	646/1000/1 C	Ether-based liquid	[136]
$Ti_3C_2T_x$-TiO_2/ZnS@S	$Ti_3C_2T_x$-TiO_2/ZnS	70/-	1259.8/0.1 C	561.4/500/0.5 C	Ether-based liquid	[137]
NiCoP@CC	NiCoP	75/1	1490.5/0.2 C	420/900/1 C	Ether-based liquid	[138]
MoO_2-MoS_2-CNT	MoO_2-MoS_2	80/1.5~2	1250/0.1 C	765.4/400/1 C	Ether-based liquid	[139]
TiO_2@V_2O_5@CdS	TiO_2@V_2O_5@Cd	-/1.5	1013/1 C	472.7/1000/1 C	Ether-based liquid	[140]
PCFCN-HEA/S	HEA	-	1221.6/0.2 C	645.4/1500/2 C	Ether-based liquid	[141]
S/HEA@HC/HCNB	HEA	12.55/~1	1348.9/0.1 C	1034.7/100/0.1 C	Ether-based liquid	[142]
GS-3/S/KB	HES	70/1.2~1.5	1567/0.1 C	～550/1500/0.5 C	Ether-based liquid	[143]

4.3.1 Single-Metal-Based Catalytic Systems

Single-metal-based catalytic systems utilize metal elements in their elemental form or as single atoms as the core active sites, which are typically supported on carbon-based substrates to achieve high dispersion and high conductivity. These metal sites can substantially reduce the conversion energy barriers of polysulfides through efficient electron transfer, significantly accelerating reaction kinetics. Among these, single-atom catalysts offer maximized atom utilization and intrinsically high catalytic activity, while metal nanoparticles have the advantages of structural stability.[144]

For example, Zhang et al.[145] constructed a carbon-vacancy-regulated iron single-atom catalyst (Fe-SAs/N-Cv), as shown in **Figure 11a**. The synergy between carbon vacancies and Fe-N_4 sites enhanced adsorption and catalysis, and both DFT calculations and experiments confirmed its excellent bifunctional properties. The S@Fe-SAs/N-Cv cathode retained 850 mAh g^{-1} after 600 cycles at 1 C with sulfur loading approximately in the range of 1.0-1.2 mg cm^{-2}. Under a high sulfur loading of 7.3 mg cm^{-2} at 0.1 C, it delivered an initial areal capacity of 7.13 mAh cm^{-2} and retained 6.56 mAh cm^{-2} after 100 cycles. Guo et al.[146] prepared cobalt single atoms supported on N-doped hollow carbon spheres

Accepted manuscript
This manuscript will be edited, formatted, and proofread. There will be replaced with Version of Record.

(NHCS@CoSAs), as shown in **Figure 11b**. The Co-N_4 active sites enabled both strong polysulfide anchoring and bidirectional catalytic conversion, resulting in an ultralow capacity decay rate of only 0.026% per cycle over more than 2000 cycles at 2 C with a sulfur loading of 1.78 mg cm^{-2}. At 0.1 C, it delivered a reversible areal capacity of 4.74 mAh cm^{-2} after 50 cycles under a high sulfur loading of 5.26 mg cm^{-2}. Su et al.[147] fabricated Cu-based N-doped carbon nanofibers (Cu/NC-NF), as shown in **Figure 11c**. The uniform 1D structure facilitated rapid electron/ion transport and structural stability. The Cu/NC-NF/S cathode maintained a stable capacity of 376.6 mAh g^{-1} after 400 cycles at 2 C with a sulfur loading of 2.55 mg cm^{-2}. Lu et al.[148] loaded Cu nanoparticles in-situ onto Ketjen black, as shown in **Figure 11d**. Cu exhibited strong adsorption towards polysulfides and significantly reduced the sulfur conversion energy barrier, kinetically suppressing the shuttle effect.

Single-metal catalytic systems can efficiently integrate polysulfide adsorption and catalytic conversion via rational matching of metal species and carbon-based supports. Such combined functional characteristics improve redox reaction behavior and electrochemical performance. Different modification routes possess distinct merits and inherent limitations. Single-atom catalysts deliver outstanding long-term cycling stability owing to maximized atom utilization and high intrinsic catalytic activity, yet single sites are prone to aggregation under high metal loading. Metal nanoparticles feature robust structural stability and favorable polysulfide adsorption capability, but they suffer from low atom utilization and relatively moderate catalytic activity. Carbon vacancy engineering and support architecture optimization represent key strategies to boost catalytic activity. Current challenges include preserving the high dispersion of single-atom sites and mitigating the agglomeration of metal nanoparticles. Future research should focus on the precise construction of active sites and the strengthening of support-metal interactions to further optimize reaction kinetics and cycling stability.

Accepted manuscript
This manuscript will be edited, formatted and proofread. The file will be replaced with Version of Record.

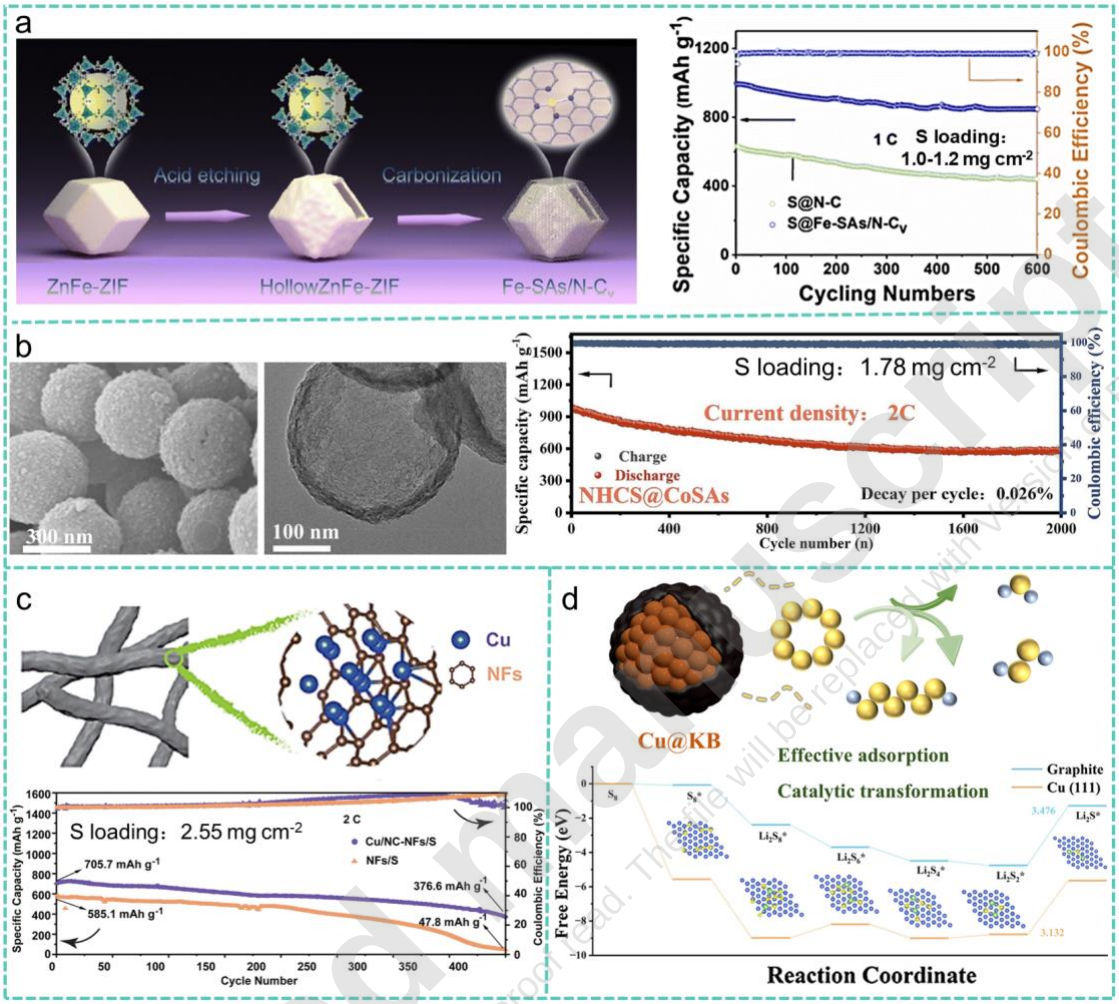


Figure 11. (a) Schematic diagram illustrating the synthesis of Fe-SAs/N-C_v, DFT calculation results, and superior electrochemical stability of the S@ Fe-SAs/N-C_v electrode tested at 1 C (sulfur loading: 1-1.2 mg cm^{-2}). Reproduced with permission.[145] Copyright 2025, Royal Society of Chemistry.(b) SEM and TEM images of NHCS@CoSAs and the long-term cycling stability of the NHCS@CoSAs/S electrode tested at 2 C (sulfur loading: 1.78 mg cm^{-2}). Reproduced with permission.[146] Copyright 2025, Elsevier.(c) Schematic illustration of the designed Cu/NC-NFs and the superior electrochemical stability of the Cu/NC-NFs/S electrode tested at 2 C (sulfur loading: 2.55 mg cm^{-2}). Reproduced with permission.[147] Copyright 2025, Royal Society of Chemistry. (d) Schematic diagram of DFT theoretical calculations and catalytic conversion mechanism for Cu@KB. Reproduced with permission. [148] Copyright 2025, Elsevier.

Accepted manuscript
This manuscript will be edited, formatted, and proofread. The file will be replaced with Version of Record.

4.3.2 Metal Compound Catalytic Systems

Metal compounds (including oxides, sulfides, nitrides, phosphides, and selenides) possess strong polarity and abundant coordination environments. These characteristics enable them to effectively anchor polysulfides through chemical bonding interactions and provide excellent electrocatalytic activity. When composited with carbon materials, These systems achieve the matched triple function of adsorption-confinement-catalysis while maintaining high conductivity, which is a crucial approach for enhancing long-term cycling stability.[149-151]

For instance, Jiang et al.[152] utilized willow branch biomass as a carbon source to prepare Fe_3O_4-loaded hierarchical porous carbon (WDC/Fe), as shown in **Figure 12a**. The Fe_3O_4, with its unfilled Fe 3d orbitals, provides efficient catalytic sites that accelerate redox kinetics. The S/WDC/Fe-7 cathode achieves an areal capacity of 6.04 mAh cm^{-2} in pouch-cell configuration under a high sulfur loading of 9.16 mg cm^{-2} with an E/S ratio of 9 μL mg^{-2}, revealing its promising prospect for practical applications in Li-S batteries. Yao et al.[153] fabricated N-doped hollow carbon spheres embedded with cobalt sulfide nanoparticles (CoS/HNC) , as shown in **Figure 12b**. The hollow structure buffers volume expansion, while polar CoS efficiently captured and catalytically converted polysulfides. Lan et al.[154] prepared TiN nanorod-decorated carbon nanofibers (CNFs-TiN NDs) via electrospinning and hydrothermal methods, as shown in **Figure 12c**. The 3D network accelerated mass transport, while TiN simultaneously achieved strong polysulfide adsorption, catalytic conversion and improved conductivity, significantly suppressing the shuttle effect. At a sulfur loading of 6.4 mg cm^{-2} with an E/S ratio < 10 μL mg^{-1}, the cathode delivered an initial areal capacity of 5.1 mAh cm^{-2} at 0.1 C. Luo et al.[155] designed a dual-carbon structure host (CoSe-CNT@NC) featuring 2D carbon nanosheets interpenetrated with carbon nanotubes and embedded with CoSe nanocatalysts, as shown in **Figure 12d**. This structure achieves synergy between highly

Accepted manuscript
This manuscript will be edited, formatted and proofread. The file will be replaced with Version of Record.

dispersed catalysis and efficient mass transfer, exhibiting excellent rate capability.

Current research demonstrates that metal compound catalytic systems can realize adsorption, confinement, and catalysis functions through compositing polar components. Such combined functional characteristics enrich the electrochemical functions of the materials. Different modification routes possess distinct merits and inherent limitations. Metal oxides (Fe_3O_4) utilize unique unfilled metal 3d orbitals to offer efficient catalytic sites for redox reactions, yet metal oxides generally exhibit moderate intrinsic electrical conductivity. Metal sulfides (CoS) combine polar polysulfide anchoring capability with volume-buffering hollow architecture, but their redox catalytic activity is relatively moderate compared with nitrides. Metal nitrides (TiN) integrate polysulfide adsorption, catalysis and good intrinsic conductivity, while their fabrication of continuous 3D fibrous networks requires elaborate synthesis. Metal selenides (CoSe) embedded in interpenetrating carbon frameworks enable rapid mass transport and favorable rate performance, yet the precise construction of such dual-carbon nanostructures demands sophisticated synthetic strategies.

Different types of compounds provide efficient catalytic sites by virtue of their unique electronic structures, while carbon-based supports ensure electrical conductivity and structural stability. Structural designs such as hollow architectures, 3D networks, and dual-carbon frameworks further optimize mass transfer efficiency and volume buffering capability. Current challenges include controlling the dispersion of active compound phases and ensuring long-term cycling stability. Future research should focus on interface engineering between metal compounds and carbon-based supports to strengthen interface interactions among different components, thereby enhancing catalytic efficiency and cycling durability at high rates.

Accepted manuscript
This manuscript will be edited, formatted and proofread. There will be replaced with the Version of Record.

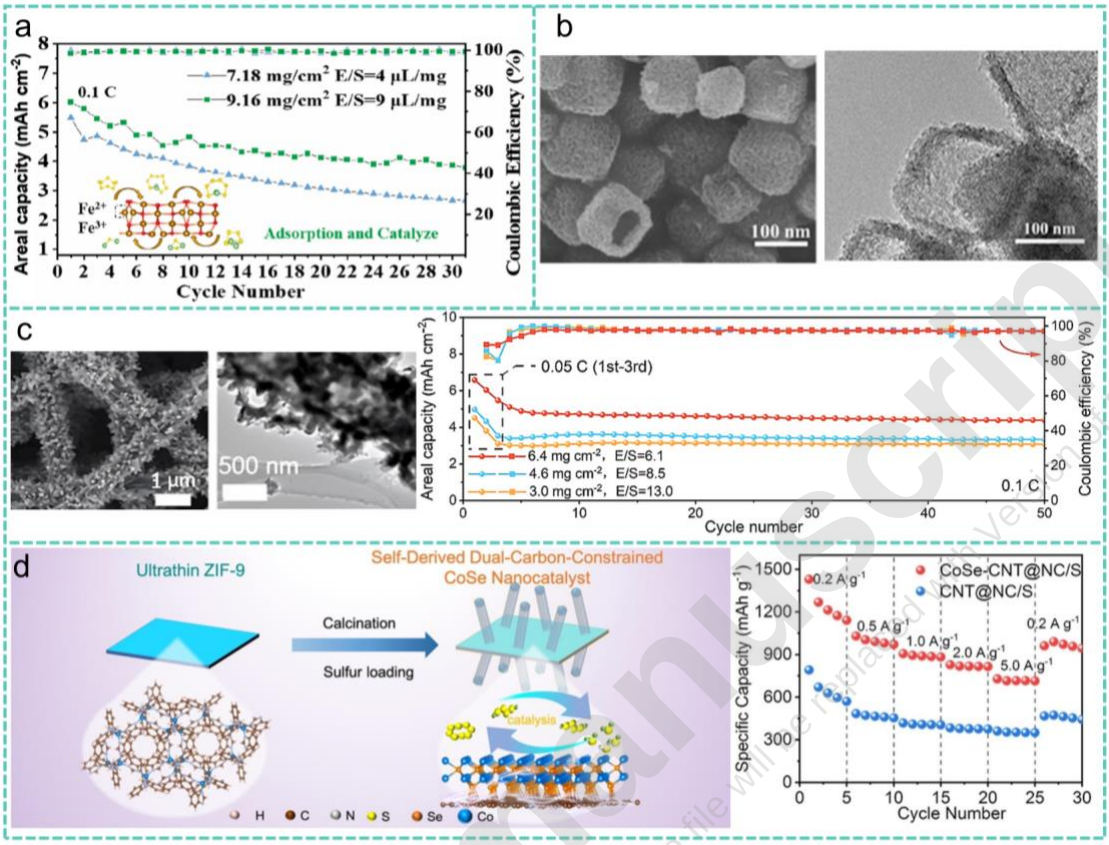


Figure 12. (a) Cycling performance of the S/WDC/Fe-7 electrode tested under high areal sulfur loadings of 9.16 and 7.18 mg cm^{-2}. Reproduced with permission.[152] Copyright 2025, Elsevier. (b) SEM and TEM images of CoS/HNC. Reproduced with permission.[153] Copyright 2024, Elsevier. (c) SEM and TEM images of CNFs-TiN NDs, as well as the electrochemical stability of its electrodes with high sulfur loadings of 3.0, 4.6, and 6.4 mg cm^{-2}. Reproduced with permission.[154] Copyright 2025, Elsevier. (d) Schematic synthetic procedure of CoSe-CNT@NC/S, as well as the rate capability of the CoSe-CNT@NC/S electrode. Reproduced with permission [155] Copyright 2026, Elsevier.

4.3.3 Multimetallic Composite Catalytic System

Multi-metal composite catalytic systems incorporate two or more metals or metal compounds as active components. Such combined structural and electronic characteristics realize functional complementarity through electron modulation, interface coupling, heterostructure construction, and multi-site configuration design. Different metal components jointly regulate polysulfide conversion

Accepted manuscript
This manuscript will be edited, formatted, and proofread. The file will be replaced with the version of Record.

pathways and accelerate redox reaction kinetics. Typically, one type of site enhances polysulfide adsorption and anchoring, while another site accelerates catalytic conversion; alternatively, different sites optimize charging and discharging kinetics separately. This addresses the limitations of single-component systems (e.g., insufficient activity, imbalanced reactions), substantially enhancing the overall battery performance.[156, 157]

For instance, Yu et al.[158] prepared a series of transition metal-bismuth dual-atom catalysts (TM-Bi DACs), as shown in **Figure 13a**. Among these, Co-Bi/CN exhibited optimal performance, maintaining 86% capacity retention after 1000 cycles at 1 C with a sulfur loading of ~1.2 mg cm^{-2}, with dual-atom synergy significantly enhancing catalytic stability. Hou et al.[159] fabricated Co/Ce dual single-atom catalysts anchored on N-doped hollow carbon spheres following adsorption-catalysis design principles to restrain the polysulfide shuttle effect, as shown in **Figure 13b**. The Co/Ce dual-site sulfur cathode exhibits an ultralow capacity decay of only 0.03% per cycle over 1000 cycles at 2 C with a sulfur loading of 2 mg cm^{-2}. Further high-loading evaluation was conducted at a sulfur loading of 4.2 mg cm^{-2} with a low E/S ratio of ~ 8 μL mg_S^{-1}, where the cathode delivered a high areal specific capacity of 3.99 mAh cm^{-2} at 0.2 C. Zhang et al.[160] designed a Co/CoSe@$MoSe_2$ hierarchical heterostructure, as shown in **Figure 13c**. The inner Co/CoSe provides high conductivity and rapid catalysis, while the outer $MoSe_2$ achieves strong capture and confinement; the heterojunction interface further accelerates charge transfer and polysulfide conversion. Our group, building upon a Co_7Fe_3 alloy catalyst, successfully constructed a Co_7Fe_3-Co heterostructure catalyst by introducing additional Co metal through a simple heat treatment process, as shown in **Figure 13d**. This catalyst was incorporated into Ketjenblack (KB) to form a sulfur-impregnated cathode material (designated as S/KB/Co_7Fe_3-Co). Li-S batteries employing S/KB/Co_7Fe_3-Co as the cathode exhibited excellent electrochemical performance, maintaining a reversible specific capacity exceeding 500 mAh g^{-1} after 1000 cycles at a current density

Accepted manuscript
This manuscript will be edited, formatted and proofread. There will be replaced with Version of Record.

of 0.6 A g^{-1}, corresponding to a capacity decay rate of 0.046% per cycle.[161]

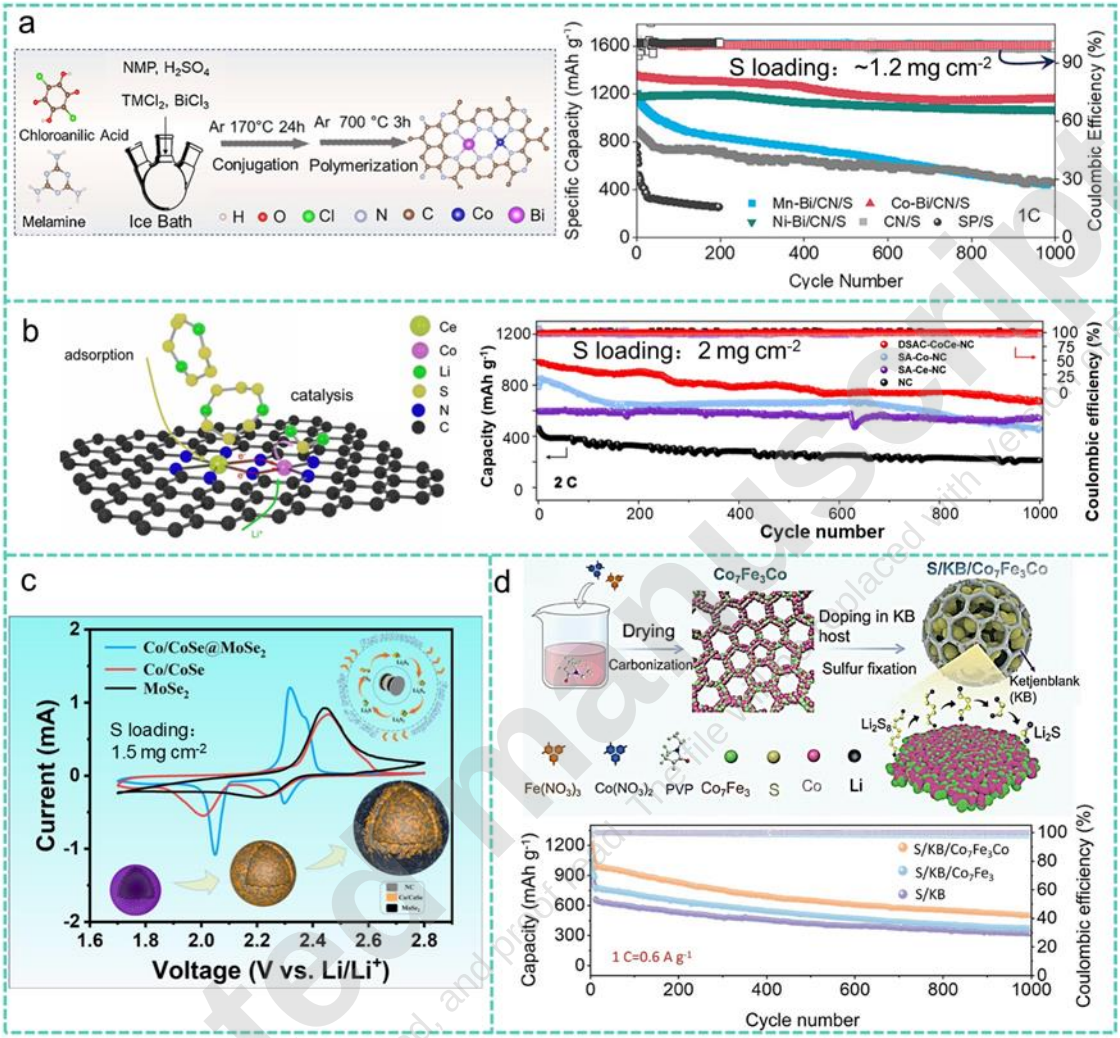


Figure 13. (a) Synthesis and physicochemical characterization of TM-Bi/CN DACs, together with the long-term cycling stability of the Co-Bi/CN/S electrode tested at 1 C (sulfur loading: ~1.2 mg cm^{-2}). Reproduced with permission.[158] Copyright 2026, Wiley-VCH. (b) Mechanism of synergistic adsorption and catalysis of Co/Ce dual single atoms and the electrochemical stability of the S@DSAC-CoCe-NC electrode tested at 2 C (sulfur loading: 2 mg cm^{-2}). Reproduced with permission.[159] Copyright 2025, American Chemical Society. (c) Schematic illustration of preparation and cyclic voltammetry curves of Co/CoSe@$MoSe_2$ at a sulfur loading of 1.5 mg cm^{-2}. Reproduced with permission.[160] Copyright 2025, Elsevier. (d) Schematic illustration of Co_7Fe_3Co preparation and the cycling stability of the S/KB/Co_7Fe_3Co electrode tested at

0.6 A g^{-1}. Reproduced with permission.[161] Copyright 2025, Wiley-VCH.

The core advantage of multi-metal composite catalytic systems lies in the precise matching of adsorption and catalysis through dual-atom configuration, heterostructure construction or functional division of dual sites. Such combined functional characteristics improve redox reaction behavior and electrochemical performance. Different modification routes possess distinct merits and inherent limitations. Bimetallic dual-atom catalysts (Co-Bi, Co/Ce) achieve inter-site functional complementarity to stabilize catalysis and mitigate capacity fading, yet the precise fabrication of dual atomic sites remains difficult. Multi-component heterostructured catalysts (Co/CoSe@$MoSe_2$, Co_7Fe_3-Co) utilize interfacial coupling to accelerate charge transfer and combine catalysis with polysulfide confinement, whereas modulation of multi-phase interfaces raises synthetic complexity. Current challenges include precise control of multi-component structural design and simplification of preparation processes. Future research should rely on theoretical calculations to guide active component screening and structural design, realizing rational matching among different metallic components to drive continuous breakthroughs in catalytic performance.

The key issues and corresponding mitigation strategies for metal-based catalytic systems (including single-metal, metal compound and multimetallic compound catalysts) in lithium-sulfur batteries are summarized as follows. In transition-metal-based catalytic systems, the leaching of metal ions (e.g., Co, Ni, Fe, Mn) from the cathode constitutes the primary origin of cathode–anode crosstalk. The dissolved metal ions can catalyze electrolyte decomposition and undermine the stability of the SEI film on the lithium anode surface. These migrated metal ions reach the lithium metal anode and impair its interfacial properties, which is commonly referred to as anode deactivation in related investigations.[162, 163] This process has been confirmed by experimental data such as XPS and ICP-MS, and can be alleviated by strategies including separator adsorption layers and electrolyte complexing agents. In addition, the insulating

Accepted manuscript
This manuscript will be edited, formatted, and proofread. The file will be replaced with Version of Record.

Li_2S products generated during the catalytic reaction tend to cover the active sites of metal-based catalysts, leading to site passivation and further catalyst deactivation. However, the core-shell structure design can effectively prevent the active sites from being covered, thereby significantly improving the stability of the catalyst.

Collectively, modulation strategies such as carbon coating, defect anchoring and high-concentration electrolytes may mitigate catalyst deactivation and cathode-anode crosstalk, improving the long-cycle stability of Li-S batteries. Despite the promising bidirectional catalytic capability of these metal-based catalysts, pairing them with structural or interfacial modifications still faces two persistent challenges: metal ion leaching and Li_2S-triggered active-site passivation. Core-shell coating can suppress ion dissolution to some extent, yet the coating layer may block the contact between catalytic sites and polysulfides, creating an inherent trade-off between catalyst stability and catalytic efficiency. Quantitative ICP-MS dissolution data for comparing the inhibitory effects of diverse core-shell architectures remain insufficient in current research. Furthermore, when composite catalytic hosts are coupled with polar polymer interlayers, strong chelation between polar polymer groups and metal ions can accelerate catalyst loss and further impair the stability of multi-component electrodes. Rational structural and compositional optimization is therefore required to balance catalytic activity, ion confinement and interfacial compatibility under practical operating conditions.

5 Interfacial Engineering to Suppress Shuttle Effect

As the core region where charge transfer, mass transport, and electrochemical reactions occur in Li-S batteries, the structural stability and kinetic properties of the interface directly determine the overall battery performance. During charge-discharge cycling, the dissolution and diffusion of polysulfides, electrode volume expansion, and parasitic reactions with the electrolyte can readily lead to interfacial structure degradation, increased impedance and deteriorated

Accepted manuscript
This manuscript will be edited, formatted and proofread. The file will be replaced with Version of Record.

interfacial compatibility, representing critical bottlenecks restricting battery performance. Interface regulation strategies aim to precisely control the interfacial microstructure and chemical composition by constructing functional interfacial layers, optimizing the electrolyte system, or modifying separators. This achieves the synergistic goals of enhancing interfacial stability, optimizing ion transport kinetics, and suppressing polysulfide shuttling. Based on regulatory targets and technical approaches, this section categorizes these strategies into three types: polymer interface regulation, electrolyte system regulation, and separator/interlayer functionalization regulation. The working mechanisms and research progress of each strategy are systematically discussed.[164-166]

5.1 Polymeric Interfacial Coating

Benefiting from their designable molecular structures (conjugated backbones, polar functional groups) and flexible composite methods, polymers have emerged as ideal functional materials for interface regulation in Li-S batteries.[167, 168] Their core advantages include: conjugated π-electron structures enabling the construction of continuous conductive networks to alleviate the inherent insulating property of sulfur; polar groups such as amino, carboxyl, and hydroxyl groups on the molecular chains anchoring polysulfides through electrostatic adsorption, hydrogen bonding, or coordination interactions; and the flexible polymer matrix buffering electrode volume expansion and maintaining interfacial structural integrity.[169, 170] Based on functional positioning and composite methods, polymer interface regulation materials can be mainly classified into two categories: conductive polymers and polar adsorptive polymers (**Table 3**). Notably, covalently bonded polymers, closely associated with the subsequent discussion on solid-state conversion cathodes, are not separately classified herein. Detailed discussion on the solid-solid reaction mechanism of covalently bonded organosulfur polymers and their typical examples is provided in Section 6: Solid State Conversion Cathodes: The SPAN and Related Polymer Family.

Accepted manuscript
This manuscript will be edited for style, and proof read. The file will be replaced with Version of Record.

Table 3. Summary of Polymer Interface Regulation for Sulfur Cathodes in Li-S batteries

Cathode	Polymer matrix	Sulfur content (wt%)/ Sulfur loading (mg cm^{-2})	Initial discharge capacity ($mAh\ g^{-1}$)/C-rate	Long-term cycling ($mAh\ g^{-1}$)/ cycles/C-rate	Electrolyte type	Refs.
BTTP@CNT/S	BPDA-T	75/1.1	1165/0.2 C	799/500/1 C	Ether-based liquid	[171]
S-TVTCSi4-CNT	S-TVTCSi4	73.6/1	1445/0.1 C	500/1000/1 C	Ether-based liquid	[172]
S-TVTCSi4-KJB2%	S-TVTCSi4	79.2/1	1202/0.1 C	652/500/0.5 C	Ether-based liquid	[173]
1,4-NDC@S@PAA	1,4-NDC@S@PAA	64.5/1.2~2.1	963/0.3 C	535/500/1 C	Ether-based liquid	[174]
S-ran-DIB/MWCNT 20	S-ran-DIB	83/3~5	1060/0.1 C	500/500/0.1 C	Ether-based liquid	[175]
S-2MIM-CNTs	S-2MIM	79/0.9~1	1524/0.1 C	~550/500/0.5 C	Ether-based liquid	[176]
IP-S	IP	-/6.87	1389.9/0.1 C	664.4/400/0.5 C	Ether-based liquid	[177]

5.1.1 Conductive Polymer

Conductive polymers utilize conjugated macromolecules such as PANI, PPy, PTh, and poly(3,4-ethylenedioxythiophene) (PEDOT) as matrices, which are composited with sulfur or sulfur-based materials to simultaneously enhanc electron conduction and suppress polysulfides at the interface. The conjugated backbone of these materials constructs continuous electron pathways throughout the electrode, while their π-π stacking structures or ion-doped sites from strong interactions with polysulfides. This optimizes interfacial charge transfer while inhibiting polysulfide dissolution and diffusion, thereby enhancing electrode structural stability.[178]

For instance, Li et al.[179] prepared PANI-coated 3D nest-like sulfur/carbon nanotube composites (SPANI@(S/CNTs)) via spray drying and sulfurization processes, as shown in **Figure 14a**. The sulfurized PANI layer, rich in polar sites, served as an efficient anchoring matrix for lithium polysulfides, inhibiting active material loss and substantially enhancing battery cycling stability. At a sulfur loading of 2.3 mg cm^{-2}, the SPANI-2@(S/CNTs)-220 cathode delivered an initial gravimetric capacity of 1220.7 mAh g^{-1}, with an areal specific capacity of 2.808 mAh cm^{-2}. After 200 cycles, it retained a reversible gravimetric capacity of 1098.9 mAh g^{-1}, corresponding to an areal specific capacity of 2.527 mAh cm^{-2}. Wang et al.[180] designed PPy-coated CeO_2/Co_3O_4 yolk-shell structured hollow

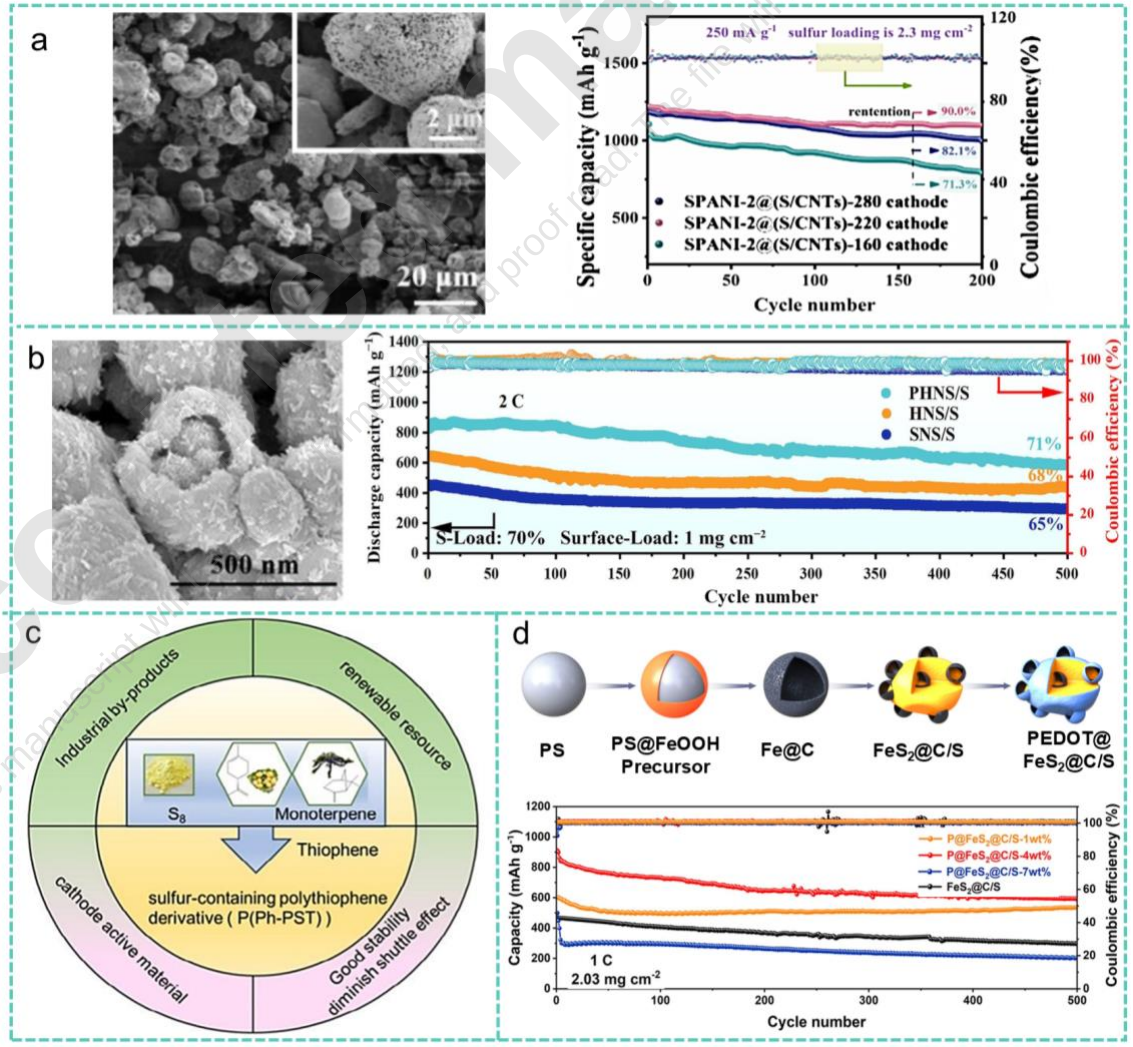
Accepted manuscript
This manuscript will be edited, formatted and proofread. The file will be replaced with Version of Record.

nanospheres (PHNS) as sulfur hosts, as shown in **Figure 14b**. The PPy coating layer not only enhanced material conductivity but also anchored polysulfides through the dual actions of physical encapsulation and chemical adsorption. The PHNS/S electrode delivered an initial discharge specific capacity of 829 mAh g^{-1} at 2 C with a sulfur loading of 1 mg cm^{-2}, and exhibited an average capacity decay rate of only 0.051% per cycle over 500 cycles. Additionally, at a high sulfur loading of 6.5 mg cm^{-2} with an E/S ratio of 9.23 μL mg_S^{-1}, a reversible areal capacity of 5.7 mAh cm^{-2} remained achievable at 0.2 C. Sun et al.[181] synthesized a novel polythiophene derivative containing sulfur segments (P(Ph-PST)) via inverse vulcanization, addition, and electrochemical polymerization using elemental sulfur, monoterpene, and thiophene as raw materials, as shown in **Figure 14c**. This polymer combined conductive properties with sulfur storage functionality, demonstrating excellent cycling stability and rate capability when used as a cathode active material. Yang et al.[182] designed a PEDOT-modified FeS_2@C hollow nanosphere sulfur host material, as shown in **Figure 14d**. FeS_2@C provided efficient catalytic activity, while the PEDOT coating exhibited both high conductivity and strong chemisorption capability; their synergy effectively suppressed the lithium polysulfide shuttle effect. With a PEDOT loading of 4 wt%, the PEDOT@FeS_2@C/S cathode maintained good cycling stability after 500 cycles at 1 C with a sulfur loading of 2.03 mg cm^{-2}. Even under a sulfur loading of 3.3 mg cm^{-2} and an E/S ratio of 9.26 μL mg^{-1}, the cathode still delivered an initial areal capacity of 2.95 mAh cm^{-2} at 0.2 C.

In summary, conductive polymers realize improved electrical conductivity, suppressed polysulfide shuttle, and stabilized electrode structure by constructing conductive networks via conjugated backbones and anchoring polysulfides through polar sites. Various modification routes exhibit distinct merits and limitations. Direct use of conductive polymers provides effective polysulfide anchoring, yet suffers from insufficient intrinsic conductivity. Compositing polymers such as PANI, PPy, and PEDOT with carbon materials or metal

Accepted manuscript
This manuscript will be edited, formatted and proofread. The file will be replaced with Version of Record.

compounds further optimizes mass transfer efficiency and catalytic activity, but still bears the risk of structural failure under high sulfur loading. Coating modification and structural design (e.g., yolk-shell structures) are key strategies for performance improvement; polymers containing sulfur segments also achieve integrated sulfur storage and conductivity. Current challenges include the need for further improvement in polymer conductivity and susceptibility to structural collapse under high sulfur loading. Future research should focus on polymer molecular design and optimization of composite processes to realize rational matching among different components and enhance high-rate and long-term cycling stability, while balancing the trade-off between polymer chain rigidity, ion transport capacity and mechanical integrity under high sulfur loading conditions.



Accepted Manuscript
This manuscript will be replaced with the final proof read version of Record.

Figure 14. (a) SEM images of SPANI@(S/CNTs) and long-term cycling stability of SPANI-2@(S/CNTs) electrodes at different vulcanization temperatures tested at 250 mA g^{-1} (sulfur loading: 2.3 mg cm^{-2}). Reproduced with permission.[179] Copyright 2024, Elsevier. (b) SEM images of PHNS and electrochemical stability of the PHNS/S electrode tested at 2 C(sulfur loading: 1 mg cm^{-2}). Reproduced with permission.[180] Copyright 2025, Elsevier. (c) Schematic illustration of P(Ph-PST) synthesis and investigation on the electrochemical stability of P(Ph-PST)-based electrode. Reproduced with permission.[181] Copyright 2025, Elsevier. (d) Schematic diagram of the synthesis route of PEDOT@FeS_2@C/S composite cathode, which delivers optimal electrochemical performance at a PEDOT loading of 4 wt% under 1 C (sulfur loading: 2.03 mg cm^{-2}). Reproduced with permission.[182] Copyright 2025, American Chemical Society.

5.1.2 Polar adsorptive polymer

Polar adsorptive polymers introduce strongly polar functional groups (e.g., amino, carboxyl, hydroxyl, cyano) into molecular chains through molecular design, achieving precise interfacial anchoring of polysulfides via electrostatic adsorption, hydrogen bonding, or coordination interactions.[183] Compared to physical barrier strategies, these materials exhibit stronger targeting for polysulfide suppression, effectively reducing active material loss and mitigating capacity decay during cycling.

For example, Zhang et al.[184] utilized waste grapefruit peel and PANI as raw materials to prepare a composite sulfur host material (PANI@GC), as shown in **Figure 15a**. PANI introduced abundant polar sites (aromatic amine groups, conjugated π-π stacking structures), forming a catalytically active interface that efficiently anchored lithium polysulfides and accelerated their conversion kinetics. The PANI@GC/S cathode exhibited boosted electrochemical performance. Souza et al.[185] prepared a microporous thiophene polymer (MTP-1) via mechanochemical oxidative polymerization, followed by impregnation

Accepted manuscript
This manuscript will be edited, formatted, and proofread. The file will be replaced with Version of Record.

with elemental sulfur to obtain a sulfur composite cathode material (MTP-1/S_8), as shown in **Figure 15b**. Zhang et al.[186] constructed a macroporous rGO foam skeleton using a bubble template, then filled submicron pores within rGO to build a hierarchical pore structure, as shown in **Figure 15c**. By electropolymerizing a poly(1-aminoanthraquinone) (PAAQ) redox mediator, a multifunctional sulfur host material (rGO-LA) was obtained. The rGO-LA@S cathode achieved a high capacity retention of 75.1% after 800 cycles at 0.5 C even with a high sulfur loading of 10.0 mg cm^{-2}. Even at an ultra-high sulfur loading of 20.1 mg cm^{-2}, it delivered a superior areal capacity of 17.5 mAh cm^{-2}. Lu et al.[187] synthesized a N-doped porous aerogel material (GA/HNBRL) using GO as the carbon source and hydrogenated nitrile butadiene rubber latex (HNBRL) as a modifier, as shown in **Figure 15d**. This host captured polysulfides through the combined effects of physical adsorption and chemical anchoring, accelerating redox kinetics; HNBRL enhanced the mechanical properties of the host, adapting to the requirements of high sulfur loading and volume expansion buffering.

In summary, polar adsorptive polymers leverage the targeted anchoring advantage of strongly polar functional groups, combined with compositing modifications involving carbon materials and elastic rubber modifiers, to realize optimized polysulfide adsorption, efficient mass transfer, and stabilized electrode structure—particularly prominent in high sulfur loading scenarios. As demonstrated by the above examples, various modification strategies exhibit distinct merits and limitations. Polar polymer alone provides strong chemical anchoring toward polysulfides, yet usually suffers from poor ion transport and insufficient mechanical robustness. Composite modification with carbon or rubber (e.g., HNBRL in GA/HNBRL host) can improve mass transfer and mechanical properties, but may introduce complicated fabrication procedures. Key strategies include tuning polar functional groups and constructing multi-functional integrated structures. Current challenges lie in the difficulty to balance

Accepted manuscript
This manuscript will be edited, formatted and proof read. There will be replaced with version of Record.

adsorption strength, ion permeability and mechanical durability for thick electrodes. Future development should focus on two main directions. first, precisely controlling the density and distribution of polar functional groups through molecular design to strengthen the selective adsorption of polysulfides; second, promoting functional integration design that combines adsorption performance with catalytic activity and mechanical support, while simplifying preparation processes and reducing costs. Furthermore, in-situ characterization and theoretical calculations are needed to elucidate the intrinsic reaction mechanism of multi-component interactions, providing precise guidance for material optimization and facilitating their practical application in high-performance Li-S batteries, while reconciling the trade-off between adsorption strength, ion permeability and mechanical durability for thick electrode implementation.

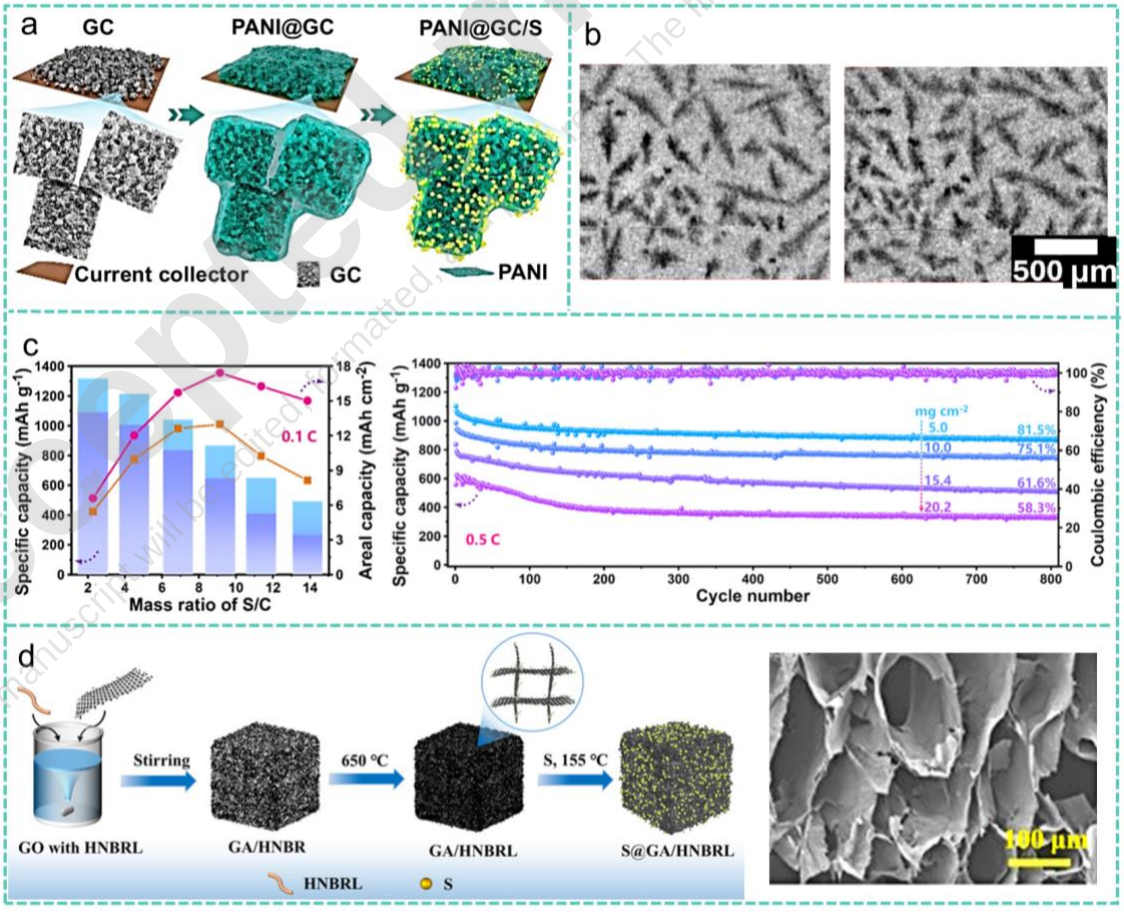


Figure 15. (a) Preparation process of PANI@GC/S. Reproduced with

permission.[184] Copyright 2025, Elsevier. (b) Microscopic morphology and molecular structure characterization of microporous thiophene-based polymer MTP-1. Reproduced with permission.[185] Copyright 2025, Elsevier. (c) Specific capacity and areal capacity at different S/C ratios, and long-term cycling stability at 0.5 C for the rGO-LA@S cathode under various sulfur loadings. Reproduced with permission.[186] Copyright 2024, Elsevier. (d) Schematic illustration of the synthesis procedure of S@GA/HNBRL and SEM images of GA/HNBRL. Reproduced with permission.[187] Copyright 2025, American Chemical Society.

5.2 Electrolyte Component Optimization

As the core medium for ion transport in Li-S batteries, electrolytes are generally classified into four categories: ether-based liquid electrolyte, carbonate-based liquid electrolyte, gel electrolyte, and polymer solid electrolyte. the solvent composition, lithium salt type, additive species, and their ratios in the electrolyte directly determine ionic conduction efficiency, polysulfide solubility, electrode/electrolyte interfacial stability, and sulfur-based redox reaction kinetics.[188, 189] Conventional electrolytes (e.g., ether-based liquid electrolyte) readily lead to excessive polysulfide dissolution, inducing the shuttle effect and lithium anode corrosion; insufficient interfacial compatibility exacerbates impedance growth and structural degradation. Electrolyte system regulation achieves the synergistic goals of polysulfide dissolution suppression, interfacial structure stabilization and reaction kinetics acceleration by precisely optimizing core components or introducing functional additives, providing critical support for enhancing Li-S battery performance (**Table 4**).[190, 191]

Table 4. Summary of Electrolyte System Regulation for Sulfur Cathodes in Li-S batteries

Cathode	Electrolyte（Functional additives）	Electrolyte (solvent)	Electrolyte (Lithium salts)	Initial discharge capacity (mAh g^{-1})/C-rate	Refs.
S/C	$LiNO_3$	CPME+DME	LiTFSI	1141.66/0.1 C	[192]
S/C	$LiNO_3$	DME+2-	LiTFSI	950/0.05 C	[193]

Accepted manuscript
This manuscript will be edited, formatted, and proofread. the PDF will be replaced with Version of Record.

		MeTHF+TFEO			
S/C	DPPs+$LiNO_3$	DOL+DME	LiTFSI	850/0.1 C	194
S	NC	DOL+DME	LiTFSI	1100/0.05 C	195
S	BNC	DOL+DME	LiTFSI	775/0.5 C	196
S@uf-MBene/CNT	Na_2SeO_3+$LiNO_3$	DOL+DME	LiTFSI	778.2/0.5 C	197
CNT-S/HA	HA	DOL+DME	LiTFSI	1493/0.2 C	198
S/CNTs	PEA+$LiNO_3$	TTE+DME+DOL	LiTFSI	~1000/0.1 C	199
S	$LiNO_3$	DME+TFTFE	LiTFSI	~850/0.15 C	200
S	$LiNO_3$	DMI+TMU	LiTFSI	1251.7/0.1 C	201
S/C	CoI_2+$LiNO_3$	DEG-DME+DOL	LiTFSI	1119.9/0.2 C	202
CNT/S	ZnI_2+$LiNO_3$	DOL+DME	LiTFSI	1250/0.1 C	203
S	$Co(bpy)_3(PF_6)_2$+$LiNO_3$	DOL+DME	LiTFSI	1228/0.2 C	204
S	DPDTe	EGDBE+TTE	LiFSI	~800/0.05 C	205
CNT-S	KPTB	DOL+DME	LiTFSI	1250/0.2 C	206
S/KB	N-Gr+$LiNO_3$	DOL+DME	LiTFSI	1376.3/0.1 C	207
S	$LiNO_3$	DOL+DME	LiTFSI	923/0.1 C(-20°C)	208
S	-	DOL+DME	F-PhSLi+LiTFSI	1618.9/0.1 C	209
S	$NiBr_2$·DME	DOL+DME	LiTFSI	919.8/0.2 C	210
S	Cu-2-T+$LiNO_3$	DOL+DME	LiTFSI	1002.8/0.2 C	211
SPAN	Py_{13}TFSI	DEE+ETFE	LiFSI	~600/0.5 C	212
SPAN	-	THP	LiFSI	579/0.5 C	213
SPAN	-	TEP+DBE	LiFSI	~700/0.2 C	214
SPAN	-	TFEP+BTFP	LiTFSI	650/0.5 C(100°C)	215
SPAN	-	PE	LiTFSI	701.2/0.1 C	216
SPAN	-	DME+TTE	LiFSI	648/0.1 A g^{-1}	217

For functionalized electrolyte additives, for instance, Gao et al.[218] proposed a coordination-mediated bifunctional chemical regulation strategy based on arylboronic acids, as shown in **Figure 16a**. With the BPBA electrolyte additive suppressing the shuttle effect and interfacial degradation, the BPBA-containing Li-S cell stably operated for 1000 cycles, delivering an ultra-low capacity decay rate of only 0.033% per cycle at 0.5 C under a sulfur loading of 2 mg cm^{-2}. Han et al.[219] introduced 6-dibutylamino-1,3,5-triazine-2,4-dithiol (DTD) as a functional electrolyte additive, achieving the dual effects of enhancing

Accepted manuscript
This manuscript will be edited, formatted and proof read. The file will be replaced with Version of Record.

polysulfide conversion and optimizing interfacial film formation, as shown in **Figure 16b**. Cho et al.[220] constructed a sustainable regulation system for directional polysulfide conversion by introducing a small amount of Lewis acidic Ca^{2+} into the electrolyte, as shown in **Figure 16c**. The Lewis acidity of Ca^{2+} drove soluble polysulfides to be directionally converted into insoluble CaS and elemental sulfur, fundamentally avoiding electrolyte thickening and significantly suppressing polysulfide shuttling and lithium anode corrosion. For electrolyte solvents, Zheng et al.[221] proposed a novel sulfur conversion mechanism mediated by cluster-type polysulfides, constructing a new electrolyte system by blending 1,2-dimethylbenzene (DTL) and DME, as shown in **Figure 16d**. In this system, the hydrophobic groups of DTL molecules encapsulate polysulfides, and in conjunction with the coordination of $TFSI^-$, drive polysulfide aggregation to form cluster-type polysulfides with virtual shell boundaries. These clusters, serving as new reaction units, successfully bridged the performance gap between traditional dissolution-dominated mechanisms and quasi-solid-state mechanisms. Jin et al.[222] proposed a redox mediation regulation strategy targeting the sluggish charge transfer kinetics of polysulfide oxidation in weakly solvating electrolytes, as shown in **Figure 16e**. By introducing specific mediators, interfacial electron transfer was accelerated. This strategy effectively enhanced the reaction kinetics of weakly solvating electrolyte systems. A 5 Ah-level pouch cell constructed based on this approach achieved a practical energy density of 470 Wh kg^{-1}, providing crucial technical support for the practical application of Li-S batteries.

Based on current research, electrolyte system regulation, through strategies such as additive functionalization, solvent blending, and ion regulation, realizes optimized polysulfide suppression, stabilized interfacial properties, and accelerated redox kinetics. Such combined functional characteristics improve the overall electrochemical performance of the battery system. In terms of lean electrolyte viability, most existing electrolyte additives are only effective under high E/S ratio conditions and exhibit significant performance degradation in lean

Accepted manuscript
This manuscript will be edited, formatted and proofread. The file will be replaced with Version of Record.

electrolyte systems with E/S ratio < 5 μL mg^{-1}. A small number of studies have achieved stable cycling under low electrolyte dosage, but they still fail to meet the stringent industrial requirements.

Future development should focus on three main directions. First, the development of multi-functional additives and solvent systems that precisely match the requirements of cathode catalysis and anode interface, balancing shuttle suppression with ionic conduction efficiency. Second, the promotion of full-system compatibility of the electrolyte with electrodes and separators, reducing interfacial impedance through rational matching among different components, and enhancing stability under high sulfur loading and high rates. Third, the deepening of the application of novel reaction mechanisms such as weak solvation and cluster mediation, combining in-situ characterization and theoretical calculations to elucidate the principles of multi-component interactions. Furthermore, attention must be paid to developing low-cost, environmentally friendly, and scalable electrolyte preparation technologies, while exploring the integration of electrolytes with novel battery configurations (e.g., solid-state batteries, anode-free systems), providing core support for the practical breakthrough of Li-S batteries.

Accepted manuscript
This manuscript will be edited, formatted and proofread. The file will be replaced with Version of Record.

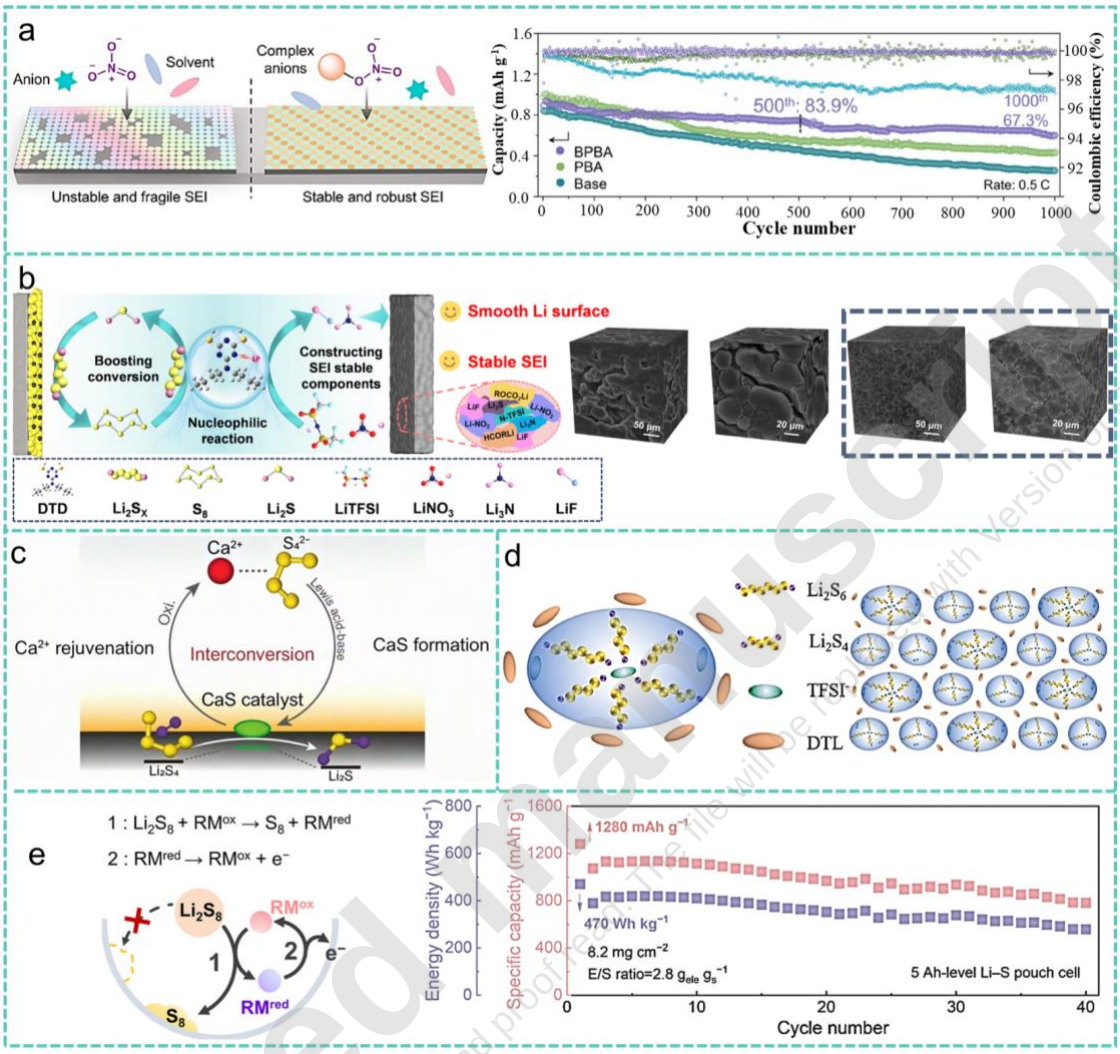


Figure 16. (a) Coordination chemistry of arylboronic acid with NO_3^-, together with enhanced cycling stability of BPBA-regulated Li-S batteries at 0.5 C (sulfur loading: 2 mg cm^{-2}). Reproduced with permission.[218] Copyright 2025, Wiley-VCH. (b) Schematic of DTD-based strategies and efficacy for mitigating Li-S battery challenges; SEM images of anodes after cycling with/without DTD at different magnifications. Reproduced with permission.[219] Copyright 2025, Royal Society of Chemistry. (c) Schematic of the features of the Lewis acidic Ca^{2+} additive in Li-S batteries. Reproduced with permission.[220] Copyright 2025, Springer Nature. (d) $TFSI^-$-mediated polysulfide clustering in CPE. Reproduced with permission.[221] Copyright 2025, Wiley-VCH. (e) Schematic of Li_2S_8 oxidation pathways in WSE-based Li-S batteries with/without charging RM, together with cycling performance of high-energy-density WSE-based Li-S

Accepted manuscript
This manuscript will be edited, formatted and proofread. The files will be replaced with version of Record.

pouch cells with charging RM tested at 0.025 C (sulfur loading: 8.2 mg cm^{-2}). Reproduced with permission.[222] Copyright 2025, Wiley-VCH.

5.3 Functionalized Separator & Interlayer Design

The separator in Li-S batteries serves the dual function of isolating the cathode and anode, ensuring lithium ion transport while preventing electron conduction. Although conventional polyolefin separators (e.g., polypropylene Celgard, polyethylene separators) possess porous structures and good ionic conductivity, their lack of adsorption or barrier capability for polysulfides fails to inhibit polysulfide shuttling between the electrodes, making them a key factor contributing to capacity decay and Coulombic efficiency reduction.[223, 224] Separator/interlayer functional regulation strategies, through modifying conventional separators or inserting functionalized interlayers (at the separator-cathode interface), construct a "smart barrier" that combines selective lithium ion transport with efficient polysulfide interception. This achieves secondary capture and catalytic conversion of polysulfides without hindering normal lithium ion transport, suppressing the shuttle effect along the transport pathway and significantly enhancing overall battery performance (**Table 5**).

Table 5. Summary of Separator/Interlayer Functional Regulation for Sulfur Cathodes in Li-S batteries

Cathode	separator substrate	Separator/Interlayer component	Initial discharge capacity ($mAh\ g^{-1}$)/C-rate	Long-term cycling ($mAh\ g^{-1}$)/cycles/C-rate	Electrolyte type	Refs.
KB/S	PE	PBC	1106/0.1 C	606/100/0.1 C	Ether-based liquid	[225]
KB/S	PE	$BaSO_4$@KB	907/0.5 C	772/200/0.5 C	Ether-based liquid	[226]
KB/S	PP	N-CNTs/Ni@WC	1478.42/0.1 C	485/500/1 C	Ether-based liquid	[227]
CNT/S	PP	FeF_3@NG	1298.3/0.2 C	654.6/500/1 C	Ether-based liquid	[228]
S	PP	HSO_3^--ETB-COF	1126/0.1 C	754.6/500/1 C	Ether-based liquid	[229]
KB/S	PP	Fe_3C/CNS	1452.2/0.2 C	640.5/500/1 C	Ether-based liquid	[230]
S/C	PP	LPC-CoS_2	1256/0.1 C	497/1000/1 C	Ether-based liquid	[231]
S/CNTs	PP	PMo_{12}/$CoSe_2$@NC/CNTs	1263.79/0.1 C	747.64/300/1 C	Ether-based liquid	[232]
S/CNTs	PP	EHNT	1324.5/0.1 C	714.8/150/0.5 C	Ether-based liquid	[233]
S	PEP	LNLPW	1510.2/0.1 C	710.9/400/0.5 C	Ether-based liquid	[234]

Accepted manuscript
This manuscript will be edited, formatted, and proofread. The final version may be published with Version of Record.

KB/S	PP	C-FeF_2	1194.4/0.1 C	534.8/400/0.5 C	Ether-based liquid	[235]
CNT/S	PP	PSN/MXene	1443/0.1 C	794/100/0.2 C	Ether-based liquid	[236]
S/C	PP	MWCNT	1100/0.05 C	800/40/0.05 C	Ether-based liquid	[237]
S	PP	TiO_2-PCF	1492/0.1 C	822/200/0.5 C	Ether-based liquid	[238]
S/C	ceramic separator	NCO/NCSO-HNWs	1260/0.2 C	695/500/1 C	Ether-based liquid	[239]
S/C	PP	Ni_2P/CoP/NC	1224.6/0.1 C	439.5/800/1 C	Ether-based liquid	[240]
g-C_3N_4/CNT/S	PP	nKL	1128.7/0.1 C	541/250/0.1 C	Ether-based liquid	[241]
CNT/S	PP	CNT/Mn-MoP	1396/0.2 C	819/200/1 C	Ether-based liquid	[242]
S	PP	TiN	1357/0.1 C	769/200/0.5 C	Ether-based liquid	[243]
CMK-3/S	PP	In_2O_3@C	1358/0.2 C	716.1/500/0.5 C	Ether-based liquid	[244]
S	PP	TTBT-COF	1033/0.1 C	530/500/1 C	Ether-based liquid	[245]
AC@S	PP	MS-HEO	~1642/0.1 C	~762/450/1 C	Ether-based liquid	[246]

For example, Du et al.[247] prepared an iron-doped titanate anchored reduced graphene oxide composite (rGO/H_2TiO_{3-x}-Fe) via an element doping optimization strategy and applied it for separator modification, as shown in **Figure 17a**. Batteries utilizing this modified separator exhibited an ultralow capacity decay rate of 0.035% per cycle over 1000 cycles at 5 C. Ma et al.[248] designed a compact heterostructure composite (MIL-88A@CdS) to construct an "adsorption-catalysis" synergistic system, as shown in **Figure 17b**. MIL-88A@CdS exhibited outstanding cycling durability, retaining a specific capacity of 975 mAh g^{-1} after 500 cycles at 1 C, and also achieved favorable areal-capacity retention over 100 cycles at 0.2 C under a cathode sulfur loading of 5.5 mg cm^{-2}. Kang et al.[249] synthesized an amino-functionalized titanium-based metal-organic framework material (NH_2-Ti-MOF) for separator modification, as shown in **Figure 17c**. The introduction of amino groups not only enhanced the chemical interaction between the material and polysulfides but also narrowed the pore size of Ti-MOF through steric hindrance effects, enabling the functionalized separator to selectively regulate the migration of lithium ions and polysulfides via a "size-sieving effect", allowing rapid lithium ion passage while blocking larger polysulfide anions. Xi et al.[250] prepared an interlayer material comprising carbon nanocages encapsulating high-entropy alloy (HEA) nanoparticles supported on viscose-based carbon fibers (HEA@NC/CF), as

Accepted manuscript
This manuscript will be edited for style and proof read. The final version may differ from this version of Record.

shown in **Figure 17d**. HEA nanoparticles accelerated sulfur species redox reactions, suppressing polysulfide shuttling; the carbon fiber network enhanced interlayer structural stability and electron transport efficiency; the HEA@NC core-shell structure provided confined reaction space for polysulfide conversion and buffered volume changes. Chhetri et al.[251] fabricated hemispherical mesoporous hollow carbon nanobowls (HM-HCNBs) via a template-assisted method and controlled carbonization process, subsequently loading bimetallic sulfides (Mo-V-S) onto their surface for separator modification, as shown in **Figure 17e**. The Mo-V-S@HM-HCNBs/Celgard interlayer achieved combined triple functions of "physical confinement-chemical adsorption-catalytic conversion," with batteries retaining 61.4% of their capacity after 1000 cycles at 3 C under a sulfur loading of 4.3 mg cm^{-2}, demonstrating excellent long-term cycling stability.

In summary, separator/interlayer functional regulation, through integrated "adsorption-catalysis-sieving" design, heterostructure construction, and multi-component configuration design, builds a "smart barrier" for efficient polysulfide interception, significantly enhancing battery long-term cycling stability. Such combined structural and functional features realize effective trapping and conversion of polysulfides. Current challenges lie in the trade-off between polysulfide interception capacity and ion permeability, as well as insufficient system compatibility under high sulfur loading and lean electrolyte conditions. Future development should focus on three main directions. First, the promotion of functional integration and precise structural design, strengthening the dynamic matching of polysulfide capture and catalytic conversion through rational matching of active components (e.g., high-entropy alloys, bimetallic sulfides) with porous hosts. Second, the optimization of interfacial compatibility and mass transfer efficiency, reducing lithium ion transport resistance while ensuring effective polysulfide interception, to meet the demands of high sulfur loading and high rates. Third, the development of low-cost, scalable preparation

Accepted manuscript
This manuscript will be edited, formatted and proofread. The file will be replaced with Version of Record.

processes to facilitate the transition of modified separators from laboratory to industry. Furthermore, combining in-situ characterization techniques to reveal interfacial reaction mechanisms, while achieving full-system compatibility among separator, electrolyte, and electrodes, is essential to further explore the inherent performance potential of the "separator-electrode-electrolyte" system, providing critical support for the practical application of Li-S batteries.

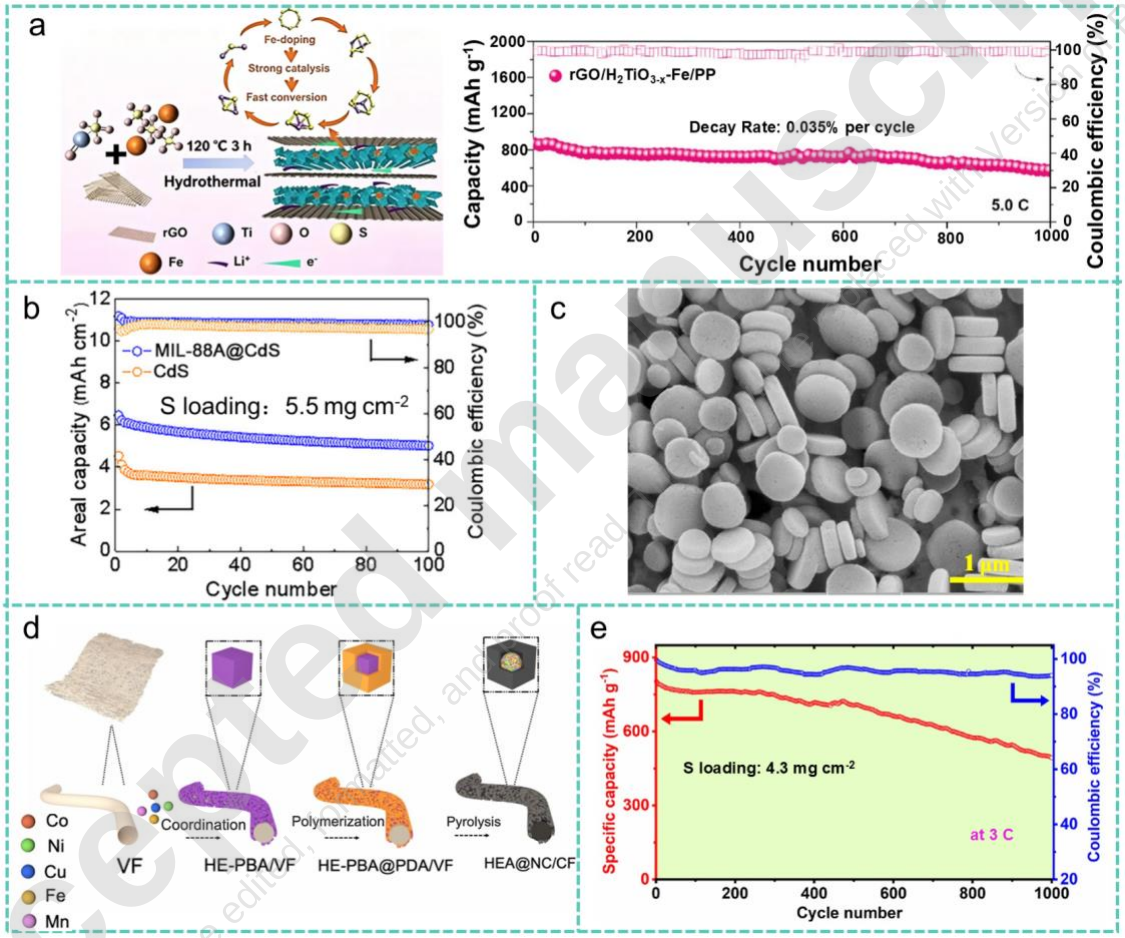


Figure 17. (a) Fabrication and working mechanism of rGO/H_2TiO_{3-x}-Fe, and long-term cycling stability of Li-S batteries with the separator tested at 5 C. Reproduced with permission.[247] Copyright 2025, Wiley-VCH. (b) Reversible cycling at 0.2C (sulfur loading: 5.5 mg cm^{-2}) of CdS and MIL-88A@CdS modified separators. Reproduced with permission.[248] Copyright 2025, Wiley-VCH. (c) SEM images of NH_2-Ti-MOF. Reproduced with permission.[249] Copyright 2025, Springer Nature. (d) Synthesis process of HEA@NC/CF. Reproduced with permission.[250] Copyright 2025, American Chemical Society. (e)

Long-term cycling stability of Li-S batteries with the Mo-V-S@HM-HCNBs/Celgard tested at 3 C (sulfur loading: 4.3 mg cm^{-2}). Reproduced with permission [251] Copyright 2026, Elsevier.

Polymer coatings, electrolyte additives and functional separators effectively block polysulfide shuttle channels, but interfacial modification introduces inevitable ion transport impedance. If thin interfacial films are used to reduce resistance, their ability to adsorb/catalyze polysulfides will be insufficient; thick functional interlayers achieve strong shuttle suppression but sacrifice rate performance. When interfacial regulation is combined with porous structural hosts, the pores of carbon frameworks are easily blocked by electrolyte decomposition products and precipitated Li_2S, jointly accelerating electrode impedance growth. At present, most interface modification work only characterizes half-cell cycling performance under excess electrolyte, and few reports systematically test electrode impedance evolution under lean E/S ratio conditions, which cannot verify their practical value for industrial high-energy-density batteries.

6 Covalent Sulfurized Polymer Cathodes with Solid–Solid Conversion (SPAN System)

Most covalently bonded organosulfur polymers undergo solid-solid reactions during charge and discharge. Sulfur species are covalently confined on polymer backbones via stable C-S bonds, thus eliminating soluble lithium polysulfides. Nevertheless, exceptions exist. Systems containing both covalently bonded sulfur and free elemental sulfur follow mixed reaction pathways involving solid-solid and liquid-solid conversions. SPAN-based cathode materials realize energy storage dominantly via solid-solid reaction routes, where no polysulfide intermediates are produced.[252] Such unique electrochemical characteristics of SPAN provide a direct reference to reveal the inherent limitations of conventional dissolution-mediated sulfur cathodes. Conventional dissolution-

Accepted manuscript
This manuscript will be edited, formatted and proof read. The PDF will be replaced with Version of Record.

mediated sulfur cathodes rely on soluble lithium polysulfides as core redox intermediates; this mechanism inevitably induces the polysulfide shuttle and loss of active materials. Strategies such as physical confinement and interface modification can only mitigate these problems rather than resolve the intrinsic mechanistic constraints.[253] In SPAN, sulfur atoms are covalently bonded to the polymer backbone, and no free long-chain polysulfides form during redox reactions, suppressing polysulfide leaching from the source. A comparison of the two reaction pathways shows that the performance bottleneck of dissolution-mediated systems arises from the soluble nature of polysulfide intermediates, and fundamental breakthroughs cannot be achieved merely via structural optimization.[254] This intrinsic characteristic enables thorough suppression of the shuttle effect without relying on conventional adsorption or catalytic modulation strategies, thus deserving independent systematic discussion. Sulfur atoms are stably immobilized by C-S covalent bonds, and the electrochemical properties can be further optimized by modulating the length of sulfur chains. The final discharge product is Li_2S embedded carbon skeleton composite, and no soluble reaction intermediates are involved in the entire redox process (**Table 6**).

Table 6. Summary of Polymer Interface Regulation for Sulfur Cathodes in Li-S batteries

Cathode	Polymer matrix	Sulfur content (wt%)/ Sulfur loading (mg cm^{-2})	Initial discharge capacity (mAh g^{-1})/C-rate	Long-term cycling (mAh g^{-1})/ cycles/C-rate	Electrolyte type	Refs.
I-SPAN	SPAN	46/8.25~8.8	700/0.05 A g^{-1}	4 mAh cm^{-2}/100/0.5 A g^{-1}	Carbonate-based liquid	255
HSPAN	SPAN	50.47/0.8~1	1796/0.2 C	1145/800/1 C	Ether-based liquid	256
SPAN-1.5%HBO	SPAN	54.2/-	881/0.1 C	577/100/1 C	Carbonate-based liquid	257
SPAN-L	SPAN	46.2/-	961.2/0.1 C	464.2/250/0.5 C	Carbonate-based liquid	258
SPAN-F3	SPAN	52.8/2.4~2.6	961/0.1 C	673/500/1 C	Carbonate-based liquid	259
$Se_{0.05}S_{0.95}$PAN-TI	SPAN	54.2/~2	958/0.1 C	~500/1000/2 C	Carbonate-based liquid	260
PAN@PPD@S	PAN@PPD@S	82.1/2	1101/0.3 C	572/500/5 C	Ether-based liquid	261
S_8@S_7Se/PAN	S_8@S_7Se/PAN	67.4/5.5	1622.7/0.2 C	1229.4/1000/1 C	Carbonate-based liquid	262
TCPS-1	TCPS	84.1/1.1~1.4	895/0.1 A g^{-1}	350/800/1 A g^{-1}	Ether-based liquid	263
PolyS-1	PolyS	59.3/0.8	943/0.1 A g^{-1}	281/500/1 A g^{-1}	Ether-based liquid	264
poly-S 60	poly-S	60/1~1.2	1066.7/0.2 C	447.5/1000/2 C	Ether-based liquid	265
poly(S_{90}-r-	poly(S_{90}-r-	95.64/0.4-0.6	1270.4/0.1 C	670.1/100/0.2 C	Ether-based liquid	266

Accepted manuscript
This manuscript will be edited, formatted and proofread. The file will be replaced with Version of Record.

$(TAEAB)_{10}$) PCS	$(TAEAB)_{10}$) PCS	86.5/~2	951.4/0.1 C	611.7/500/1 C	Ether-based liquid	[267]

For instance, Kuai et al. [268] combined DFT calculations, spectroscopic tests and AIMD simulations to explore electrolyte-cathode interfacial reactions and polysulfide dissolution of SPAN-based Li-S batteries, as shown in **Figure 18a**. They found LiFSI enables ion conduction, CEI formation and polysulfide regulation. Ethers show superior solvation to carbonates, and Li-O/S bonding determines differences in CEI growth and lithiation decomposition. Zuo et al. [269]synthesized micron PC-SPAN secondary granules via spray drying by coating nano-SPAN with crosslinked PDA/PAA/PVA, overcoming obstacles for SPAN cathodes in high-loading, lean-electrolyte high-energy Li-S cells, as shown in **Figure 18b**. Rich functional groups of the coating glue primary particles to suppress volume variation and stabilize electrodes upon cycling, while in-particle ionic channels facilitate rapid ion conduction. A prototype Li-SPAN battery with a high energy density of 530.2 Wh kg^{-1} was fabricated based on the PC-SPAN electrode with an areal capacity of 19.1 mAh cm^{-2} and a low electrolyte/SPAN ratio of 0.93 μL mg^{-1}.

As for exceptional cases, Wu et al.[270] employed hydrazine hydrate to prepare N-rich cross-linked nanoflower-like polyacrylonitrile (NH-FPAN) as a sulfur host material, as shown in **Figure 18c**. During sulfurization, the abundant N adsorption sites and cross-linked network structure of the material enabled the coexistence of elemental sulfur and covalently bonded sulfur, increasing the sulfur content from 40% to 65%. With a high sulfur loading of 24.8 mg cm^{-2}, the NH-$FSe_{0.03}S_{0.97}$PAN electrode delivered an initial areal capacity of 25.2 mAh cm^{-2} and a reversible capacity of 17.4 mAh cm^{-2} over nearly 120 stable cycles. Yi et al.[271] sulfurized polypyrrole (PPy) above 300 °C, enabling PPy to form covalent bonds with short sulfur chains, thereby preparing a sulfured polypyrrole (SPPy320V) cathode material, as shown in **Figure 18d**. By adjusting the sulfurization temperature to optimize the material's electronic structure and sulfur bonding state, SPPy320V achieved an initial specific capacity of 803 mAh

Accepted manuscript
This manuscript will be edited, formatted, and proofread. The file will be replaced with Version of Record.

g^{-1} at 2 C and an ultralow capacity decay rate of only 0.022% per cycle over 700 cycles. Zhang et al.[272] proposed a semi-immobilization strategy, preparing allyl-terminated hyperbranched polyethyleneimine-functionalized reduced graphene oxide (A-PEI-EGO) as a sulfur-rich copolymer framework, as shown in **Figure 18e**. The A-PEI-EGO-S cathode exhibited an ultralow capacity decay rate of only 0.046% per cycle over 400 cycles at 0.5 C with a sulfur loading of 1-1.5 mg cm^{-2}.

In summary, covalently bonded polymers stably anchor sulfur species via C–S bonds, fundamentally suppressing the shuttle effect and showing excellent long-term cycling stability. As demonstrated by the above examples, covalent sulfur polymer cathodes possess distinctive advantages and inherent drawbacks. Compared with traditional S_8-based cathodes, they exhibit a single ~2.1 V voltage plateau, together with favorable compatibility with ester-based electrolytes. However, their electrochemical performance is restricted by the low intrinsic conductivity of polymer matrices. Their modification strategies focus on improving conductivity, increasing sulfur content, and alleviating volume expansion, without the need for polysulfide-targeted adsorption or catalysis. Key strategies include molecular structure engineering and composite construction to enhance electron transport and accommodate volume variation. Current challenges lie in the gap between practical and theoretical energy density, and the compromised electrode mechanical integrity when fabricating thick electrodes with high sulfur loading. Future development should focus on optimizing molecular structure (e.g., copolymerization, doping) to balance capacity and kinetics, developing low-cost, scalable preparation processes, and combining in-situ characterization with theoretical calculations to precisely control C-S bonds; rational integration with catalytic components and functional hosts is also promising for advancing high-energy-density Li-S batteries' practical application, while carefully handling the trade-off between sulfur loading, polymer molecular weight and electrode mechanical integrity during

Accepted manuscript
This manuscript will be edited, formatted and proofread. There will be replaced with Version of Record.

thick electrode fabrication.

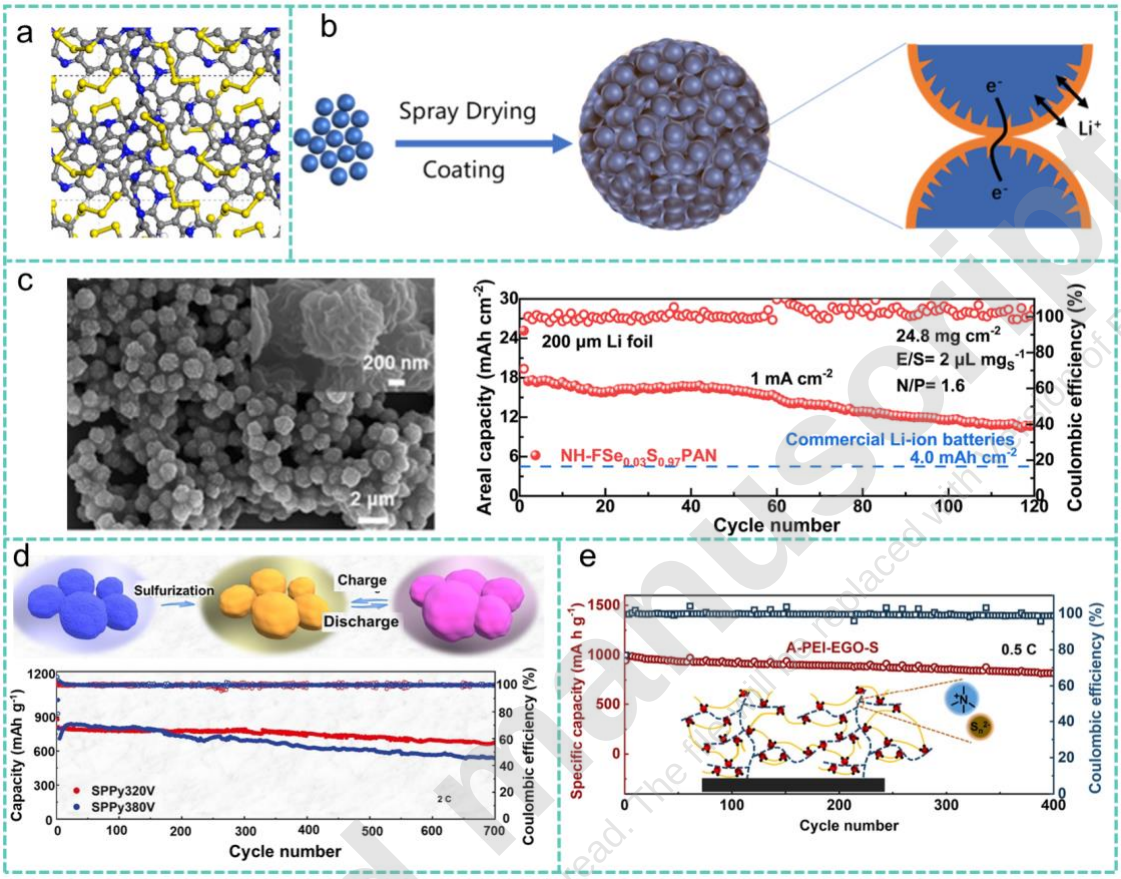


Figure 18. (a) Top view of pristine SPAN structure shown in repeated cell units, with dashed lines indicating the cell margins. Reproduced with permission. [268] Copyright 2024, American Chemical Society. (b) Illustration of the coating process through SD, the nano particles aggregated into micro-scale attribute to the interactions between the functional groups of PDA, PAA and PVA. Reproduced with permission. [269] Copyright 2024, Elsevier. (c) The synthesis route of NH-$FSe_{0.03}S_{0.97}$PAN, the schematic diagram for its practical application, and the excellent long-term cycling stability of the NH-$FSe_{0.03}S_{0.97}$PAN electrode tested at 1 mA cm^{-2} (sulfur loading: 16.1 mg cm^{-2}). Reproduced with permission.[270] Copyright 2025, Royal Society of Chemistry. (d) Illustration of the synthesis and discharge process of sulfurized polypyrrole, and the long-term cycling stability of the SPPy electrode tested at 2 C under different temperatures. Reproduced with permission.[271] Copyright 2023, Elsevier. (e) Schematic Illustration of A-PEI-EGO and A-PEI-EGO-S, as well as the Superior

Accepted manuscript
This manuscript will be edited, formatted, and proofread. The final version will replace this version of Record.

Electrochemical Stability of the A-PEI-EGO-S Electrode tested at 0.5 C (sulfur loading: 1-1.5 mg cm^{-2}). Reproduced with permission.[272] Copyright 2023, Elsevier.

7 Conclusions and Industrialization-Oriented Future Outlook

Li-S batteries possess outstanding theoretical energy density, while sulfur cathodes still face four core obstacles: sluggish charge transfer kinetics, severe volume deformation, polysulfide shuttle and low volumetric capacity. This review systematically sorts out three independent sulfur cathode modification routes: structural design, composite electrocatalysis and interfacial regulation, and separately elaborates their mechanisms, representative materials, unique strengths and inherent defects:

(1) Structural host design relies on physical confinement to improve electrode conductivity and buffer volume expansion, but high porosity leads to low tap density, which severely restricts volumetric energy density;

(2) Composite electrocatalysis accelerates polysulfide multi-step redox reactions and alleviates kinetic polarization, yet metal catalyst leaching and Li_2S active site passivation shorten cycle lifespan;

(3) Interfacial engineering inhibits polysulfide cross-membrane diffusion, but dense functional interlayers raise ion transport impedance and degrade rate capability.

A critical analysis of multi-strategy combination further reveals prominent inherent trade-offs between the three modification pathways, and existing literature cannot provide sufficient quantitative experimental evidence to confirm stable synergistic effects that surpass single optimization under industrial harsh conditions. The so-called “structure-catalysis-interface coordination” only exists in ideal material design, and multiple incompatible performance contradictions restrict its practical application. Different from previous reviews that take integrated synergistic systems as the core research direction, this work proposes differentiated cathode optimization schemes

Accepted manuscript
This manuscript will be edited, formatted and proofread. There will be replaced with Version of Record.

oriented to distinct practical indicators:

(1) Targeting high volumetric energy density: Adopt low-porosity compact structural hosts, match low-content single-atom catalytic sites, and use thin-layer lightweight interfacial modification to balance shuttle inhibition and ion conduction;

(2) Targeting high-rate discharge performance: Construct interconnected low-dimensional conductive frameworks with exposed catalytic sites, and avoid thick separator/polymer interlayers;

(3) Targeting ultra-long cycle stability: Optimize core-shell encapsulated metal catalysts, utilize medium-porosity hosts to buffer volume variation, and adopt weakly polar electrolyte additives to balance polysulfide anchoring and catalyst compatibility.

SPAN cathodes with solid-solid conversion mechanisms are discussed as a special category, which fundamentally eliminate soluble polysulfides and exhibit unique ester electrolyte compatibility, providing a distinctive technical route different from conventional elemental sulfur cathodes. Nevertheless, SPAN materials suffer from low intrinsic conductivity and limited sulfur content, requiring independent structural/catalytic optimization without polysulfide-oriented interface design.

From the perspective of industrialization, most current laboratory research only reports gravimetric specific capacity under loose test conditions (low sulfur loading, excessive electrolyte, high N/P ratio), ignoring key industrial metrics including areal capacity, E/S ratio, volumetric energy density and compaction density. Future research must standardize evaluation criteria based on pouch cell demands and supplement comparative data under lean-electrolyte and high-loading conditions. In addition, static DFT simulation cannot reflect electrode dynamic reconstruction during cycling; operando spectroscopic characterization combined with variable-temperature kinetic tests is required to accurately identify genuine electrocatalytic behaviors rather than simple adsorption

Accepted manuscript
This manuscript will be edited, formatted and proofread. There will be replaced with Version of Record.

interactions. Low-cost, scalable synthesis routes (template-free, one-step pyrolysis) should be prioritized to replace expensive MOF, high-entropy alloy and noble metal catalytic materials with complicated preparation processes.

In the future, research on sulfur cathodes should abandon the pursuit of universal three-in-one synergistic frameworks, and instead carry out targeted coupling of 1–2 modification strategies according to clear performance indicators. Combining advanced in-situ characterization and dynamic theoretical calculations to resolve the trade-off relationships between structural, catalytic and interfacial properties will be the key direction to push Li-S batteries from laboratory research to large-scale industrial applications.

Declaration of competing interest

The authors declare no conflict of interest.

Data Availability Statement

No primary research results, software or code have been included and no new data were generated or analysed as part of this review.

Acknowledgements

The authors gratefully acknowledge financial support from National Natural Science Foundation of China (52202309), Major Project for Basic and Natural Sciences Research of Jiangsu Provincial Colleges and Universities (25KJA150006), Science and Technology Cooperation Project with Hong Kong, Macao and Taiwan under the Yancheng City Science and Technology Plan (Ycgh2025008) and Postgraduate Scientific Research Innovation Program of Jiangsu Province (KYCX25_3879). All schematic figures without cited references in this manuscript are original and specially drawn for this work. These figures are not copied, adapted or redrawn from any previously published publications.

Accepted manuscript
This manuscript will be edited, formatted, and proofread. The file will be replaced with Version of Record.

Author contributions

Yang Liu performed literature retrieval and collation, conceived the framework of this review, drafted the manuscript and prepared all figures. Yaping Yang participated in the conceptual design, critical academic discussion and manuscript revision. Rong Shao, Zhidong Chen, Zhong Jin and Lin Sun contributed to critical academic discussion and manuscript polishing. Zhidong Chen and Lin Sun oversaw this work, secured financial support, administered the research project and revised the manuscript. All authors have read and approved the final version of the manuscript.

Accepted manuscript
This manuscript will be edited, formatted, and proof read. The file will be replaced with Version of Record.

8 References

1. M. Kotal, S. Jakhar, S. Roy, H.K. Sharma. *J. Energy Storage*, **47**, 103534 (2022); https://doi.org/10.1016/j.est.2021.103534
2. J. Chang, Q. Huang, Y. Gao, Z. Zheng. *Adv. Mater.*, **33**, 2004419 (2021); https://doi.org/10.1002/adma.202004419
3. A.Y. Tsivadze, T.L. Kulova, V.N. Andreev, A.M. Skundin, O.V. Korchagin, A.D. Modestov, O.V. Tripachev, K.P. Birin. *Russ. Chem. Rev.*, **95**, RCR5200 (2026); https://doi.org/10.59761/rcr5200
4. Y. Ding, Z.P. Cano, A. Yu, J. Lu, Z. Chen. *Electrochem. Energy Rev.*, **2**, 1 (2019); https://doi.org/10.1007/s41918-018-0022-z
5. G. Li, Z. Chen, J. Lu. *Chem*, **4**, 3 (2018); https://doi.org/10.1016/j.chempr.2017.12.012
6. H. Raza, S. Bai, J. Cheng, S. Majumder, H. Zhu, Q. Liu, G. Zheng, X. Li, G. Chen. *Electrochem. Energy Rev.*, **6**, 29 (2023); https://doi.org/10.1007/s41918-023-00188-4
7. J. Yu, I. Pinto-Huguet, C.Y. Zhang, Y. Zhou, Y. Xu, A. Vizintin, J.-J. Velasco-Vélez, X. Qi, X. Pan, G. Oney, A. Olgo, K. Märker, L. M. Da Silva, Y. Luo, Y. Lu, C. Huang, E. Härk, J. Fleming, P. Chenevier, A. Cabot, Y. Bai, M. Botifoll, A.P. Black, Q. An, T. Amietszajew, J. Arbiol. *ACS Energy Lett.*, **9**, 6178 (2024); https://doi.org/10.1021/acsenergylett.4c02703
8. M. Zhao, B.-Q. Li, X.-Q. Zhang, J.-Q. Huang, Q. Zhang. *ACS Cent. Sci.*, **6**, 1095 (2020); https://doi.org/10.1021/acscentsci.0c00449
9. I. Marri, Z. Edfouf, A. Caballero, A.Y. Tesio. *J. Energy Storage*, **82**, 110518 (2024); https://doi.org/10.1016/j.est.2024.110518
10. R. Chen, Y. Zhou, X. Li. *Energy Storage Mater.*, **68**, 103353 (2024); https://doi.org/10.1016/j.ensm.2024.103353
11. C. Wang, R. Liu, W. Liu, W. Zhu, X. Yang, Q. Wu, K. Xie, L. Shen, J. Wu, Y. Liu, L. He, Z. Chen, J. Chen, C. Zhao, X. Lin, L. Shi, J. Zhao, X. Feng, G. Wu, Y. Ma. *Adv. Funct. Mater.*, **34**, 2316221 (2024);

Accepted manuscript
This manuscript will be edited for style and proofread. The file will be replaced with the Version of Record.

https://doi.org/10.1002/adfm.202316221

12. X. Zuo, L. Wang, M. Zhen, T. You, D. Liu, Y. Zhang. *Angew. Chem. Int. Ed.*, **63**, e202408026 (2024); https://doi.org/10.1002/anie.202408026
13. X. Chen, C. Zhao, K. Yang, S. Sun, J. Bi, N. Zhu, Q. Cai, J. Wang, W. Yan. *Energy Environ. Mater.*, **6**, e12483 (2023); https://doi.org/10.1002/eem2.12483
14. Z. Jiang, Z. Zeng, W. Hu, Z. Han, S. Cheng, J. Xie. *Energy Storage Mater.*, **36**, 333 (2021); https://doi.org/10.1016/j.ensm.2021.01.008
15. L. Fang, W. Xu, X. Lyu, Y. Liu, B. Reinhart, H. Nguyen, T. Li. *ACS Appl. Energy Mater.*, **6**, 795 (2023); https://doi.org/10.1021/acsaem.2c03017
16. S. Drvarič Talian, M. Bešter-Rogač, R. Dominko. *Electrochim. Acta*, **252**, 147 (2017); https://doi.org/10.1016/j.electacta.2017.08.168
17. H. Chen, Z. Zhang, H. Qin, B. Zhang, D. Wang, L. Ming, X. Ou. *Adv. Funct. Mater.*, **35**, 2506355 (2025); https://doi.org/10.1002/adfm.202506355
18. Z. Su, L. Wang, Z. Wang, B. Fang, R. Mo. *J. Colloid Interface Sci.*, **704**, 139321 (2026); https://doi.org/10.1016/j.jcis.2025.139321
19. J.H. Na, S. Jang, H.J. Kim, J.K. Kim, H. Jang, I. Nam, S.-K. Park. *Adv. Fiber Mater.*, **8**, 234 (2026); https://doi.org/10.1007/s42765-025-00614-w
20. J. Liu, J. Zhang, J. Zhu, R. Zhao, Y. Zhang, Y. Ma, C. Li, H. Zhang, Y. Chen. *Nano Res.*, **16**, 12601 (2023); https://doi.org/10.1007/s12274-023-5683-1
21. J. He, A. Bhargav, A. Manthiram. *Angew. Chem. Int. Ed.*, **61**, e202116586 (2022); https://doi.org/10.1002/anie.202116586
22. W. Sun, L. Xu, Z. Song, H. Lin, Z. Jin, W. Wang, A. Wang, Y. Huang. *Adv. Funct. Mater.*, **34**, 2313112 (2024); https://doi.org/10.1002/adfm.202313112
23. C. Xu, H. Wang, X. Liu, G. Liu, Z. Zhang, C. Wu, J. Li. *J. Power Sources*, **562**, 232778 (2023); https://doi.org/10.1016/j.jpowsour.2023.232778
24. X. Yang, S. Cao, Z. He, C. Xu, H. Wang, G. Liu. *Electrochim. Acta*, **469**, 143259 (2023); https://doi.org/10.1016/j.electacta.2023.143259
25. Z. Wang, J. Shen, J. Liu, X. Xu, Z. Liu, R. Hu, L. Yang, Y. Feng, J. Liu, Z. Shi, L. Ouyang, Y. Yu, M. Zhu. *Adv. Mater.*, **31**, 1902228 (2019);

Accepted manuscript
This manuscript will be edited, formatted, and proofread. There will be replaced with Version of Record.

https://doi.org/10.1002/adma.201902228

26. R. Deng, M. Wang, H. Yu, S. Luo, J. Li, F. Chu, B. Liu, F. Wu. *Energy Environ. Mater.*, **5**, 777 (2022); https://doi.org/10.1002/eem2.12257
27. Z.W. Seh, Y. Sun, Q. Zhang, Y. Cui. *Chem. Soc. Rev.*, **45**, 5605 (2016); https://doi.org/10.1039/C5CS00410A
28. Z. Shi, M. Li, J. Sun, Z. Chen. *Adv. Energy Mater.*, **11**, 2100332 (2021); https://doi.org/10.1002/aenm.202100332
29. Y.-W. Song, L. Shen, N. Yao, S. Feng, Q. Cheng, J. Ma, X. Chen, B.-Q. Li, Q. Zhang. *Angew. Chem. Int. Ed.*, **63**, e202400343 (2024); https://doi.org/10.1002/anie.202400343
30. L. Zhou, D.L. Danilov, F. Qiao, J. Wang, H. Li, R.-A. Eichel, P.H.L. Notten. *Adv. Energy Mater.*, **12**, 2202094 (2022); https://doi.org/10.1002/aenm.202202094
31. J. Offermann, S.N. Ul Haq, K.-X. Wang, R. Adelung, S.-H. Chang, B. Babu, M. Abdollahifar. *Adv. Energy Mater.*, **15**, 2404383 (2025); https://doi.org/10.1002/aenm.202404383
32. J. Chen, Y. Zhang, J. Yang, Y. Nuli, J. Wang. *Sci. China Chem.*, **67**, 106 (2024); https://doi.org/10.1007/s11426-022-1421-7
33. T. Duivenvoorden, S. Sanderson, D.J. Searles. *Batteries Supercaps*, **7**, e202300324 (2024); https://doi.org/10.1002/batt.202300324
34. X. Yang, X. Li, K. Adair, H. Zhang, X. Sun. *Electrochem. Energy Rev.*, **1**, 239 (2018); https://doi.org/10.1007/s41918-018-0010-3
35. W. Teng, R. Wang, J. Cheng, P. Xiao, D. Wang. *Renewables*, **3**, 306 (2025); https://doi.org/10.31635/renewables.025.202500100
36. R. Zhang, N.-W. Li, X.-B. Cheng, Y.-X. Yin, Q. Zhang, Y.-G. Guo. *Adv. Sci.*, **4**, 1600445 (2017); https://doi.org/10.1002/advs.201600445
37. J.-J. Long, H. Yu, W.-B. Liu. *Rare Met.*, **43**, 1370 (2024); https://doi.org/10.1007/s12598-023-02378-x
38. X. Zuo, Y. Qiu, M. Zhen, D. Liu, Y. Zhang. *Nano-Micro Lett.*, **17**, 209 (2025);

Accepted manuscript
This manuscript will be edited, formatted and proofread. The file will be replaced with Version of Record.

https://doi.org/10.1007/s40820-025-01726-z

39. R.I. Anayah, I.J. Dillingham, V.S. Thoi. *ACS Appl. Energy Mater.*, **8**, 4815 (2025); https://doi.org/10.1021/acsaem.5c00725

40. Y. Li, R. He, H. Liu, X. Zhang. *Mater. Chem. Phys.*, **308**, 128288 (2023); https://doi.org/10.1016/j.matchemphys.2023.128288

41. Y. Wang, X. Wang, H. Ye, K. Han. *Appl. Clay Sci.*, **179**, 105172 (2019); https://doi.org/10.1016/j.clay.2019.105172

42. T. Hu, Y. Chen, H. Liu, L. Liu, C. Dai, Y. Han. *Next Energy*, **6**, 100212 (2025); https://doi.org/10.1016/j.nxener.2024.100212

43. B. Nie, C. Zhou, M. Gao, D. He, Z. Yao, Y. Liu, X. Shen, X. Wang, H. Pan. *J. Alloys Compd.*, **797**, 1205 (2019); https://doi.org/10.1016/j.jallcom.2019.04.192

44. Z. Chen, J. Long, T. Zhou, T. Han, Y. Hu, J. Liu. *J. Electroanal. Chem.*, **916**, 116371 (2022); https://doi.org/10.1016/j.jelechem.2022.116371

45. R. Nadimicherla, Y.-c. Tang, Y.-h. Lu, R.-l. Liu. *New Carbon Mater.*, **40**, 188 (2025); https://doi.org/10.1016/S1872-5805(25)60944-9

46. R. Ren, R. Du, Y. Li, J. Wang, Z. Shi, M. Li. *Energy & Fuels*, **39**, 12768 (2025); https://doi.org/10.1021/acs.energyfuels.5c01486

47. W. Bi, C. Li, D. Yang, Y.-Z. Zhang, L. Hu, Q. Gong, J. Zhang, Y. Zhang, M. Li, J. Wei, Y. Zhou, D. Zhou, T. Wu, L.-F. Chen, A. Cabot. *Energy Environ. Sci.*, **18**, 1929 (2025); https://doi.org/10.1039/D4EE04689G

48. X.-D. Zhou, X.-X. Wu, H.-J. Fu, P.-X. Lei, N. Li, H.-P. Li, H.-B. Huang. *Mater. Today Energy*, **52**, 101950 (2025); https://doi.org/10.1016/j.mtener.2025.101950

49. Z. Wang, K. Tian, T. Liang, Z. Chen, Y. Chang, L. Yang, S. Yin. *Electrochim. Acta*, **548**, 147911 (2026); https://doi.org/10.1016/j.electacta.2025.147911

50. S. Wei, H. Chen, F. Yu, X. Wu, L. Que, T. Hu, J. Wang, M. Huang, C.-Z. Lu, Y. Xie. *J. Power Sources*, **598**, 234193 (2024); https://doi.org/10.1016/j.jpowsour.2024.234193

Accepted manuscript
This manuscript will be edited, formatted and proofread. The file will be replaced with Version of Record.

51. W.-G. Lim, M. Ban, K.I. Shim, J. Park, S. Kim, S. Kim, S. Kim, C.-Y. Park, J.W. Han, J. Lee. *Chem. Eng. J.*, **495**, 153472 (2024); https://doi.org/10.1016/j.cej.2024.153472

52. Y. Huang, L.-J. Zhang, W. Wang, Z.-K. Li, X. Liu, H.-L. Yan, J.-C. Yan, W.-D. Zhang, Z.-P. Lei, S.-B. Ren, Z.-C. Wang, H.-F. Shui, L.-J. Yan. *Fuel*, **406**, 136919 (2026); https://doi.org/10.1016/j.fuel.2025.136919

53. Z. Yang, K. Chen, Q. Sun, N. Ding, G. Zhang, S. Xing. *Electrochim. Acta*, **538**, 146993 (2025); https://doi.org/10.1016/j.electacta.2025.146993

54. D. Bowman, A.T.S.C. Brandão, S. State, R. Costa, M. Enachescu, L.-B. Enache, C.M. Pereira, D. McNulty. *J. Power Sources*, **649**, 237406 (2025); https://doi.org/10.1016/j.jpowsour.2025.237406

55. G. Yuan, R. Jing, H. Wen, X. Sun, Q. Xu, H. Xue. *Mater. Today Commun.*, **47**, 113095 (2025); https://doi.org/10.1016/j.mtcomm.2025.113095

56. T. Cheng, H. Cui, J. Shi, Y. Weng, R. Yan, Y. Liu, M. Li, Q. Li, N. Yan. *Chem. Phys. Lett.*, **882**, 142478 (2026); https://doi.org/10.1016/j.cplett.2025.142478

57. R.L. de Freitas Filho, K.S. Santos, R.C. Ferreira Silva, L. Coelho de Oliveira, I.B. Gomes, F.G. Gandra, L.T. Cardoso, D.D. Justino, P.S. Pinto, A.P. de Carvalho Teixeira, J.P. Campos Trigueiro, P.F. Ribeiro Ortega, R.L. Lavall, G.G. Silva. *Microporous Mesoporous Mater.*, **387**, 113530 (2025); https://doi.org/10.1016/j.micromeso.2025.113530

58. S. Pothaya, N. Maeboonruan, J. Lohitkarn, C. Poochai, Y. Chuminjak, C. Sriprachuabwonga. *Diamond Relat. Mater.*, **159**, 112879 (2025); https://doi.org/10.1016/j.diamond.2025.112879

59. S. Chen, G. Du, Y. Cheng, D. Han, J. Deng, Y. Wang, H. Li, L. Yao, D. Wang, Q. Su, B. Xu. *Chem. Eng. J.*, **509**, 161440 (2025); https://doi.org/10.1016/j.cej.2025.161440

60. A. Dharmesh, P. Rani, A.K. Sharma. *J. Power Sources*, **634**, 236429 (2025); https://doi.org/10.1016/j.jpowsour.2025.236429

61. X. Wang, H. Chen, F. Yu, S. Wei, J. Liu, L. Que, Y. Wu, Q. Pang, C. Lu, Y. Xie.

Accepted manuscript
This manuscript will be edited, formatted and proofread. The file will be replaced with Version of Record.

Chem. Eng. J., **513**, 162707 (2025); https://doi.org/10.1016/j.cej.2025.162707

62. H. Tang, M. Hu, D. Li, J. Zhu, J. Chen, N. Liu. *J. Electroanal. Chem.*, **979**, 118923 (2025); https://doi.org/10.1016/j.jelechem.2024.118923

63. J. Wang, k. Chen, S. Liu, D. Duan, X. Zhou, J. Wang, Y. Li, S. Liu. *J. Energy Storage*, **134**, 118162 (2025); https://doi.org/10.1016/j.est.2025.118162

64. K. Chhetri, I. Pathak, D. Acharya, Y.R. Rosyara, R.M. Bhattrai, K.-H. Kong, B.-S. Kim, T. Kim, T.H. Ko, H.Y. Kim. *J. Energy Storage*, **136**, 118459 (2025); https://doi.org/10.1016/j.est.2025.118459

65. Y. Ren, X. Song, H. Wang, Y. Zeng, X. Li, R. Xue, J. Xiao. *Electrochim. Acta*, **482**, 143991 (2024); https://doi.org/10.1016/j.electacta.2024.143991

66. B. Li, Y. Yan, X. Zhang, B. Ren, Z. Meng, R. Xu, Y. Zou, Q. Deng, W. Yu, X. Wang, N. Zhao, L. Zhong, R. Yang, Y. Xu. *Adv. Powder Technol.*, **36**, 105016 (2025); https://doi.org/10.1016/j.apt.2025.105016

67. J. Guo, R. Niu, W.K. Pang, S. Zhao, X. Yan, X. Zhang, H. Li, Z. Li. *Electrochim. Acta*, **545**, 147718 (2026); https://doi.org/10.1016/j.electacta.2025.147718

68. J. Lu, M. Zhu, M. Kim, A. He, C. Wang, T.H. Kim, S.H. Lee. *J. Power Sources*, **647**, 237269 (2025); https://doi.org/10.1016/j.jpowsour.2025.237269

69. D.D. Pathak, M. Neem, G. Kumar, B. Modak, S. Neogi, B.P. Mandal. *J. Energy Storage*, **117**, 116176 (2025); https://doi.org/10.1016/j.est.2025.116176

70. J. Lu, Y. Zhang, J. Huang, H. Jiang, B. Liang, B. Wang, D. He, H. Chen. *J. Energy Storage*, **118**, 116330 (2025); https://doi.org/10.1016/j.est.2025.116330

71. J. Xie, Y. Li, J. Li, Z. Wu, Y. Huang, H. Huang, X. Liang, G. Li, P. Qing, D. Huang, H. Liu, Z. Lan, W. Zhou. *J. Alloys Compd.*, **1036**, 181797 (2025); https://doi.org/10.1016/j.jallcom.2025.181797

72. P. Lin, B. Gao, Z. Fan, M. Wang, X. Lan, H. Fu. *J. Energy Storage*, **125**, 117001 (2025); https://doi.org/10.1016/j.est.2025.117001

73. J. Yuan, W. Ding, L.R. Jaishi, K. Muthukumarappan, Z. Wang, X. Xian. *Nano Res.*, **18**, 94907828 (2025); https://doi.org/10.26599/NR.2025.94907828

74. L. He, J. Liao, M. Tang, L. Gan, Y. Huang, Q. Jiang. *"Colloids Surf., A"*, **719**,

Accepted manuscript
This manuscript will be edited, formatted and proofread. The file will be replaced with Version of Record.

137005 (2025); https://doi.org/10.1016/j.colsurfa.2025.137005

75. C. Cui, X. Xu, Q. Cui, Z. Wang, L. Wang, S. Yao, J. Wei, H. Su. *Energy & Fuels*, **39**, 15864 (2025); https://doi.org/10.1021/acs.energyfuels.5c01790

76. R. Ren, L. Huang, R. Du, Y. Li, M. Li, N. Mo. *J. Alloys Compd.*, **1050**, 185629 (2026); https://doi.org/10.1016/j.jallcom.2025.185629

77. Y. Xie, S. Liao, W. Zheng, H. Zhang, X. Wang. *Chem. Eng. J.*, **519**, 165584 (2025); https://doi.org/10.1016/j.cej.2025.165584

78. Y. Xie, F. Wu, W. Zheng, H. Zhang, X. Wang. *Sci. China Mater.*, **68**, 1100 (2025); https://doi.org/10.1007/s40843-024-3259-x

79. J. Luo, K. Guan, W. Lei, S. Zhang, Q. Jia, H. Zhang. *Journal of Materials Science & Technology*, **122**, 101 (2022); https://doi.org/10.1016/j.jmst.2021.12.048

80. X. Liu, L. Zhang, X. Ma, H. Lu, L. Li, X. Zhang, L. Wu. *Chem. Eng. J.*, **454**, 140460 (2023); https://doi.org/10.1016/j.cej.2022.140460

81. J. Xiang, Z. Guo, Z. Yi, Y. Zhang, L. Yuan, Z. Cheng, Y. Shen, Y. Huang. *J. Energy Chem.*, **49**, 161 (2020); https://doi.org/10.1016/j.jechem.2020.01.037

82. X. Yang, N. Yan, W. Zhou, H. Zhang, X. Li, H. Zhang. *J. Mater. Chem. A*, **3**, 15314 (2015); https://doi.org/10.1039/C5TA03013G

83. D. Wang, H. Yan, Y. Yang, J. Cheng, Y. Lu, Y. Luo, H. Pang. *Sci. China Mater.*, **67**, 93 (2024); https://doi.org/10.1007/s40843-023-2666-1

84. F. Sagita, I.M. Arcana, G.T.M. Kadja. *Inorg. Chem. Commun.*, **175**, 114112 (2025); https://doi.org/10.1016/j.inoche.2025.114112

85. J. Xia, M. Lv, S. Zhang, Y. Xing, G. Zhou. *Materials Science and Engineering: R: Reports*, **164**, 100985 (2025); https://doi.org/10.1016/j.mser.2025.100985

86. X. Geng, L. Yang, P. Song. *Chemistry – A European Journal*, **30**, e202303451 (2024); https://doi.org/10.1002/chem.202303451

87. Z. Li, J. Liu, T. Wang, J. Zhu, C. Cheng, G. Ao, Z. Guan, J. Zhu. *Carbon*, **222**, 118966 (2024); https://doi.org/10.1016/j.carbon.2024.118966

88. Y. Jiang, R. Huang, X. Long, L. Lu, J. Liu, Z. Yang, Y. Yu, Y. Yang. *ACS Appl.*

Accepted manuscript
This manuscript will be edited, formatted and proofread. The file will be replaced with Version of Record.

Mater. Interfaces, **17**, 6969 (2025); https://doi.org/10.1021/acsami.4c20169

89. T. Li, C. Yang, H. Hao, Z. Yuan, Z. Yu, H. Liu. *J. Alloys Compd.*, **1022**, 180032 (2025); https://doi.org/10.1016/j.jallcom.2025.180032

90. D. Yang, J. Wang, C. Lou, M. Li, C. Zhang, A. Ramon, C. Li, M. Tang, G. Henkelman, M. Xu, J. Li, J. Llorca, J. Arbiol, D. Mitlin, G. Zhou, A. Cabot. *ACS Energy Lett.*, **9**, 2083 (2024); https://doi.org/10.1021/acsenergylett.4c00771

91. M. Wu, Z. Xing, R. Zhu, X. Liu, Y. Feng, W. Shao, R. Yan, B. Yin, S. Li. *Small*, **20**, 2306991 (2024); https://doi.org/10.1002/smll.202306991

92. S.A. Li, S.A. Novikova, I.A. Stenina, T.L. Kulova, A.M. Skundin, A.B. Yaroslavtsev. *Mendeleev Commun.*, **35**, 560 (2025); https://doi.org/10.71267/mencom.7767

93. R.M. Bhattarai, E. Nikam, K. Chhetri, C.-H. Chung, J. Hereijgers. *Prog. Mater Sci.*, **165**, 101859 (2027); https://doi.org/10.1016/j.pmatsci.2026.101859

94. J. Li, L. Liu, J. Qi, Q. Qin, Q. Zhao, B. Wang, S. Zheng. *J. Porous Mater.*, **29**, 1727 (2022); https://doi.org/10.1007/s10934-022-01314-1

95. A. Fu, C. Wang, F. Pei, J. Cui, X. Fang, N. Zheng. *Small*, **15**, 1804786 (2019); https://doi.org/10.1002/smll.201804786

96. B. Yu, C. Gyan-Barimah, J. Wang, M.I. Maulana, J.H. Sung, J.-H. Yu, S.-T. Hong, K. Wang, J.-S. Yu. *ACS Nano*, **19**, 37879 (2025); https://doi.org/10.1021/acsnano.5c11688

97. H. Zhang, Y. Zhao, C. Cai, L. Huang. *J. Mater. Chem. A*, **13**, 37568 (2025); https://doi.org/10.1039/D5TA07003A

98. J. Huangfu, P. Feng, X. Di, Y. Tian, M. Shi, W. Hu, X. Zhao, S. Wang, Y. Xi, F. Kong, H. Wang. *Adv. Energy Mater.*, **15**, 2502210 (2025); https://doi.org/10.1002/aenm.202502210

99. T. Yang, P. Dong, Z. Chen, X. Gan, L. Gu, Q. Lin, W. Yang. *ACS Appl. Mater. Interfaces*, **17**, 64677 (2025); https://doi.org/10.1021/acsami.5c19977

100. B. Liu, V.S. Thoi. *Chem. Commun.*, **58**, 4005 (2022);

Accepted manuscript
This manuscript will be edited, formatted and proofread. The file will be replaced with Version of Record.

https://doi.org/10.1039/d1cc07087h

101. S. Lv, X. Ma, S. Ke, Y. Wang, T. Ma, S. Yuan, Z. Jin, J.-L. Zuo. *Journal of the American Chemical Society*, **146**, 9385 (2024); https://doi.org/10.1021/jacs.4c01620

102. J. He, H. Liu, M. Li, Z. Cheng, X. Dou, J. Li, Y. Wang, X. Wang, P. Wang, Z. Liu. *Sci. China Chem.*, **68**, 6063 (2025); https://doi.org/10.1007/s11426-025-2908-9

103. G. Mu, M. Hu, Z. Cai, J. Xiao, F. Xiao, J. Xi, S. Wang. *J. Energy Chem.*, **113**, 126 (2026); https://doi.org/10.1016/j.jechem.2025.09.040

104. H. Zhang, M. Zhang, R. Liu, T. He, L. Xiang, X. Wu, Z. Piao, Y. Jia, C. Zhang, H. Li, F. Xu, G. Zhou, Y. Mai. *Nat. Commun.*, **15**, 5451 (2024); https://doi.org/10.1038/s41467-024-49826-5

105. J. Guo, J. Liu. *Nanoscale Adv.*, **1**, 2104 (2019); https://doi.org/10.1039/c9na00040b

106. M. Xu, X. Liu, Z. Zhao, L. Sun, L. Liu, J. Guo, J. Sha. *Chem. Eng. J.*, **491**, 152178 (2024); https://doi.org/10.1016/j.cej.2024.152178

107. S. Xi, Y. Zhidong, C. Yongqi, C. Jixuan, H. Heming, H. Yang, J. Qi. *J. Energy Storage*, **122**, 116630 (2025); https://doi.org/10.1016/j.est.2025.116630

108. L. Zhu, X. Zhang, Y. Song, K. Shi, X. Song, H. Liu, G. Wu. *Appl. Surf. Sci.*, **720**, 165296 (2026); https://doi.org/10.1016/j.apsusc.2025.165296

109. F. Zhou, Y. Meng, T. Wang, D. Sun, L. Gao, Z. Sun, Y. Wang, J. Zeng, B. Wang, R. Zhang, R. Li, C. Huang, L. Yang, X. Wang. *Nano Energy*, **127**, 109755 (2024); https://doi.org/10.1016/j.nanoen.2024.109755

110. X. Li, Z. Zhao, S. Yuan, J. Cheng, W. Hou, L. Hou, F. Liu, C. Yuan. *Energy Storage Mater.*, **86**, 104965 (2026); https://doi.org/10.1016/j.ensm.2026.104965

111. K. Zhang, Z. Zhao, H. Chen, Y. Pan, B. Niu, D. Long, Y. Zhang. *Small*, **21**, 2409674 (2025); https://doi.org/10.1002/smll.202409674

112. Z. Wang, Y. Song, L. Zhu, J. Song, X. Song, L. Chen. *Particuology*, **117**, 175

Accepted manuscript
This manuscript will be edited, formatted and proofread. The file will be replaced with Version of Record.

(2026); https://doi.org/10.1016/j.partic.2026.07.012

113. D. Son, C.-Y. Park, J. Kim, W.-G. Lim, S. Kim, J. Lee. *Angew. Chem. Int. Ed.*, **64**, e202425037 (2025); https://doi.org/10.1002/anie.202425037

114. Z. Hu, C. Geng, L. Wang, W. Lv, Q.-H. Yang. *Adv. Energy Sustainability Res.*, **5**, 2300148 (2024); https://doi.org/10.1002/aesr.202300148

115. L. Hong, L. Wu, S. Li, Z. Zhang, X. Chen, Y. Ma, Y. Wang, G. Shi, H. Pang. *J. Power Sources*, **633**, 236446 (2025); https://doi.org/10.1016/j.jpowsour.2025.236446

116. D. Li, H. Sun, C. Ma, C. Li, J. Wang, J. Niu, S. Yao. *J. Energy Storage*, **113**, 115698 (2025); https://doi.org/10.1016/j.est.2025.115698

117. X. Li, J. Yu, W. Li, Y. Liao, M. Li, B. Zhao, X. Liu, S. Huang, S. Xia, J. Zhang, Y. Jiang. *Chem. Eng. J.*, **505**, 159355 (2025); https://doi.org/10.1016/j.cej.2025.159355

118. J. Huang, Z. Huang, C. Zhang, T. Hao, T. Wang, D. Deng, Z. Sun, Y. Wang, C. Xu, J. Zeng, S. Tang, C. Huang, L. Yang, X. Wang. *Green Chem.*, **27**, 3326 (2025); https://doi.org/10.1039/D4GC05753H

119. Z. Li, L. Sun, K. Wang, Y. Zhang. *Mater. Today Sustainability*, **22**, 100392 (2023); https://doi.org/10.1016/j.mtsust.2023.100392

120. W. Meng, Y. Wang, X. Zhou, Z.-J. Chen, Y. Zhao, P.-C. Zhao, S. Yuan, Z. Jin, C.-H. Li. *Journal of the American Chemical Society*, **147**, 44479 (2025); https://doi.org/10.1021/jacs.5c16469

121. R. Liu, H. Cheng, W. Tai, Y. Chen, B. Zhao, Y. Sun, H. Hu. *ACS Sustainable Chem. Eng.*, **13**, 4108 (2025); https://doi.org/10.1021/acssuschemeng.4c10189

122. Y. Wu, M. Li, Y. Sun, Y. Chen, Y. Wang, C. Li, L. Wang, Q. Lv. *J. Colloid Interface Sci.*, **704**, 139333 (2026); https://doi.org/10.1016/j.jcis.2025.139333

123. Q. He, W. Chen, B. Fan, Q. Wei, Y. Zou. *Chem. Eng. J.*, **496**, 153813 (2024); https://doi.org/10.1016/j.cej.2024.153813

124. K. Mahankali, S. Nagarajan, N.K. Thangavel, S. Rajendran, M. Yeddala, L.M. Arava. *Catalysts*, **10**, 1137 (2020); https://doi.org/10.3390/catal10101137

Accepted manuscript
This manuscript will be edited, formatted and proofread. The file will be replaced with the Version of Record.

125. Z. Zhu, G. Fan, H. Huang, Y. Guo, X. Gu, J.S. Chen. *J. Mater. Chem. A*, **13**, 5632 (2025); https://doi.org/10.1039/D4TA06750A

126. W. Hu, H. Liu, F. Zhang, X. Wang, L. Pang, S. Wang, J. Li. *Chem. Eng. J.*, **513**, 163176 (2025); https://doi.org/10.1016/j.cej.2025.163176

127. Z. Hu, D. Jiang, L. Wang, L. Qu, Q. Su, K. Duan, M. Xiang, J. Guo, W. Bai, S. Chou. *Chem. Eng. J.*, **520**, 166018 (2025); https://doi.org/10.1016/j.cej.2025.166018

128. W. Wang, L. Bai, N. Li, S. Zhao, X. Shi, P. Wang. *Chin. Chem. Lett.*, **36**, 110938 (2025); https://doi.org/10.1016/j.cclet.2025.110938

129. L. Chen, P. Xu, Y. Chen, D. Chen, J.-J. Shao. *Langmuir*, **41**, 26428 (2025); https://doi.org/10.1021/acs.langmuir.5c03703

130. I. Mohammad, A. Bekzhanov, Y. Surace, D. Cupid. *Energy Adv.*, **4**, 1363 (2025); https://doi.org/10.1039/D5YA00206K

131. S. Xue, C. Hai, Y. Sun, S. Dong, L. Ma, X. He, Q. Xu, Y. Zhou. *Mater. Res. Bull.*, **186**, 113340 (2025); https://doi.org/10.1016/j.materresbull.2025.113340

132. R.C. Rodríguez, P.S. Cappellari, G.Á. Planes, A. Caballero, A.Y. Tesio. *J. Energy Storage*, **140**, 118893 (2025); https://doi.org/10.1016/j.est.2025.118893

133. Q. Xu, H. Liu, S. Lv, Y. Han, X. Ji, C. Ma, J. Li, Z. Zhang, Y. Jin, Q. Xie, H. Liu. *J. Energy Chem.*, **111**, 719 (2025); https://doi.org/10.1016/j.jechem.2025.08.016

134. J. Lan, R. Hou, G. Wang, F. Miao, G. Shao, P. Zhang. *Adv. Funct. Mater.*, **35**, 2421930 (2025); https://doi.org/10.1002/adfm.202421930

135. T. Boteju, A. Sivakumaran, S. Ponnurangam, V. Thangadurai. *ACS Appl. Mater. Interfaces*, **17**, 56153 (2025); https://doi.org/10.1021/acsami.5c12948

136. C. Wang, P. Zhang, J. Li, R. Wang, C. Yang, F. Yu, X. Zhao, K. Zhao, X. Zheng, H. Zhang, T. Yang. *Nano-Micro Lett.*, **18**, 7 (2025); https://doi.org/10.1007/s40820-025-01849-3

137. L. Chen, X. Chen, J. Xiao. *J. Energy Storage*, **118**, 116241 (2025); https://doi.org/10.1016/j.est.2025.116241

Accepted manuscript
This manuscript will be edited, formatted and proofread. The file will be replaced with Version of Record.

138. Z. Yang, W. Lu, C. Sun, M. Yao, N. Chen, H. Jiang, C. Wang, D. Zhang, F. Du. *J. Colloid Interface Sci.*, **685**, 235 (2025); https://doi.org/10.1016/j.jcis.2025.01.095

139. J. Jiang, Y. Ding, S. Pan, Z. Wu, X. Wang, J. Zhu, Y. Fu. *Industrial & Engineering Chemistry Research*, **64**, 9176 (2025); https://doi.org/10.1021/acs.iecr.5c00203

140. Q. Wu, A. Gao, H. Chen, Y. Pan, X. Wang, B. Niu, Y. Zhang, D. Long. *ACS Appl. Energy Mater.*, **8**, 6557 (2025); https://doi.org/10.1021/acsaem.5c00453

141. F. Han, L. Zhang, Q. Jin, X. Ma, Z. Zhang, Z. Sun, X. Zhang, L. Wu. *ACS Nano*, **19**, 9182 (2025); https://doi.org/10.1021/acsnano.4c18642

142. F. Han, Z. Wang, Q. Jin, L. Fan, K. Tao, L. Li, L. Shi, H.-Q. Lu, Z. Zhang, J. Li, X. Zhang, L. Wu. *ACS Nano*, **18**, 15167 (2024); https://doi.org/10.1021/acsnano.4c03031

143. H. Raza, J. Cheng, J. Xu, L. An, J. Wang, W. Nie, G. Zheng, G. Chen. *Energy Environ. Mater.*, **8**, e70007 (2025); https://doi.org/10.1002/eem2.70007

144. J. Wang, W.-Q. Han. *Adv. Funct. Mater.*, **32**, 2107166 (2022); https://doi.org/10.1002/adfm.202107166

145. J. Zhang, D. Yang, C. Li, Q. Gong, W. Bi, W.-H. Lai, S. Li, Y. Lei, G. Zhou, A. Cabot, G. Wang. *Energy Environ. Sci.*, **18**, 7905 (2025); https://doi.org/10.1039/D5EE00262A

146. X. Guo, M. Yang, J. Hou, H. Li, Z. Liu, Y. Cui, D. Shi, H. Hu, B. Zhang, Y. Shao, Y. Wu, X. Hao. *Chem. Eng. J.*, **513**, 162955 (2025); https://doi.org/10.1016/j.cej.2025.162955

147. D. Su, Y. Zeng, M. Geng, T. Wang, M. Shao, C. Li, Z. Wei. *Chem. Commun.*, **61**, 5990 (2025); https://doi.org/10.1039/D5CC00529A

148. B. Lu, L. Hu, X. Yan, Y. Xia, X. He, J. Zhang, R. Fang, W. Zhang, Y. Gan, M. Fan, X. Xia, H. Huang. *Electrochim. Acta*, **537**, 146877 (2025); https://doi.org/10.1016/j.electacta.2025.146877

149. Y. Min, X. Zou, Q. Lu, W. Cai, Y. Bu. *Small*, **21**, 2411794 (2025);

Accepted manuscript
This manuscript will be edited, formatted and proofread. The file will be replaced with Version of Record.

https://doi.org/10.1002/smll.202411794

150. G. Tang, T. Yuan, L. Bi, Y. Li, Z. Wu, L. Ma. *Chem. Commun.*, **62**, 10387 (2026); https://doi.org/10.1039/d6cc01678b

151. Y. Zheng, L. Li, Y. Jiao, Y. Zhang, B. Peng, J. Xu, L. Ma. *Nano Res.*, **18**, 94907542 (2025); https://doi.org/10.26599/NR.2025.94907542

152. Y. Jiang, R. Yang, H. Li, Q. Zhang, X. Dong, H. Shang, J.-H. Ahn, B. Jiang, Y. Yan. *J. Power Sources*, **650**, 237500 (2025); https://doi.org/10.1016/j.jpowsour.2025.237500

153. Y. Yao, C. Zhou, Z.-L. Zhao, G.-G. Chang, J.-K. Wei, K.-X. Huang, J.-J. Xie, J.-S. Li, X.-Y. Yang. *Carbon*, **223**, 119018 (2024); https://doi.org/10.1016/j.carbon.2024.119018

154. J. Lan, G. Hu, Y. Yu, P. Zhang, G. Shao, F. Miao. *J. Energy Chem.*, **107**, 792 (2025); https://doi.org/10.1016/j.jechem.2025.03.076

155. S. Luo, J. Lu, Z. Qi, J. Ruan, Z. Li, J. Li, T. Yuan, Y. Pang, S. Zheng. *J. Colloid Interface Sci.*, **701**, 138691 (2026); https://doi.org/10.1016/j.jcis.2025.138691

156. S. Li, L. Li, H. Yang, Z. Wang, X. Deng, W. Lu, W. Xu. *Energy Environ. Sci.*, **19**, 1458 (2026); https://doi.org/10.1039/D5EE05863E

157. J. Yang, L. Chen. *Ionics*, **30**, 1 (2024); https://doi.org/10.1007/s11581-023-05274-7

158. J. Yu, O. Usoltsev, I. Martynova, C. Huang, Z. Liang, I. Pinto-Huguet, C. Li, L. Lu, C. Zhang, X. Lu, K. Gupta, M. Botifoll, L. Simonelli, F. Fauth, J.Y. Zhou, J. Llorca, Y. Lu, C.Y. Zhang, J. Arbiol, A. Cabot. *Adv. Mater.*, **38**, e11345 (2026); https://doi.org/10.1002/adma.202511345

159. T. Hou, N. Duan, C. Bi, J. Tu, M. Luo, Y. Qu, Y. Yang, D. Wang, Q. Chen. *ACS Nano*, **19**, 38654 (2025); https://doi.org/10.1021/acsnano.5c13298

160. Y. Zhang, G. Zheng, M. Demir, Y. He, P. Saha, H. Jiang, Q. Cheng. *J. Energy Storage*, **125**, 116966 (2025); https://doi.org/10.1016/j.est.2025.116966

161. L. Sun, H. Xu, J. Xie, Y. Yuan, H. Wang, M. Wang, X. Chen, Z. Jin. *Adv. Funct. Mater.*, **35**, 2416826 (2025); https://doi.org/10.1002/adfm.202416826

Accepted manuscript
This manuscript will be edited, formatted, and proofread. The file will be replaced with version of Record.

162. Z. Guo, Z. Cui, A. Manthiram. *Adv. Funct. Mater.*, **35**, 2501743 (2025); https://doi.org/10.1002/adfm.202501743

163. A.V. Saravanan, K. Lakshmanan, B.W. Taklu, Y. Nikodimos, E.A. Moges, C.-C. Chang, G.G. Serbessa, B.D. Dandena, E.B. Tamilarasan, S.-H. Wu, W.-N. Su, C.-C. Yang, B.J. Hwang. *ACS Appl. Energy Mater.*, **9**, 8137 (2026); https://doi.org/10.1021/acsaem.6c00646

164. Y. Liu, Y. Elias, J. Meng, D. Aurbach, R. Zou, D. Xia, Q. Pang. *Joule*, **5**, 2323 (2021); https://doi.org/10.1016/j.joule.2021.06.009

165. J. Phung, X. Zhang, W. Deng, G. Li. *Sustainable Mater.Technol.*, **31**, e00374 (2022); https://doi.org/10.1016/j.susmat.2021.e00374

166. R. Mukkabla, M.R. Buchmeiser. *J. Mater. Chem. A*, **8**, 5379 (2020); https://doi.org/10.1039/c9ta12619h

167. Q. Zhang, Q. Huang, S.-M. Hao, S. Deng, Q. He, Z. Lin, Y. Yang. *Adv. Sci.*, **9**, 2103798 (2022); https://doi.org/10.1002/advs.202103798

168. X. Li, D. Liu, Z. Cao, Y. Liao, Z. Cheng, J. Chen, K. Yuan, X. Lin, Z. Li, Y. Huang, L. Yuan. *J. Energy Chem.*, **84**, 459 (2023); https://doi.org/10.1016/j.jechem.2023.05.052

169. H. Xiang, N. Deng, H. Zhao, X. Wang, L. Wei, M. Wang, B. Cheng, W. Kang. *J. Energy Chem.*, **58**, 523 (2021); https://doi.org/10.1016/j.jechem.2020.10.029

170. Z. Ji, L. Feng, Z. Zhu, X. Fu, W. Yang, Y. Wang. *Chem. Eng. J.*, **455**, 140462 (2023); https://doi.org/10.1016/j.cej.2022.140462

171. M. Li, H. Wang, G. Yan, Z. Hu, Y. Feng, X. Zhang. *ACS Appl. Mater. Interfaces*, **16**, 12637 (2024); https://doi.org/10.1021/acsami.3c18930

172. S. Wang, Y. Wu, M. Yang, L. Sun, Y. Tao, C.-A. Yang. *New J. Chem.*, **48**, 621 (2024); https://doi.org/10.1039/D3NJ04155G

173. Y. Wu, M. Yang, S. Wang, S. Hou, Y. Zou, Y. Tao, C. Yang. *J. Alloys Compd.*, **962**, 171177 (2023); https://doi.org/10.1016/j.jallcom.2023.171177

174. P. Zhao, H. Cheng, H. Liu, J. Liu, K. Song, H. Hu. *J. Alloys Compd.*, **1003**, 175529 (2024); https://doi.org/10.1016/j.jallcom.2024.175529

Accepted manuscript
This manuscript will be edited, formatted and proofread. The file will be replaced with Version of Record.

175. S. Choudhury, M. Akef, A. Seifert, M. Göbel, M. Gruschwitz, R. Matsidik, C. Tegenkamp, M. Sommer. *ACS Appl. Mater. Interfaces*, **16**, 6301 (2024); https://doi.org/10.1021/acsami.3c09316

176. M. Zhu, H. Zhao, K. Quan, H. Chen, S. Zhang, H. Yi, J. Zhang. *Electrochim. Acta*, **474**, 143503 (2024); https://doi.org/10.1016/j.electacta.2023.143503

177. W.I. Kim, J.C. Shin, M.J. Kim, G. Jang, M. Lee, H.S. Park. *ACS Energy Lett.*, **10**, 2410 (2025); https://doi.org/10.1021/acsenergylett.5c00808

178. J. Wang, W. Zhang, H. Wei, X. Zhai, F. Wang, Y. Zhou, F. Tao, P. Zhai, W. Liu, Y. Liu. *Sustainable Energy Fuels*, **6**, 2901 (2022); https://doi.org/10.1039/d2se00254j

179. L. Li, J. Yang, G. Duan, C. Zhang, K. Liu, S. Jiang, H. Hou. *J. Energy Storage*, **90**, 111933 (2024); https://doi.org/10.1016/j.est.2024.111933

180. Y. Wang, B. Yue, X. Yan, Y. Fang, J. Wang, Q. Ma, G. Liu, W. Yu, X. Dong. *Chem. Eng. J.*, **518**, 164649 (2025); https://doi.org/10.1016/j.cej.2025.164649

181. L. Sun, H. Liu, X. Gui, L. Liu, D. Li, X. Sun, Y. Xue, C. Luo, K. Xu. *J. Energy Storage*, **129**, 117376 (2025); https://doi.org/10.1016/j.est.2025.117376

182. N. Yang, J. Zhang, Y. Ji, W. Zhang, J. Xue, X. He, Q. Li, Z. Lei, Z. Liu, J. Sun. *ACS Sustainable Chem. Eng.*, **13**, 1378 (2025); https://doi.org/10.1021/acssuschemeng.4c09127

183. N. Sapkota, S. Chiluwal, P. Parajuli, A. Rowland, R. Podila. *Adv. Sci.*, **10**, 2206901 (2023); https://doi.org/10.1002/advs.202206901

184. C.-Y. Zhang, C.-Y. Wang, E.-Z. Zhao, G. Yu, H.-L. Deng, R. Huang, Z.-Y. Wang, P. Hu, M. Yan, Z. Liu. *Chem. Eng. J.*, **522**, 167622 (2025); https://doi.org/10.1016/j.cej.2025.167622

185. B.L. Souza, R. Müller, N. Kardjilov, E. Härk, P.F.M. de Oliveira, I. Manke, S. Risse, R.M. Torresi. *J. Power Sources*, **657**, 238156 (2025); https://doi.org/10.1016/j.jpowsour.2025.238156

186. Y. Zhang, W. Wang, Z. Jia, J. Ding, L. Hua, M. Sun, Y. Li, G. Wang, C. Li. *Energy Storage Mater.*, **67**, 103320 (2024);

Accepted manuscript
This manuscript will be edited, formatted, and proofread. There will be replaced with Version of Record.

https://doi.org/10.1016/j.ensm.2024.103320

187. J. Lu, M. Zhu, C. Wang, L. Wang, C. Wu, Y. Cui, Q. Bi, S. Jiang, Q. Zhao, X. Li, A. He, S.H. Lee, Q. Li. *ACS Sustainable Chem. Eng.*, **13**, 21405 (2025); https://doi.org/10.1021/acssuschemeng.5c06841

188. E.V. Karaseva, L.A. Khramtsova, A.N. Lobov, E.V. Kuzmina, D. Eroglu, V.S. Kolosnitsyn. *J. Power Sources*, **548**, 231980 (2022); https://doi.org/10.1016/j.jpowsour.2022.231980

189. G. Li, Z. Li, B. Zhang, Z. Lin. *Front. Energy Res.*, **Volume 3 - 2015** (2015); https://doi.org/10.3389/fenrg.2015.00005

190. H. Shi, W. Sun, J. Cao, S. Han, G. Lu, Z.A. Ghazi, X. Zhu, H. Lan, W. Lv. *Adv. Funct. Mater.*, **33**, 2306933 (2023); https://doi.org/10.1002/adfm.202306933

191. D. Ovc-Okene, L.S. Shankar, A. Vizintin, R. Kun. *RSC Adv.*, **15**, 5381 (2025); https://doi.org/10.1039/d4ra06245k

192. X. Yao, Z. Wang, S. Lu, H. Tu, J. Xu, X. Ma, K. Liang, Y. Lin, A. Chen, S. Xu, J. Ren, K. Wang, F. Zhang, J. Zheng, X. Wu, H. Li. *Angew. Chem. Int. Ed.*, **64**, e202519315 (2025); https://doi.org/10.1002/anie.202519315

193. D.J. Kautz, X. Cao, P. Gao, S. Feng, Q. Zhao, S. Parab, Y. Xu, J.P. Quinn, M.M. Rahman, S. Tan, X. Zhang, S. Ketabi, A. Nazir, J. Wang, F. Dai, S. Wang, D. Lu, E. Hu, Y.S. Meng, C. Wang, J. Liu, J.-G. Zhang, W. Xu. *Adv. Mater.*, **37**, 2503365 (2025); https://doi.org/10.1002/adma.202503365

194. J.S. Searle, F. Malagreca, B.M.G. Denison, A.J. Kibler, D.A. Walsh, L.R. Johnson, D.B. Amabilino, G.N. Newton. *ACS Energy Lett.*, **10**, 2839 (2025); https://doi.org/10.1021/acsenergylett.5c01262

195. M.-Y. Li, B.-B. Zou, Y. Yan, T.-T. Wang, X. Liu, H.-J. Peng. *J. Energy Chem.*, **106**, 710 (2025); https://doi.org/10.1016/j.jechem.2025.03.005

196. H. Dai, C. Gallagher, S.-M. Bak, L. Gomes, K. Yang, R. Dong, S. Badhrinathan, Q. Zhao, Y. Du, G.P. Pandey, S. Mukerjee. *Energy Storage Mater.*, **76**, 104123 (2025); https://doi.org/10.1016/j.ensm.2025.104123

197. Z. Li, Y. Li, Y. Fei, P. Li, S.-Y. Hung, H. Zhang, G. Li. *Adv. Mater.*, **37**, 2505196

Accepted manuscript
This manuscript will be edited, formatted, and proofread. The file will be replaced with Version of Record.

(2025); https://doi.org/10.1002/adma.202505196

198. P. Li, Z. Luo, Z. Chen, H. Liu, Y. Liu, J. Guan, J. Jiang, D. Cai, S. Yang, Z. Yang. *Adv. Mater.*, **37**, e11272 (2025); https://doi.org/10.1002/adma.202511272

199. L.-L. Su, M.-X. Wu, S.-Y. Sun, C.-X. Bi, Z. Zheng, M. Zhao, B.-Q. Li, X.-Q. Zhang, J.-Q. Huang. *ACS Energy Lett.*, **10**, 313 (2025); https://doi.org/10.1021/acsenergylett.4c03177

200. I. Kim, S. Kim, H. Cho, J. Jung, H. Kwon, D. Kim, Y. Shin, H.-T. Kim. *Adv. Energy Mater.*, **15**, 2403828 (2025); https://doi.org/10.1002/aenm.202403828

201. S. Gu, Y. Zhang, M. Li, Q. Lin, C. Zhao, G. Xu, N. Zhang. *Small*, **20**, 2406923 (2024); https://doi.org/10.1002/smll.202406923

202. J. Gu, Z. Li, B. Hong, M. Wang, Z. Zhang, Y. Lai, J. Li, L. Zhang. *ACS Appl. Mater. Interfaces*, **16**, 61934 (2024); https://doi.org/10.1021/acsami.4c11693

203. Z. Zhao, B.Z. Desalegn, H.J. Joe, S.K. Kim, J. Yoo, D. Wang, J.G. Seo. *Energy Storage Mater.*, **73**, 103862 (2024); https://doi.org/10.1016/j.ensm.2024.103862

204. R. Wang, M. Jiang, G. Xu, Z. Deng, W. Bao, X. Yang. *ACS Sustainable Chem. Eng.*, **12**, 16671 (2024); https://doi.org/10.1021/acssuschemeng.4c06125

205. Z. Shi, S. Thomas, D. Guo, Z. Tian, Z. Zhao, Y. Wang, A.-H. Emwas, N. Wehbe, G. Melinte, O.M. Bakr, O.F. Mohammed, H.N. Alshareef. *ACS Energy Lett.*, **9**, 5391 (2024); https://doi.org/10.1021/acsenergylett.4c02049

206. F. Liu, D. Xu, Z. Liu, L. Wang, M. Chen, D. Zhou, Z. Xiao. *Adv. Funct. Mater.*, **35**, 2412923 (2025); https://doi.org/10.1002/adfm.202412923

207. V.R. Shah, R. Sinha, W.J. Cesarski, X. Gao, S.F. Yuk, Y.L. Joo. *ACS Appl. Mater. Interfaces*, **16**, 53950 (2024); https://doi.org/10.1021/acsami.4c12157

208. J.-H. Zhang, X.-Z. Fan, X.-H. Zhou, R.-J. Hu, N. Du, C. Guan, S.-B. Han, B.-Q. Li, L. Kong. *Energy Storage Mater.*, **73**, 103786 (2024); https://doi.org/10.1016/j.ensm.2024.103786

209. P. Sang, S. Tang, F. Li, Y. Si, Y. Fu. *Small*, **20**, 2406972 (2024); https://doi.org/10.1002/smll.202406972

Accepted manuscript
This manuscript will be edited, formatted and proofread. The file will be replaced with version of Record.

210. Y. Meng, M. Zhang, Y. Wang, C. Liu, Z. Zhang, J. Yu, J. Cai, Z. Yang. *Sci. China Mater.*, **67**, 2880 (2024); https://doi.org/10.1007/s40843-024-2969-3

211. Q. Yang, S. Shen, Z. Han, G. Li, D. Liu, Q. Zhang, L. Song, D. Wang, G. Zhou, Y. Song. *Adv. Mater.*, **36**, 2405790 (2024); https://doi.org/10.1002/adma.202405790

212. K. Qin, S. Li, D. Yen, W. Zhang, Z. Yang, E.P. Kamphaus, E.Y. Kim, J. Huang, J.J. Shea, E. Hu, L. Cheng, C. Wang, C. Luo. *ACS Energy Lett.*, **9**, 3869 (2024); https://doi.org/10.1021/acsenergylett.4c00859

213. K. Liao, M.-H. Pai, A. Manthiram. *Adv. Energy Mater.*, **15**, 2403733 (2025); https://doi.org/10.1002/aenm.202403733

214. A.L. Phan, B. Nan, P.M.L. Le, Q. Miao, Z. Wu, K. Le, F. Chen, M. Engelhard, T. Dan Nguyen, K.S. Han, J. Heo, W. Zhang, M. Baek, J. Xu, X. Zhang, P. Liu, L. Ma, C. Wang. *Adv. Mater.*, **36**, 2406594 (2024); https://doi.org/10.1002/adma.202406594

215. D. Guo, S. Thomas, J.K. El-Demellawi, Z. Shi, Z. Zhao, C.G. Canlas, Y. Lei, J. Yin, Y. Zhang, M.N. Hedhili, M. Arsalan, Y. Zhu, O.M. Bakr, O.F. Mohammed, H.N. Alshareef. *Energy Environ. Sci.*, **17**, 8151 (2024); https://doi.org/10.1039/D4EE03191A

216. X. Liu, S. Wu, Z. Hao, L. Shang, M. Guo, J. Hou, S. Shao, H. Li, Y. Li, Y. Lu, K. Zhang, Z. Yan, J. Chen. *Angew. Chem. Int. Ed.*, **64**, e202416731 (2025); https://doi.org/10.1002/anie.202416731

217. K. Yu, G. Cai, M. Li, J. Wu, V. Gupta, D.J. Lee, J. Holoubek, Z. Chen. *ACS Appl. Mater. Interfaces*, **15**, 43724 (2023); https://doi.org/10.1021/acsami.3c08338

218. R. Gao, B. Huang, M. Zhang, X. Wu, Y. Song, X. Xiao, Z. Piao, Z. Lao, Z. Han, G. Zhou. *Adv. Mater.*, **37**, 2502210 (2025); https://doi.org/10.1002/adma.202502210

219. W. Han, J. Hou, F. Wang, B. Zhang, E. Zhang, Y. Wang, C. Yang, P. Dong, W. Song, X. Li, Y. Zhang, S. Lou, Y. Zhang, Y. Zhang. *Mater. Horiz.*, **12**, 1473 (2025); https://doi.org/10.1039/D4MH01504E

Accepted manuscript
This manuscript will be edited, formatted and proofread. The file will be replaced with Version of Record.

220. H. Cho, J. Jung, I. Kim, J. Kim, S. Kim, J. Hyun, C.H. Lee, H. Kwack, W. Oh, J. Lee, H.-T. Kim. *Nat. Commun.*, **16**, 6805 (2025); https://doi.org/10.1038/s41467-025-62169-z

221. Q. Zheng, L. Cui, X. Zhao, R. Yuan, C. Wang, K. Wang, J. Fan, M. Zheng, Q. Dong. *Adv. Energy Mater.*, **15**, 2500802 (2025); https://doi.org/10.1002/aenm.202500802

222. T. Jin, X.-Y. Li, M. Zhao, S. Feng, Z. Li, Z.-X. Chen, H.-J. Peng, B.-Q. Li, J.-Q. Huang. *Angew. Chem. Int. Ed.*, **64**, e202504898 (2025); https://doi.org/10.1002/anie.202504898

223. M.S. Kim, L. Ma, S. Choudhury, L.A. Archer. *Adv. Mater. Interfaces*, **3**, 1600450 (2016); https://doi.org/10.1002/admi.201600450

224. S. Xia, X. Xu, W. Wu, Y. Chen, L. Liu, G. Wang, L. Fu, Q. Zhang, T. Wang, J. He, Y. Wu. *Materials Science and Engineering: R: Reports*, **163**, 100924 (2025); https://doi.org/10.1016/j.mser.2025.100924

225. S.-W. Seo, J.-J. Yang, Y.-S. Oh, M. Jeong, S.-J. Park, S. Ahn. *Chem. Phys. Lett.*, **882**, 142479 (2026); https://doi.org/10.1016/j.cplett.2025.142479

226. X. Wu, Q. Xia, L. Zhang, M. Jing, Q. He, Q. Zhang, X. Shen, W. Yuan. *J. Colloid Interface Sci.*, **701**, 138675 (2026); https://doi.org/10.1016/j.jcis.2025.138675

227. Z. Qiao, X. Liu, L. Yuan, H. Lei. *J. Alloys Compd.*, **1030**, 180815 (2025); https://doi.org/10.1016/j.jallcom.2025.180815

228. Z. Zhang, D. Chen, F. Ma, X. Li, H. Yu, Y. Wang, J. Huang, Y. Wu, Y. Chen. *Chem. Eng. J.*, **516**, 164150 (2025); https://doi.org/10.1016/j.cej.2025.164150

229. B. Sun, B. Jia, H. Yu, C. Yao, W. Xie, Y. Xu. *J. Power Sources*, **632**, 236325 (2025); https://doi.org/10.1016/j.jpowsour.2025.236325

230. Q. Wang, H. Kim, Z. Li, L. Song, W.-S. Yoon, R.N. Bulakhe, J.M. Kim. *Chem. Eng. J.*, **507**, 160588 (2025); https://doi.org/10.1016/j.cej.2025.160588

231. X. Wang, N. Zou, Y. Qiao, G. Ren, Q. Wang, T. Zhou, Y. Chen. *Chem. Eng. J.*, **515**, 163529 (2025); https://doi.org/10.1016/j.cej.2025.163529

Accepted manuscript
This manuscript will be edited, formatted, and proofread. The file will be replaced with Version of Record.

232. T.-S. Li, Y. Liu, X.-C. Zhang, L.-N. Zhang, Y.-C. Wu, X.-Y. Jiang, Q.-P. Zhou, C. Ma, L.-B. Ni, G.-W. Diao. *J. Energy Chem.*, **104**, 551 (2025); https://doi.org/10.1016/j.jechem.2025.01.011

233. L. Sun, J. Li, Z. Li, W. Li, G. Lv, L. Liao. *Appl. Mater. Today*, **44**, 102677 (2025); https://doi.org/10.1016/j.apmt.2025.102677

234. L. Wu, Z. Jin, X. Xie, F. Lian, J. Lu, W. Wang. *Energy Storage Mater.*, **77**, 104167 (2025); https://doi.org/10.1016/j.ensm.2025.104167

235. S. Mohapatra, A. Joshi, V. Gusain, S. Bandyopadhyay, T.S. Anand, J. Kala, B.K. Mani, A. Gupta, R.K. Srivastava, B. Nandan. *Adv. Funct. Mater.*, **n/a**, e26627 (2025); https://doi.org/10.1002/adfm.202526627

236. Z.-H. Luo, M. Zheng, M.-X. Zhou, X.-T. Sheng, X.-L. Chen, J.-J. Shao, T.-S. Wang, G. Zhou. *Adv. Mater.*, **37**, 2417321 (2025); https://doi.org/10.1002/adma.202417321

237. L.D.J. Barter, S.J. Hinder, J.F. Watts, R.C.T. Slade, C. Crean. *Batteries*, **11**, 266 (2025); https://doi.org/10.3390/batteries11070266

238. X. Chen, C. Yu, B. Chen, Z. Du, W. Ai. *Chem. Commun.*, **61**, 5617 (2025); https://doi.org/10.1039/D5CC00331H

239. J. Liu, X. Wang, T. Gao, W. Yang, Q. Jian, B. Li, L. He, Y. Ruan. *RSC Adv.*, **15**, 9875 (2025); https://doi.org/10.1039/D5RA00172B

240. G. Tang, G. Deng, Z. Jiang, W. Xi, Y. Zhang, R. Wang, Y. Gong, H. Wang, J. Jin. *J. Mater. Chem. A*, **13**, 39775 (2025); https://doi.org/10.1039/D5TA05580F

241. E. Bellinetto, V.K. Tomer, R. Malik, S. Paul, C.V. Singh, S. Turri, M. Sain, G. Griffini. *Energy Environ. Mater.*, **n/a**, e70190 (2025); https://doi.org/10.1002/eem2.70190

242. H. Li, L. Peng, Z. Wang, Y. Bai, K. Sun. *Industrial & Engineering Chemistry Research*, **64**, 15120 (2025); https://doi.org/10.1021/acs.iecr.5c00851

243. S. Lu, L. Cai, J. Wang, H. Ying, Z. Han, W. Han, Z. Chen. *Small*, **20**, 2307784 (2024); https://doi.org/10.1002/smll.202307784

244. T. Wang, Z. Shi, F. Wang, S. Cui, Z. Zhang, W. Liu, Y. Jin. *ACS Appl. Mater.*

Accepted manuscript
This manuscript will be edited, formatted, and proofread. The file will be replaced with version of Record.

Interfaces, **16**, 18937 (2024); https://doi.org/10.1021/acsami.4c01160

245. N. Xu, Y. Hu, B. Sun, W. Xie, C. Yao, Y. Xu, J. Qi. *ACS Appl. Polym. Mater.*, **6**, 13813 (2024); https://doi.org/10.1021/acsapm.4c02692

246. H. Raza, J. Cheng, S. Kandasamy, M. Madithedu, N. Tewari, I.T. Bello, J. Wei, J. Xu, L. An, G. Zheng, S.T. Boles. *Energy Environ. Mater.*, **8**, e70058 (2025); https://doi.org/10.1002/eem2.70058

247. L. Du, J. Sun, Y. Zhang, Y. Wang, Z. Liu, M. Yao, Q. Wang, Y. Tang, Y. Zhang. *Adv. Mater.*, **37**, e08523 (2025); https://doi.org/10.1002/adma.202508523

248. C. Ma, S. Zhao, H. Chen, F. Lu, J. Wang, X. Weng, L. Tan, L. Yang, M. Jin, X. Wang, K. Zong, D. Luo, Z. Chen. *Carbon Energy*, **7**, e70033 (2025); https://doi.org/10.1002/cey2.70033

249. X. Kang, T. He, H. Dang, X. Li, Y. Wang, F. Zhu, F. Ran. *Nano-Micro Lett.*, **17**, 277 (2025); https://doi.org/10.1007/s40820-025-01733-0

250. J. Xi, B. Zhao, Y. Lv, Y. Yuan, P. Du. *ACS Appl. Mater. Interfaces*, **17**, 50765 (2025); https://doi.org/10.1021/acsami.5c12067

251. K. Chhetri, D. Acharya, R.S. Pawale, K.-H. Kong, I. Pathak, Y.R. Rosyara, R.M. Bhattarai, P.C. Lohani, T. Kim, N.H. Kim, J.H. Lee, B.-S. Kim, J. Hereijgers, C.-H. Chung, H. Cho, T.H. Ko, H.Y. Kim. *"Composites, Part B"*, **310**, 113159 (2026); https://doi.org/10.1016/j.compositesb.2025.113159

252. K. Liu, H. Zhao, D. Ye, J. Zhang. *Chem. Eng. J.*, **417**, 129309 (2021); https://doi.org/10.1016/j.cej.2021.129309

253. M.S. Ahmed, S. Lee, M. Agostini, M.-G. Jeong, H.-G. Jung, J. Ming, J. Kim, J.-Y. Hwang. *Adv. Sci.*, **8**, 2170139 (2021); https://doi.org/10.1002/advs.202170139

254. T.-H. Tsai, Y.-S. Su. *RSC Applied Interfaces*, **2**, 1105 (2025); https://doi.org/10.1039/d5lf00157a

255. D.J. Kim, H.W. Jung, T.H. Hong, S.M. Ko, J.S. Lee, J.T. Lee. *Energy Storage Mater.*, **83**, 104682 (2025); https://doi.org/10.1016/j.ensm.2025.104682

256. L. Tian, L. Li, Z. Ren, W. Yuan. *Small*, **21**, 2503389 (2025);

Accepted manuscript
This manuscript will be edited, formatted, and proofread. The file will be replaced with Version of Record.

https://doi.org/10.1002/smll.202503389

257. X. Zhang, H.-C. Lu, C.-R. Hao, J.-Q. Liu, X.-R. Kong, J.-L. Wang. *Chem. Eng. J.*, **500**, 156857 (2024); https://doi.org/10.1016/j.cej.2024.156857

258. Z. Shi, Y. Wang, M. Liu, J. Ma, H. Yue, Z. Hu, S.-T. Yang, Y. Yin. *ACS Sustainable Chem. Eng.*, **12**, 17806 (2024); https://doi.org/10.1021/acssuschemeng.4c07155

259. R. He, Y. Li, Z. Mu, H. Liu, Y. Zhang, X. Zhang. *ACS Appl. Nano Mater.*, **6**, 23163 (2023); https://doi.org/10.1021/acsanm.3c04539

260. Q. Wu, M. Qin, Y. Wu, H. Zhu, S. Cheng, J. Xie. *J. Mater. Chem. A*, **11**, 22913 (2023); https://doi.org/10.1039/D3TA04860H

261. W. Tai, H. Cheng, R. Liu, Y. Chen, B. Sun, Z. Jiang, B. Zhao, M. Liu, H. Hu. *J. Power Sources*, **636**, 236579 (2025); https://doi.org/10.1016/j.jpowsour.2025.236579

262. C. Sun, Y. Wang, Q. Zhou, Y. Xin, H. Gao. *Chem. Eng. J.*, **525**, 169050 (2025); https://doi.org/10.1016/j.cej.2025.169050

263. S. Yang, Q. Sun. *J. Ind. Eng. Chem.*, **143**, 144 (2025); https://doi.org/10.1016/j.jiec.2024.08.018

264. T. Shi, M.-Y. Zhang, Q. Sun. *J. Ind. Eng. Chem.*, **138**, 123 (2024); https://doi.org/10.1016/j.jiec.2024.03.046

265. X. Li, Y. Song, Z. Yan, J. Wang, F. Ding, Z. Chen, H. Wang, J. Li. *Electrochim. Acta*, **542**, 147523 (2025); https://doi.org/10.1016/j.electacta.2025.147523

266. H.-C. Huang, Y.-Y. Chen, Y.A. Lin. *ACS Appl. Energy Mater.*, **8**, 4618 (2025); https://doi.org/10.1021/acsaem.5c00242

267. A. Tao, K. Zhang, X. Ma, X. Song, J. Liang, Y. Wang, Y. Liu, L. Jin, Z. Tie, Z. Jin. *ACS Energy Lett.*, **8**, 79 (2023); https://doi.org/10.1021/acsenergylett.2c02107

268. D. Kuai, S. Wang, S. Perez-Beltran, S. Yu, G.A. Real, P. Liu, P.B. Balbuena. *ACS Energy Lett.*, **9**, 810 (2024); https://doi.org/10.1021/acsenergylett.3c02757

269. W. Zuo, R. Li, X. Wu, Y. Guo, S. Zhou, B. Wen, J. Luo, L. Zhang. *Chem. Eng.*

Accepted manuscript
This manuscript will be edited, formatted and proof read. The file will be replaced with Version of Record.

J., **491**, 151977 (2024); https://doi.org/10.1016/j.cej.2024.151977

270. Q. Wu, Y. Wu, H. Yan, W. Zhong, M. Qin, H. Zhu, S. Cheng, J. Xie. *Energy Environ. Sci.*, **18**, 4905 (2025); https://doi.org/10.1039/D5EE00500K

271. Y. Yi, F. Hai, X. Tian, Z. Wu, S. Zheng, J. Guo, W. Chen, W. Hua, L. Qu, M. Li. *Chem. Eng. J.*, **466**, 143303 (2023); https://doi.org/10.1016/j.cej.2023.143303

272. T. Zhang, Z. Song, J. Zhang, W. Jiang, R. Mao, B. Li, S. Liu, X. Jian, F. Hu. *J. Energy Chem.*, **81**, 510 (2023); https://doi.org/10.1016/j.jechem.2023.02.031

Accepted manuscript
This manuscript will be edited, formatted, and proof read. The file will be replaced with Version of Record.